

1-1-2005

## Mass transfer measurements for syngas fermentation

Amir Kapic  
*Iowa State University*

Follow this and additional works at: <https://lib.dr.iastate.edu/rtd>

---

### Recommended Citation

Kapic, Amir, "Mass transfer measurements for syngas fermentation" (2005). *Retrospective Theses and Dissertations*. 19129.

<https://lib.dr.iastate.edu/rtd/19129>

This Thesis is brought to you for free and open access by the Iowa State University Capstones, Theses and Dissertations at Iowa State University Digital Repository. It has been accepted for inclusion in Retrospective Theses and Dissertations by an authorized administrator of Iowa State University Digital Repository. For more information, please contact [digirep@iastate.edu](mailto:digirep@iastate.edu).

**Mass transfer measurements for syngas fermentation**

by

**Amir Kapic**

A thesis submitted to the graduate faculty  
in partial fulfillment of the requirements for the degree of  
**MASTER OF SCIENCE**

Major: Mechanical Engineering

Program of Study Committee:  
Theodore J. Heindel, Major Professor  
Robert C. Brown  
Alan A. DiSpirito

Iowa State University

Ames, Iowa

2005

Copyright © Amir Kapic, 2005. All rights reserved.

Graduate College  
Iowa State University

This is to certify that the master's thesis of  
Amir Kapic  
has met the thesis requirements of Iowa State University

Signatures have been redacted for privacy

## TABLE OF CONTENTS

|  |      |
|--|------|
| LIST OF FIGURES .....  | v    |
| LIST OF TABLES .....   | viii |
| LIST OF NOMENCLATURE .....   | ix   |
| ACKNOWLEDGEMENTS .....   | xiii |
| ABSTRACT .....   | xiv  |
| CHAPTER 1: INTRODUCTION .....  | 1    |
| CHAPTER 2: LITERATURE REVIEW .....   | 5    |
| 2.1 Basic Stirred Tank Reactor (STR) Geometry .....  | 5    |
| 2.2 Dimensionless Numbers .....  | 7    |
| 2.2.1 Reynolds Number .....  | 7    |
| 2.2.2 Ungassed Power Number .....  | 7    |
| 2.2.3 Gassed Power Number .....  | 8    |
| 2.2.4 Froude Number .....  | 8    |
| 2.2.5 Gas Flow Number .....  | 9    |
| 2.3 Scale-Up Rules .....   | 9    |
| 2.3.1 Bulk Flow Regimes in Gas-Liquid STRs ( $Q_g = \text{constant}$ ) .....                             | 11   |
| 2.3.2 Hydrodynamics in the Impeller Region of a Gas-Liquid Dispersion<br>( $N = \text{constant}$ ) ..... | 15   |
| 2.3.3 Power Consumption in Aerated STRs .....  | 17   |
| 2.3.4 STR Gas-Liquid Flow Regime Maps .....  | 20   |
| 2.4 Gas-Liquid Mass Transfer .....   | 22   |
| 2.4.1 $k_L a$ Measurement Methods .....  | 22   |
| 2.4.2 Oxygen-Liquid Mass Transfer .....  | 24   |
| 2.4.3 CO-Liquid Mass Transfer Rates from Syngas .....  | 30   |
| 2.5 Literature Review Summary .....  | 34   |
| CHAPTER 3: MATERIALS AND METHODS .....   | 44   |
| 3.1 Experimental Setup .....   | 44   |
| 3.2 Power Consumption Measurements in a STR .....  | 45   |
| 3.3 Dynamic Gassing-Out Method for Dissolved Oxygen Concentrations .....                                 | 47   |

|  |     |
|--|-----|
| 3.4 Myoglobin Method for Dissolved Carbon Monoxide Concentrations .....  | 51  |
| 3.4.1 Experimental setup for CO measurements from syngas.....  | 51  |
| 3.4.2 Preparation and Collection of Liquid Samples .....   | 52  |
| 3.4.3 Measuring Dissolved Carbon Monoxide Concentrations.....  | 53  |
| 3.4.4 Determining the $k_{La}$ Values for CO Concentration Data from<br>Syngas .....                                   | 56  |
| CHAPTER 4: RESULTS AND DISCUSSION.....   | 68  |
| 4.1 Power Correlation for Gas-Liquid Dispersions in a STR.....   | 68  |
| 4.2 Dissolved Oxygen Probe Measurements in a STR.....  | 72  |
| 4.2.1 Scale-Up Correlation Model.....  | 72  |
| 4.2.2 Normalized Hydrodynamic Flow Regime Maps .....   | 74  |
| 4.2.3 Available $k_{La}$ Data in the Literature .....  | 76  |
| 4.2.4 General Scale-Up Correlation for Dissolved Oxygen in Water.....  | 79  |
| 4.3 Scale-Up and Hydrodynamic Dependence of Gas-Liquid Mass Transfer<br>Correlation for Dissolved $O_2$ in Water ..... | 83  |
| 4.3.1 Gas-Liquid Mass Transfer Mechanisms in a STR.....  | 83  |
| 4.3.2 Hydrodynamic Dependence of Dissolved $O_2$ Correlations .....  | 84  |
| 4.4 Scale-Up Correlation for Dissolved CO in Water from Syngas.....  | 87  |
| 4.5 Gas-Liquid Scale-Up Model Discussion .....   | 90  |
| CHAPTER 5: CONCLUSIONS.....  | 118 |
| 5.1 Summary .....  | 118 |
| 5.2 Recommendations.....   | 120 |
| REFERENCES CITED.....  | 122 |

## LIST OF FIGURES

|                     |  |    |
|---------------------|--|----|
| <b>Figure 2.1:</b>  | Standard vessel geometry fitted with a Rushton disc-turbine (6DT).....   | 35 |
| <b>Figure 2.2:</b>  | Bulk flow patterns at constant gas flow rate ( $Q_g$ ) with increasing<br>impeller speed $N$ . .....   | 36 |
| <b>Figure 2.3:</b>  | Generic gassed power number as a function of flow number for gas-<br>liquid dispersion in STR systems with $Q_g = \text{constant}$ .....                           | 37 |
| <b>Figure 2.4:</b>  | Main bulk flow regime transitions of a gas-liquid dispersion in a<br>standard STR.....   | 38 |
| <b>Figure 2.5:</b>  | Cavity changes at constant $N$ with increasing $Q_g$ . .....   | 39 |
| <b>Figure 2.6:</b>  | Cavity systems with increasing $Q_g$ at constant $N$ . .....   | 40 |
| <b>Figure 2.7:</b>  | Gassed power ratio at constant impeller speed $N$ . .....  | 41 |
| <b>Figure 2.8:</b>  | Gassed power curve with cavity formation. ....   | 42 |
| <b>Figure 2.9:</b>  | General flow map for $T = 1.2$ m tank and $D = 0.48$ m impeller. ....  | 43 |
| <b>Figure 3.1:</b>  | Experimental (a) stirred-tank reactor geometry and (b) facility setup.....   | 58 |
| <b>Figure 3.2:</b>  | Mechanical power losses for the DC motor used in this study.....   | 59 |
| <b>Figure 3.3:</b>  | Comparison of Silicon and Teflon probe tip membranes for measuring<br>$k_L a$ values of dissolved $O_2$ in water. ....   | 60 |
| <b>Figure 3.4:</b>  | Normalized dissolved $O_2$ concentration as a function of time at $N =$<br>$400$ rev/min, and $Q_g = 5$ L/min of air.....  | 61 |
| <b>Figure 3.5:</b>  | STR experimental facility. ....  | 62 |
| <b>Figure 3.6:</b>  | Recirculation line for carbon monoxide sample withdrawal. ....   | 63 |
| <b>Figure 3.7:</b>  | Cross section of the sampling port with $10 \mu\text{L}$ syringe positioned in<br>the low bubble region.....   | 64 |
| <b>Figure 3.8:</b>  | Typical path followed by collected samples between $\text{CO}$ -saturated and<br>deoxygenated peaks to be interpolated by the Spectra Solve. ....                  | 65 |
| <b>Figure 3.9:</b>  | Dissolved $\text{CO}$ -concentration as a function of time at $N = 700$ rev/min<br>and $Q_g = 12$ L/min of syngas. ....  | 66 |
| <b>Figure 3.10:</b> | Determination of volumetric mass transfer coefficient ( $k_L a$ ) for $\text{CO}$ in<br>a STR at $N = 200$ rev/min and $Q_g = 12$ L/min of artificial syngas. .... | 67 |
| <b>Figure 4.1:</b>  | Un-aerated $P_o$ and aerated $P_g$ powers as a function of $N$ at constant $Q_g$ . ....  | 95 |
| <b>Figure 4.2:</b>  | Gassed power number $N_{pg}$ vs. the flow number $Fl_g$ at constant $Q_g$ . ....   | 96 |
| <b>Figure 4.3:</b>  | Gassed to un-gassed power ratio $P_g/P_o$ vs. gas flow rate $Q_g$ at constant<br>$N$ .....   | 97 |

|                     |   |     |
|---------------------|---|-----|
| <b>Figure 4.4:</b>  | Gasged to ungasged power ratio $P_g/P_o$ vs. Flow number $Fl_g$ at constant $N$ .....   | 98  |
| <b>Figure 4.5:</b>  | Gasged power ( $P_g$ ) vs. $P_o^2ND^3/Q_g^{0.56}$ for air dispersed in tap water with $D = 0.0747$ m standard disc turbine (6DT) in $T = 0.211$ m tank. ....  | 99  |
| <b>Figure 4.6:</b>  | Power number ( $N_{po}$ ) vs Reynolds number ( $Re$ ) for $x_1/D = 0.0167$ , $D/T = 0.35$ , and $c = T/4$ .....   | 100 |
| <b>Figure 4.7:</b>  | Hydrodynamic flow regime map for a $T = 0.211$ m vessel, $D/T = 0.35$ . ....  | 101 |
| <b>Figure 4.8:</b>  | Scale-up correlation for volumetric gas-liquid mass transfer coefficient ( $k_La$ ) in terms of relative dispersion parameter ( $N/N_{CD}$ ) and tank to impeller diameter ratio ( $T/D$ ).....                           | 102 |
| <b>Figure 4.9:</b>  | Illustration of a general leverage plot from JMP5.1 (a); comparison of significance shown in leverage plots (b).....  | 103 |
| <b>Figure 4.10:</b> | Contribution of the correlating parameters $N/N_{CD}$ (a), $U_g$ (b), and $T/D$ (c) to the significance of the scale-up model of Eq. (4.3).....   | 104 |
| <b>Figure 4.11:</b> | Volumetric mass transfer coefficient ( $k_La$ ) as a function of gas flow rate ( $Q_g$ ) at constant impeller speed ( $N$ ) for dispersed air in tap water.....   | 105 |
| <b>Figure 4.12:</b> | Volumetric mass transfer coefficient ( $k_La$ ) as a function of impeller speed ( $N$ ) at constant gas flow rate ( $Q_g$ ) for dispersed air in tap water. ....  | 106 |
| <b>Figure 4.13:</b> | Volumetric mass transfer coefficient ( $k_La$ ) as a function of gasged power density ( $P_g/V$ ) and superficial gas velocity ( $U_g$ ) for dispersed air in tap water.....  | 107 |
| <b>Figure 4.14:</b> | Comparison of ALC and BLC data to the flow regime dependant scale-up correlation for volumetric gas-liquid mass transfer from dispersed air in tap water (Eq. (4.6)).....   | 108 |
| <b>Figure 4.15:</b> | Volumetric mass transfer coefficient ( $k_La$ ) as a function of gas flow rate ( $Q_g$ ) at constant impeller speed ( $N$ ) for dispersed oxygen in water. ....   | 109 |
| <b>Figure 4.16:</b> | Volumetric mass transfer coefficient ( $k_La$ ) as a function of impeller speed ( $N$ ) at constant gas flow rate ( $Q_g$ ) for dispersed oxygen in water.....  | 110 |
| <b>Figure 4.17:</b> | Volumetric mass transfer coefficient ( $k_La$ ) as a function of gasged power density ( $P_g/V$ ) and superficial gas velocity ( $U_g$ ) for dispersed oxygen in tap water in $T = 0.211$ m vessel and $D/T = 0.35$ ..... | 111 |
| <b>Figure 4.18:</b> | Flow regime dependence of ALC and BLC data in the scale-up correlation for volumetric gas-liquid mass transfer from dispersed oxygen in tap water at $25^\circ\text{C}$ .....   | 112 |
| <b>Figure 4.19:</b> | Carbon-monoxide mass transfer scale-up correlation in the ALC   |     |

|                     |   |     |
|---------------------|---|-----|
|                     | region using an artificial syngas blend of 20% CO, 18%CO <sub>2</sub> , 52%N <sub>2</sub> , and 10% H <sub>2</sub> in tap water at 30°C. ....   | 113 |
| <b>Figure 4.20:</b> | Volumetric mass transfer coefficient ( $k_L a$ ) as a function of gas flow rate ( $Q_g$ ) at constant impeller speed ( $N$ ) for dispersed artificial syngas in tap water with $D = 0.0747$ m impeller in $T = 0.211$ m vessel. ....                  | 114 |
| <b>Figure 4.21:</b> | Volumetric mass transfer coefficient ( $k_L a$ ) as a function of impeller speed ( $N$ ) at constant gas flow rate ( $Q_g$ ) for dispersed artificial syngas in tap water with $D = 0.0747$ m impeller in $T = 0.211$ m vessel. ....                  | 115 |
| <b>Figure 4.22:</b> | Predicted mass transfer rates for carbon-monoxide from air in tap water at 30°C sparging artificial syngas (20% CO, 18% CO <sub>2</sub> , 52% N <sub>2</sub> , 10% H <sub>2</sub> ) using Eq. (4.14) for $T = 0.211$ m vessel in the ALC region. .... | 116 |
| <b>Figure 4.23:</b> | Dissolved O <sub>2</sub> mass transfer rates predicted from air in tap water at 20°C from Eq. (4.15) for $T = 0.211$ m vessel in the ALC region. ....   | 117 |

**LIST OF TABLES**

|                   |   |    |
|-------------------|---|----|
| <b>Table 3.1:</b> | Actual $k_L a$ values compared to $k_L a$ values for $\tau_p = 5$ s (van de Sande, 1974)..... | 49 |
| <b>Table 4.1:</b> | Literature data used in the general scale-up correlation development (Eq. (4.6)).....         | 77 |

## LIST OF NOMENCLATURE

|                 |   |                         |
|-----------------|---|-------------------------|
| A               | Absorption value                            | (-)                     |
| B               | Constant of integration                     | (-)                     |
| C               | Concentration of dissolved gas in water     | (mole m <sup>-3</sup> ) |
| C <sub>0</sub>  | Initial gas concentration in bulk of liquid | (mole m <sup>-3</sup> ) |
| C <sub>i</sub>  | Equilibrium dissolved gas concentration     | (mole m <sup>-3</sup> ) |
| C <sub>k</sub>  | Partial gas concentration of any species k  | (mole m <sup>-3</sup> ) |
| C <sub>P</sub>  | Protein concentration                       | (μM)                    |
| C*              | Normalized gas concentration                | (-)                     |
| C <sub>1</sub>  | Experimental constant                       | (-)                     |
| c               | Impeller clearance above the base           | (m)                     |
| D               | Impeller diameter                           | (m)                     |
| D <sub>d</sub>  | Rushton disc diameter                       | (m)                     |
| D <sub>i</sub>  | Width of the impeller blade                 | (m)                     |
| D <sub>s</sub>  | Ring sparger diameter                       | (m)                     |
| E               | Induced voltage                             | (V)                     |
| Fl <sub>g</sub> | Gas flow number; $Fl_g = Q_g/ND^3$          | (-)                     |
| Fr              | Froude number; $Fr = N^2D/g$                | (-)                     |
| g               | Gravitational constant                      | (m s <sup>-2</sup> )    |
| H               | Liquid height in vessel                     | (m)                     |
| I               | Current intensity                           | (A)                     |
| K               | Experimental constant                       | (-)                     |

|                |  |                  |
|----------------|--|------------------|
| $k_{La}$       | Liquid-side volumetric mass transfer coefficient   | ( $s^{-1}$ )     |
| $K\phi$        | Electric motor torque constant                     | ( $Nm A^{-1}$ )  |
| $l$            | Path length of cuvette                             | (cm)             |
| $N$            | Impeller rotational speed                          | ( $rev s^{-1}$ ) |
| $N_{pg}$       | Gassed power number; $N_{pg} = P_g/\rho N^3 D^5$   | (-)              |
| $N_{po}$       | Ungassed power number; $N_{po} = P_o/\rho N^3 D^5$ | (-)              |
| $\bar{N}_{po}$ | Average ungassed power number                      | (-)              |
| $p$            | Total gas mixture pressure                         | ( $Nm^{-2}$ )    |
| $P_b$          | Buoyancy gas power                                 | (W)              |
| $p_k$          | Partial pressure of any species k                  | ( $Nm^{-2}$ )    |
| $P_e$          | Electrical power converted to mechanical power     | (W)              |
| $P_{e,t}$      | Total electrical power absorbed                    | (W)              |
| $P_g$          | Gassed power input from impeller to liquid         | (W)              |
| $P_{joule}$    | Power by joule effect                              | (W)              |
| $P_{mech}$     | Mechanical power                                   | (W)              |
| $P_o$          | Ungassed power input from impeller to liquid       | (W)              |
| $Re$           | Reynolds number; $Re = ND^2\rho/\mu$               | (-)              |
| $T$            | Vessel inside diameter                             | (m)              |
| $T_{loss}$     | Mechanical torque losses                           | (Nm)             |
| $T_{mech}$     | Mechanical torque                                  | (Nm)             |
| $T_o$          | Reference vessel diameter                          | (m)              |
| $t$            | Time   | (s)              |

|       |   |                                |
|-------|---|--------------------------------|
| $t_0$ | Starting time for air sparging                                | (s)                            |
| $U_g$ | Sparged superficial gas velocity                              | ( $\text{m s}^{-1}$ )          |
| $U_v$ | Probe response voltage  | (V)                            |
| $V$   | Liquid volume in vessel                                       | ( $\text{m}^3$ )               |
| vvm   | Volumetric gas flow rate per minute per unit of liquid volume | ( $\text{min}^{-1}$ )          |
| $Q_g$ | Volumetric gas flow rate                                      | ( $\text{m}^3 \text{s}^{-1}$ ) |
| $x_k$ | Mole fraction of the amount of any species k                  | (-)                            |
| $x_1$ | Disc thickness  | (m)                            |

### Superscripts

|         |                       |     |
|---------|-----------------------|-----|
| x, y, z | Exponential constants | (-) |
|---------|-----------------------|-----|

### Subscripts

|     |                     |
|-----|---------------------|
| CD  | Complete dispersion |
| F   | Flooding            |
| R   | Recirculation       |
| max | maximum             |

### Abbreviations

|      |                                   |
|------|-----------------------------------|
| ALR  | Air-lift reactor                  |
| ALC  | After large cavity                |
| BCR  | Bubble column reactor             |
| BLC  | Before large cavity               |
| CSTR | Continuously stirred tank reactor |

|     |                             |
|-----|-----------------------------|
| FBT | Flat blade turbine          |
| FSM | Feeding steady state-method |
| PBT | Pitched blade turbine       |
| PCU | Primary control unit        |
| STR | Stirred-tank reactor        |
| TBR | Trickle-bed reactor         |
| 6DT | Six-bladed disc turbine     |

### Greek Symbols

|                 |                          |                                       |
|-----------------|--------------------------|---------------------------------------|
| $\alpha, \beta$ | Exponential constants    | (-)                                   |
| $\varepsilon$   | Gas holdup               | (-)                                   |
| $\varepsilon_a$ | Absorption coefficient   | ( $\mu\text{M}^{-1} \text{cm}^{-1}$ ) |
| $\rho$          | Liquid density           | ( $\text{kg m}^{-3}$ )                |
| $\rho_G$        | Gas density              | ( $\text{kg m}^{-3}$ )                |
| $\mu$           | Liquid dynamic viscosity | ( $\text{Ns m}^{-2}$ )                |
| $\tau_p$        | Probe response time      | (s)                                   |
| $\theta$        | Liquid temperature       | ( $^{\circ}\text{C}$ )                |

## **ACKNOWLEDGEMENTS**

I would like to express my gratitude to all those who gave me the possibility to complete this masters thesis.

I am deeply indebted to my supervisor Dr. Ted Heindel at Iowa State University of Science and Technology whose help, stimulating suggestions, and encouragement helped me in this research thesis. Many thanks go to Dr. Ted Heindel for all his help throughout my entire graduate program.

I would like to thank Dr. Robert Brown for stimulating support and Dr. Alan DiSpirito for helpful communication, which greatly encouraged my thesis work. Many thanks go to Dr. Robert Brown and Dr. Alan DiSpirito for serving on my committee.

I want to thank the entire Department of Mechanical Engineering at Iowa State University for giving me permission to commence this thesis in the first instance, to do the necessary research work and to pursue a graduate carrier. I would like to also thank Dr. Mark Hargrove and Dr. Ruben Peters and all the lab staff from the Department of Biochemistry, Biophysics and Molecular Biology for the use of the necessary equipment.

I would like to give my special thanks to all my family members whose patient love enabled me to complete this work.

This material is based upon work supported by the Cooperative State Research, Education, and Extension Service, U.S. Department of Agriculture, under Agreement Nos. 2002-34188-12035 and 2004-34188-15067. Their support is greatly appreciated.

## ABSTRACT

A general scale-up correlation is developed for the volumetric gas-liquid mass transfer coefficient ( $k_L a$ ) in stirred-tank reactors (STRs) for oxygen transport using results from the literature and the current study. Power data for the dispersion of air in water by a six-bladed Rushton impeller are obtained by measuring electrical power, and a gassed power correlation is proposed. A correlation for gas-liquid mass transfer based on the energy input criteria of the form  $k_L a = C_1 (P_g / V)^\alpha U_g^\beta$  fit the data well, but, in general, is dependant on flow regime and the vessel size. The volumetric mass transfer coefficient ( $k_L a$ ) is correlated on the basis of the relative dispersion parameter ( $N/N_{CD}$ ) for similar impeller hydrodynamics and operating regimes. A stirred-tank reactor scale-up technique from bench-scale ( $T = 0.211$  m and  $D/T = 0.35$ ) to industrial-scale (up to  $T = 2.7$  m) is proposed using a normalized hydrodynamic flow regime map and shown to be useful in understanding the range of operational conditions for the successful scale-up of stirred tank reactors. The experiments show that the scale-up model can be applied for a single and or multi-gas component mass transport to liquids if the STR is operated in the same hydrodynamic regime. A method for determining dissolved carbon monoxide concentrations from artificial syngas is developed and the volumetric gas-liquid mass transfer rates are determined. The gas-liquid scale-up model is used in carbon monoxide mass transfer scale-up for syngas fermentation in a STR. Carbon monoxide mass transfer rates obtained in this work are predicted from those of air correlated from literature. A STR scale-up model is extended to other reactor types such as air lift reactors and bubble columns in mixing applications, and the corresponding gas-liquid scale-up model is suggested.

## CHAPTER 1: INTRODUCTION

Mixing technology has developed over the past 50 years and many mixing principles and designs of mixing equipment for desired process objectives have become possible. Gas-liquid stirred tank reactors (STRs) are widely used throughout the process industry, including applications to absorption, stripping, chlorination, fermentation, oxidation, and wastewater treatment. They are also used for carrying out biochemical processes such as an anaerobic fermentation process for the conversion of waste gases from refinery operations into usable products, such as plastics, chemicals, and fuels (Worden, 1997). The United States is extremely dependant on petroleum-based products from which more than 50% are currently imported (USDOE-Energy Efficiency and Renewable Energy, 2005). Utilizing biorenewable resources to convert biomass to useful products through syngas fermentation could replace petroleum-based products with biobased products and help relieve the dependence this country has on petroleum imports.

Fermentation has always been an important part in our lives (i.e., food industry, chemistry, medicine, etc.). The general premise is that microorganisms take one component and biologically convert it to another component. Lynd (1996) suggested that syngas fermentation offers cost and efficiency advantages in the production of biobased products from a wide variety of biomass feedstocks. A recent study (Mississippi State School of Chemical Engineering) compared two processes for ethanol production from syngas (primarily a mixture of CO and H<sub>2</sub>): (i) the use of an inorganic heterogeneous catalysts (such molybdenum sulfide), and (ii) bioconversion using syngas fermentation. Below is a

summary of the benefits of syngas fermentation process over the catalytic process (Mississippi State School of Chemical Engineering):

1. The fermentation process operates at low temperatures and pressures as opposed to those required for the catalytic process, thus, reducing capital costs and increasing the safety aspects of the plant.
2. The fermentation process produces a higher ethanol yield than the catalytic process.
3. Based on past DOE funded research using refinery gases, the fermentation process is more economically attractive.
4. The fermentation process is much more forgiving in terms of varying syngas flow rate and composition.
5. The fermentation process is not poisoned by the presence of sulfur compounds which is particularly problematic in the catalytic process

In replacing petroleum-based products with biobased products, the syngas approach employs CO and H<sub>2</sub> as the building blocks for synthesis of chemicals and fuels from biomass. A significant bottleneck in the process is the syngas-liquid mass transfer limitations because the major syngas components (CO and H<sub>2</sub>) have low solubilities in the fermentation broth. In biotechnology and engineering, a production of biobased products from a wide variety of biomass feedstocks can be made possible if the two disciplines can be integrated to overcome mass transfer limitations in syngas-liquid STRs.

The CO utilization by the anaerobic microorganisms provides energy for growth and material for product formation via fermentation. Limitations on the CO-liquid mass transfer are likely to reduce cell growth and product yield. The shortage of the CO in the fermentation broth may also cause the formation of unwanted byproducts and, possibly, cell

death.

This study will investigate CO mass transfer from an artificial syngas blend of 20% CO, 18% CO<sub>2</sub>, 52% N<sub>2</sub>, and 10% H<sub>2</sub>. This is a representative syngas mixture that can be produced by the gasifier currently located in 1056 Black Engineering Building at Iowa State University, Ames. Typically, fermentations on both the bench-top and industrial scale are very expensive. Hence, this study will focus on the CO-liquid mass transfer from the artificial syngas using tap water as a model fluid (i.e., in the absence of microorganisms) in a bench-top STR.

An optimization of the mass transfer rates and STR performance for a given system requires an understanding of the influences of power input, impeller speed, gas flow rate, geometry, agitator type, etc. Typically, the agitator aids the mass transfer from syngas bubbles to the fermentation broth and from the broth to the microorganisms. One of the goals of this work is to apply biochemical methods to measure dissolved CO concentrations in water with enough accuracy to obtain reliable mass transfer coefficients ( $k_La$ ) necessary to describe a STR fermentation performance.

Another important goal in the process industries is scale-up of STRs, air lift reactors, bubble columns, and relevant devices for industrial-scale operations. Scale-up must be accomplished to reproduce the process in a large volume. In this research, the bench-top mass transfer studies are completed in volumes of a few liters, while an industrial-scale reactor may hold several thousand liters. Currently, the availability of dissolved CO mass transfer rates in STRs of various sizes is extremely limited in the literature; hence, the scale-up cannot be completed due to the lack of CO mass transfer rates in reactors of different size. However, the available literature data for dissolved oxygen mass transfer will be used to

develop a scale-up model that will be extended to the scale-up of CO mass transfer rates for syngas fermentation. Similarly, the scale-up model for other reactor types (i.e, air lift reactors, bubble columns, etc.) will be introduced and briefly discussed in the end of this thesis.

This thesis will expand on the above ideas, including gas-liquid mass transfer measurements and the corresponding correlations development in a bench-top STR to predict a performance of an industrial STR size. Chapter 2 will provide background information relevant to CO-liquid mass transfer in STRs. Chapter 3 will address materials and methods for STR power consumption, and dissolved oxygen and carbon monoxide mass transfer measurements. Chapter 4 will interpret the results and present the correlations obtained in this study and the literature. A STR scale-up model for gas-liquid mass transfer will be proposed and a similar model will be suggested for other mixing devices (i.e., air-lift reactors, bubble columns). And Chapter 5 will conclude the work of this thesis and provide the important recommendations.

## CHAPTER 2: LITERATURE REVIEW

This chapter is divided into five major sections. The first section discusses a standard STR geometry. The second section defines the important dimensionless numbers in gas-liquid mass transfer studies. The third section talks about the scale-up of STRs and reviews important gas-liquid flow regimes and the associated impeller hydrodynamics. The fourth section reviews the gas-liquid mass transfer measurements in STRs for oxygen from air, and carbon monoxide from syngas for fermentation studies. This section also reviews some measuring techniques that are available for measuring dissolved gases in water. The last section summarizes the literature review.

### 2.1 Basic Stirred Tank Reactor (STR) Geometry

Cylindrical stirred tank reactors having diameter  $T$  are either designed with flat or dished bottoms. The effects of flat-bottom tanks, ASME dished-bottom tanks, and shallow cone tanks are considered to be essentially the same. A dished-bottom reactor is generally preferred for promoting more effective mixing of the tank contents and maximizing suspension quality of the solid phase. Vessels containing low-viscosity fluids tend to swirl and produce vortices which are in most cases undesirable if operating in the turbulent regime. Baffles are used to destroy the vortices and aid in good mixing of the tank contents. A standard baffle configuration consists of four vertical plates spaced 90 degrees apart and

having a width equal to  $T/12$  or  $T/10$  of the tank diameter (Fig. 2.1)\*. A gas sparger is used to introduce gas into the liquid for efficient gas-liquid contacting in assisting mass transfer. The most commonly used sparger configuration consists of a ring with equally spaced sparger holes positioned on the bottom side of the ring to prevent contamination and allow easier maintenance. The sparger ring is located directly below the impeller and its diameter should be less than the impeller diameter, typically  $0.8D$ , where  $D$  is the impeller diameter.

There are many impeller types in commercial use, and determination of the most effective impeller should be based on the process requirements and knowledge of the physical properties of the tank contents. Impellers can be classified as turbines for low and medium viscosity fluids and close-clearance impellers for high viscosity fluids. Turbine impellers are further subdivided based on flow patterns, such as axial flow and radial flow. In this work, radial flow impellers designed with six blades (i.e., a Rushton turbine-6DT) will be considered as shown in Fig 2.1. For standard Rushton turbines, the impeller diameter ( $D$ ) is usually in the range of  $T/4$  to  $T/2$  and constructed with six vertical blades of length  $D/4$  and width of  $D/5$ . Typically, radial flow impellers may either be disc-type (Rushton turbine) or be an open flat blade turbine (FBT). Disk-type radial impellers provide more uniform radial flow with the disk acting as a baffle on the impeller in preventing gas from rising along the vessel shaft. As shown in Fig. 2.1, standard disc diameters ( $D_d$ ) for Rushton turbines are of  $2/3$  or  $3/4$  times the impeller diameter  $D$ . To provide a maximum gas contact time, the impeller should be close to the base, but not so close as to impact its pumping capacity ( $c = T/4$  is recommended). Liquid height ( $H$ ) equal to the tank diameter ( $T$ ) is commonly used in

---

\*Note: All figures in this thesis are located at the end of the respective chapter.

STR studies.

## 2.2 Dimensionless Numbers

Dimensionless groups are widely used to correlate data in the process industries. This section will provide definitions of dimensionless numbers and emphasize their importance and physical meaning in the study of STRs.

### 2.2.1 Reynolds Number

In stirred tank reactor studies, the Reynolds number (Re) takes the form:

$$\text{Re} = \frac{\rho ND^2}{\mu} \quad (2.1)$$

where both  $\rho$  and  $\mu$  are based on the liquid properties in gas-liquid dispersion systems. Usually, the impeller speed  $N$  is specified in rev/s and the impeller diameter  $D$  in meters. Physically, the Reynolds number in agitated vessels represents the ratio of inertial to viscous forces and is used to characterize the fluid flow (i.e., laminar, transitional, or turbulent).

### 2.2.2 Ungassed Power Number

Power input from agitation in ungasged vessels is normally correlated in terms of the power number,  $N_{po}$ , as a function of Reynolds number,  $\text{Re}$ . The ungasged power number ( $N_{po}$ ) represents the ratio of the pressure differences producing flow to the inertial forces of the liquid dispersion and it is analogous to a friction factor or drag coefficient (Dawson, 1992).  $N_{po}$  is usually based on the power input by the impeller for agitated vessels and takes

the form:

$$N_{po} = \frac{P_o}{\rho N^3 D^5} \quad (2.2)$$

where  $P_o$  is the impeller power input into the liquid without sparged gas.

### 2.2.3 Gassed Power Number

The gassed power number,  $N_{pg}$ , is a dimensionless parameter that provides a measure of the power requirements for the impeller operation in a gas-liquid dispersion. The gassed power number represents the ratio of the pressure differences producing flow to the inertial forces of a gas-liquid dispersion. When gas is introduced into ungassed agitated vessels, the mixing power will drop and is related to a gassed power number defined by:

$$N_{pg} = \frac{P_g}{\rho N^3 D^5} \quad (2.3)$$

where  $P_g$  is the impeller power input into the liquid when gas is sparged into the vessel.

### 2.2.4 Froude Number

The Froude number (Fr) represents the ratio of inertial to gravitational forces and is defined by:

$$Fr = \frac{N^2 D}{g} \quad (2.4)$$

For nonaerated vessels equipped with four baffles, the Froude number is generally considered to be unimportant (Dawson, 1992).

### 2.2.5 Gas Flow Number

The gas flow number ( $Fl_g$ ) represents the ratio of gas flow rate to a quantity proportional to the impeller pumping rate and is given by:

$$Fl_g = \frac{Q_g}{ND^3} \quad (2.5)$$

The gas flow number includes the effects of gassing rate, impeller rotational speed, and impeller diameter, and is very important in determining the flow phenomena occurring in the impeller region. Typically, the flow number represents a measure of the impeller pumping capacity.

## 2.3 Scale-Up Rules

Two of the most important parameters in stirred gas-liquid dispersions is the gassed power consumption, which determines the operating costs, and the volumetric mass transfer coefficient,  $k_La$ . In spite of much research in agitated gas-liquid dispersions, no complete method exists yet for the prediction of  $k_La$  and scale-up with the power consumption. Midoux et al. (1978) divided the available correlations from the literature into three groups: (i) dimensionless empirical correlations, (ii) correlations based on the dimensionless gas flow rates, and (iii) dimensional empirical correlations.

Various investigators have correlated  $k_La$  to agitation power input per unit volume and superficial gas velocity over one or two similar vessel sizes. However, published results in air-water systems show a large scatter when plotted in the form:

$$k_L a = C_1 \left( \frac{P_g}{V} \right)^\alpha U_g^\beta \quad (2.6)$$

where the exponents  $\alpha$  and  $\beta$  range from 0.3 to 0.7 and 0 to 1.0, respectively, as summarized by Stenberg and Andersson (1988). They dispersed air in tap water using three standard stirred tank reactors (STRs) in an attempt to scale-up liquid volumes of 0.12, 0.6, and 3 m<sup>3</sup>. The mass transfer coefficient was found to be independent of the superficial gas velocity in the 0.12 m<sup>3</sup> vessel, but gave an exponential dependence of 0.54 in the 3 m<sup>3</sup> vessel. Experimental results showed large variations between the vessel sizes, with the gas flow dependence being the most effective in scattering the data. Stenberg and Andersson (1988) concluded that both reactor size and superficial gas velocity were correlated to the change in exponents when  $k_L a$  values are plotted in the form of Eq. (2.6).

Similar variations in scale-up constants with various tank sizes were recognized by Rushton and Bimbinet (1968). They investigated gas holdup in air-water systems using different vessel sizes, impeller types, and air flow rates. The effects of superficial gas velocity and total power input, which in addition to impeller power included the power introduced into the vessel by the gas flow, were correlated to gas holdup. In the analysis of gas holdup scale-up, Rushton and Bimbinet (1968) found that the effect of impeller to tank diameter ratio ( $D/T$ ) and tank diameter alone ( $T$ ) can be accounted for by the variation of  $C_1$  and  $\alpha$  when the gas holdup is of the form  $\varepsilon \propto \left( \frac{P_g}{V} \right)^\alpha U_g^\beta$ , similar to Eq. (2.6). They found that both  $C_1$  and  $\alpha$  pass through maximum values as  $D/T$  changes and the exponent  $\beta$  stayed constant. They suggested that the correlation based on the power criteria ( $P_g/V$ ) is scale dependent and should have additional terms for a successful scale-up. This is supported by

the fact that in many scale-up attempts, power criteria has been shown to be unsuccessful in predicting industrial-scale results from laboratory trials, but it is very successful in correlating data from similarly sized vessels. The most commonly used scale-up equation (Eq. (2.6)) does not contain a tank geometric quantity, and the gassed power density term should account for geometrical similarity if the geometric ratios of STR's operating components (i.e., impeller size, baffle geometry, etc.) to tank diameter are kept constant.

Proper design of STRs requires knowledge of the fluid behavior in terms of gas-liquid operating regimes and contact time or holdup, so that mass transfer coefficients can be determined in bench-top equipment and projected to large industrial-scale systems. There are flooding limits, complete dispersion transitions, cavity formations, and critical impeller speeds below which the impeller is not effective in dispersing the gas into the liquid. These limits will now be discussed.

### **2.3.1 Bulk Flow Regimes in Gas-Liquid STRs ( $Q_g = \text{constant}$ )**

In standard STRs, the impeller rotational speed ( $N$ ) and the gas flow rate ( $Q_g$ ) are the two major parameters that influence the gas-liquid flow regime. Important definitions in aerated STRs include the flooding transition impeller speed  $N_F$ , the complete dispersion impeller speed  $N_{CD}$ , and the recirculation impeller speed  $N_R$ . Correlations presented below are for different vessel sizes to better understand the scale-up analysis of the various flow regimes for six-blade disc style impellers (6DT) with a standard tank geometry and  $H = T$ .

Nienow et al. (1985) studied the effect of scale and geometry on flooding, complete dispersion, recirculation, and power in gassed stirred vessels of different sizes ( $T = 0.29, 0.56, 0.61, 0.90, 0.91, 1.83$  m). Figure 2.2 shows the bulk mixing stages observed with disc

turbines when the impeller speed is increased from low (a) to high (e) at a constant gas flow rate (Nienow et al., 1985). These bulk flow patterns are summarized as: (a) negligible dispersion; (b) upper part of the vessel acting as a bubble column; (c) gas circulation in the upper part of the vessel with occasional movement in the lower vessel part; (d) gas circulation throughout the whole vessel; and (e) secondary circulation loops form and gross recirculation.

Rushton and Bimbinet (1968) defined the transition from (c) to (b) in Fig. 2.2 as the onset of flooding. On the other hand, Nienow et al. (1985) defined the transition between (d) and (c) in Fig. 2.2 as the onset of flooding by observing conditions at which the entire lower part of vessel below the impeller was not aerated. If a STR is operated at a constant gas flow rate ( $Q_g$ ) with increasing impeller speed ( $N$ ), smaller bubbles are formed as  $N$  increases, resulting in a larger interfacial area and a higher gas-liquid mass transfer rate. With gradually decreasing the impeller speed  $N$  at constant gas flow rate, large bubbles form, reducing the interfacial area and resulting in smaller gas-liquid mass transfer because the impeller is unable to properly disperse the gas in the tank. When  $N$  is decreased to a certain value, the gas-liquid flow pattern suddenly changes and there are no longer bubbles present in the space below the impeller. At this state, only the upper part of the vessel is aerated and it acts like a bubble column. This state is known as the onset of flooding as defined by Rushton and Bimbinet (1968). Although there tends to be inconsistencies in the literature as to the exact definition, flooding is generally defined as the flow regime where the impeller cannot properly disperse the gas throughout the vessel, as shown in Fig. 2.2a. This condition is to be avoided. Nienow et al. (1985) identified the minimum impeller speed ( $N_F$ ) required to prevent flooding:

$$(Fl_g)_F = 30(Fr)_F \left( \frac{D}{T} \right)^{3.5} \quad (2.7)$$

where  $(Fl_g)_F$  represents the gas flow number at the flooding condition, and  $(Fr)_F$  is the corresponding Froude number at flooding. It can be seen from Eq. (2.7) that the minimum impeller speed at flooding is a strong function of impeller to vessel diameter ratio ( $D/T$ ) since the impeller's ability to disperse the gas plays a major role in the flooding transition. This correlation has been found to fit data well for a wide range of vessels, including  $0.29 \leq T \leq 1.2$  m and  $0.22 \leq D/T \leq 0.5$ , for both coalescing and noncoalescing liquids, and for both point and ring spargers of diameter  $\leq 0.8D$ .

Power input from agitation in ungasged vessels is normally correlated in terms of the power number  $N_{po}$  (Eq (2.2)), as a function of Reynolds number  $Re$ , (Eq. (2.1)). The ungasged power number,  $N_{po}$ , for a 6DT Rushton turbine is assumed to be constant for  $Re > 2 \times 10^4$  (Nienow et al., 1985). Introducing the gas in the tank at constant impeller speed reduces the required power, as determined by the gassed power number  $N_{pg}$ .

Usually  $N_{pg}$  or the ratio of power numbers under gassed and ungasged condition ( $N_{pg}/N_{po} = P_g/P_o$ ), is plotted as a function of flow number  $(Fl_g)$  at constant gas flow rate ( $Q_g$ ) or at constant impeller speed ( $N$ ). At constant gas flow rate ( $Q_g$ ), the power curve of  $N_{pg}$  or  $P_g/P_o$  as a function of  $Fl_g$  will follow a well known trend as shown in Fig. 2.3, with local minimum and maximum points empirically identified according to Nienow et al. (1985). Figure 2.3 is useful for determining the bulk flow regime transitions. The local minimum occurs at an impeller speed associated with the onset of complete gas dispersion ( $N_{CD}$ ). The local maximum corresponds to the recirculation point as defined by Nienow and Wisdom (1976),

with  $N_R$  being the associated impeller speed. The sharpness of the local minimum and maximum at the transition is highly dependent on the vessel size. Larger vessels have more gradual transitions while smaller vessel sizes have more abrupt transitions.

For efficient operation, the impeller speed  $N$  must be greater than the impeller speed at which complete gas dispersion occurs ( $N > N_{CD}$ ). Nienow et al. (1977) correlated the impeller speed for complete gas dispersion in the following form:

$$(Fl_g)_{CD} = 0.2(Fr)_{CD}^{0.5} \left( \frac{D}{T} \right)^{0.5} \quad (2.8)$$

As shown in Fig. 2.3, the impeller speed  $N_{CD}$  corresponds to the local minimum when the gassed power is plotted as a function of flow number at constant gas flow rate. This condition will utilize the minimum power for complete gas dispersion in the liquid. As the impeller speed increases above  $N_{CD}$ , up to  $N_R$  and above, the gas phase is still well-mixed and a secondary circulation loop forms in the upper part of the vessel, which can be seen in Fig. 2.2e.

The amount of gas recirculation partially determines the nature of the gas phase mixing that occurs in the tank, which affects the mass transfer interfacial area. As a result, the impeller speed for the initial onset of recirculation was defined by Nienow and Wisdom (1976) and correlated in the dimensionless form:

$$(Fl_g)_R = 13(Fr)_R^2 \left( \frac{D}{T} \right)^5 \quad (2.9)$$

Figure 2.4 summarizes the bulk flow regimes with the designated flow transitions  $N_F$ ,  $N_{CD}$ , and  $N_R$  as defined above while omitting flow regime (b) in Fig. 2.2 for simplicity.

In summary, by increasing the impeller speed while maintaining a constant gas flow rate, the following bulk flow regimes may be observed: (i) if the gas flow rate is too high, it dominates the flow and the impeller becomes flooded  $N_F$  (Fig. 2.4a); (ii) for  $N_F < N < N_{CD}$ , the impeller is loaded but the gas is not completely dispersed (Fig. 2.4b); (iii) for  $N_{CD} < N < N_R$ , the gas is completely dispersed (Fig. 2.4c); and (iv) when  $N > N_R$ , large amounts of gas recirculate throughout the vessel. These bulk flow phenomena affect the direct power draw by the impeller in a gas-liquid dispersion. Therefore, much effort by many researchers has been dedicated to the study of the impeller gas dispersion and the associated local hydrodynamics and power draw.

### **2.3.2 Hydrodynamics in the Impeller Region of a Gas-Liquid Dispersion ( $N = \text{constant}$ )**

The bulk flow regimes and the flow regimes around the impeller region require additional study to explain the complex phenomena in stirred tank gas dispersion. According to Warmoeskerken and Smith (1982, 1984b), the flow regime around the impeller has a direct influence on the power demand and is closely related to the mass transfer between the dispersed gas and the liquid. For a single-phase STR with a Rushton impeller, liquid flow around the impeller is mainly characterized by two roll vortices formed behind the upper and lower edges of the blades. If gas is introduced into these vortices at constant impeller speed, gas-filled cavities form. Van't Riet (1975) studied the cavity formation at the impeller blades in detail and defined three cavity forms that depend on the stirrer speed and gas flow rate: (i) vortex cavities, (ii) clinging cavities, and (iii) large cavities. As shown in Fig. 2.5a, vortex cavities form at constant impeller speeds and at low gas rates, and are low-pressure regions in

which the gas gets pulled into, and dispersed from, the cavity to form ventilated gas cavities (Smith and Warmoeskerken, 1985). The word “ventilated” means that the gas flows into the cavity and is dispersed from the cavity. This results in the gassed power consumption decreasing as the volume of gas in the impeller cavities increases. If the gas flow rate is further increased, the vortex rotation is reduced and the cavity continues to grow and begins to cling to the rear of the blade (Fig. 2.5b). In both cases (i) and (ii), the gas breaks away from the cavity in a turbulent fashion. A further increase in the gas flow rate leads to the development of large cavities (Fig. 2.5c), which are characterized by clear smooth surfaces from which gas breaks away in a much more gentle way.

Although vortex and clinging cavities form six-symmetric structures on a Rushton impeller, Warmoeskerken et al. (1984a) observed a three-symmetric cavity structure known as a 3-3 cavity structure as shown in Fig. 2.6. The 3-3 cavity structure starts with three large cavities and three clinging cavities in the form of a symmetrical pattern around the impeller, and it continues to grow with increasing flow number. Smith and Warmoeskerken (1985) found 3-3 structures to be remarkably stable at given operating conditions, meaning that the cavities remain associated with the given blades and do not change their relative configurations once formed. In prior work (Warmoeskerken et al., 1984b) it was reported that 3-3 cavity structures directly affect the power demand of the impeller, which in turn influences other process variables such as gas holdup and gas-liquid mass transfer. At higher gas flow rates, six large cavities of two different sizes develop and distribute themselves in an alternating large-small 3-3 structure configuration. Smith and Warmoeskerken (1985) precisely determined the transition from clinging cavities to 3-3 cavity structures by analyzing the output from strain gauges mounted on the impeller vane with a frequency

analyzer. The transition from the vortex-clinging cavities to the first large cavity occurred at gas flow number given by:

$$Fl_g = 3.8 \times 10^{-3} \left( \frac{Re^2}{Fr} \right)^{0.067} \left( \frac{T}{D} \right)^{0.5} \quad (2.10)$$

Warmoeskerken and Smith (1985) noted that large cavities of the 3-3 structure cannot occur below a Froude number of 0.045 in vessels with  $D/T = 0.4$  at  $c = D$ . At high gas flow rates, the impeller becomes overloaded and the 3-3 stable structures are replaced by six irregular and rather unstable vibrating ragged cavities (Fig. 2.6d) as reported by Nienow et al., (1985). In general, the impeller gas dispersion regions associated with various cavity types as shown in Fig. 2.6a-c occur when the impeller speed is in range  $N_F < N < N_R$ , and Fig 2.6d is found when  $N < N_F$ . Of all the cavity types, the 3-3 structure appears to be the most important because of the gas handling capability of this system.

### 2.3.3 Power Consumption in Aerated STRs

The hydrodynamics and power draw are interrelated and are combined in the more recent studies of gas dispersion. Nienow et al. (1985) studied the power curve behavior with cavity formation in a more detailed fashion. In general, plots of  $P_g/P_o$  versus the flow number ( $Fl_g$ ) at constant impeller speed ( $N$ ) follow a generic shape shown in Fig. 2.7, and are useful in understanding the impeller hydrodynamics. When  $Fr < 0.045$ , the 3-3 structure does not form and the clinging-ragged transition is noted at the flooding-loading point without forming large cavities. When  $Fr > 0.045$ , the 3-3 structure is observed and then followed by ragged vibrating cavities at high gas flow numbers, at which flooding is accompanied by the

“3-3”-ragged transition.

According to Smith and Warmoeskerken (1985), the power curve has two distinguishing parts: (i) a convex part that occurs at low gas flow rates, and (ii) a concave part that occurs at higher gas flow rates. The inflection point corresponds to the transition from the vortex-clinging cavities to 3-3 cavity structures as shown in work by Warmoeskerken et al. (1981). In general, in low viscosity systems, the power draw at constant impeller speed falls as the aeration rate increases due to the growing cavity size. A short summary of the later work by Smith and Warmoeskerken (1985), according to the influence of various cavity structures on varying power demands, is presented in Fig. 2.8. The identified regimes are summarized accordingly:

- (a) A stable regime of six similar vortex cavities with a small power difference from that of the ungasged system;
- (b) A stable regime of six similar clinging cavities within a power decrease of at most 10% from that of the ungasged system;
- (c) A stable regime in which three large and three clinging cavities are formed where the power demand falls to about 40% of the original ungasged value;
- (d) A stable regime in which three large cavities are growing resulting in a lower power demand;
- (e) A stable regime in which six large cavities of two different sizes are formed resulting in very low power demand; and
- (f) An unstable regime caused by six vibrating ragged cavities which increases the power demand above the minimum value.

The transition from region (c) to region (d) is given by Eq. (2.10) and that from region (e) to

region (f) is well defined by Eq. (2.7).

By analyzing their data on the basis of the impeller hydrodynamics, Smith and Warmoeskerken (1985) developed gas holdup and gas-liquid mass transfer correlations for air-water systems in a vessel with  $T = 0.44$  m and  $D = 0.176$  m within a standard deviation of  $\pm 15\%$ , depending on whether the 3-3 regime had been established or not. The mass transfer correlations were presented for two distinct regions:

$$\frac{k_L a}{N} = 1.1 \times 10^{-7} F l_g^{0.6} Re^{1.1} \quad (\text{before large cavities are formed}) \quad (2.11)$$

$$\frac{k_L a}{N} = 1.6 \times 10^{-7} F l_g^{0.42} Re^{1.02} \quad (\text{after large cavities are formed}) \quad (2.12)$$

More recent work of Smith (1991) developed correlations from data obtained at different organizations using various impeller types and vessel sizes of  $T = 0.44$  m (hollow blade),  $T = 0.6$  m (Rushton), and  $T = 2.6$  m (with two different impellers). All data were derived for oxygen mass transfer from clean air-water systems. Their correlation was obtained for conditions in which the impeller operated in the large cavity regime for the majority of the collected data:

$$k_L a = 1.25 \times 10^{-4} \left( \frac{D}{T} \right)^{2.8} Fr^{0.6} Re^{0.7} F l_g^{0.45} \left( \frac{D}{g} \right)^{-0.5} \quad (2.13)$$

This correlation was found to fit data well for a wide range of vessel sizes (from  $T = 0.44$  to  $2.6$  m) with an rms deviation of 8% for all of the data points. This correlation is very sensitive to  $D/T$  ratio compared to the sensitivity of other terms in Eq. (2.13).

The hydrodynamics and power draw are interrelated and combined in more recent studies of gas dispersion because the gas cavities interfere with the mechanism of power transfer

from the blade to the liquid. It is more common to report the gassed to ungassed power ratio than to report the gassed power directly. Greaves and Barigou (1988) studied gassed power of a six-blade disk impeller in a vessel of  $T = 1.0$  m with  $c/T = 0.5$  and various impeller sizes of  $D/T = 0.25, 0.33,$  and  $0.5$  using air-water and air-electrolyte systems. They obtained power correlations as functions of flow regimes:

$$P_g = 441.4N^{3.13}Q_g^{-0.50}\left(\frac{D}{T}\right)^{5.82} \quad (\text{vortex-clinging cavity}) \quad (2.14)$$

$$P_g = 1737.1N^{2.99}Q_g^{-0.31}\left(\frac{D}{T}\right)^{5.98} \quad (\text{large cavity regime}) \quad (2.15)$$

No effects of the ionic properties of the different solutions were found. They also obtained a single power correlation but with more scatter compared to the correlations that account for different flow regimes. This work helped in understanding the dependence of flow regimes for successful aerated STR scale-up analysis, leading some researchers to study gas-liquid flow maps for STRs, which will be described next.

#### 2.3.4 STR Gas-Liquid Flow Regime Maps

For geometrically similar vessels, Warmoeskerken and Smith (1984a) suggested the flooding-loading transition is governed by a linear relationship of the form:

$$Fl_g = C_1 Fr \quad (2.16)$$

The constant in Eq. (2.16) was experimentally determined to be  $C_1 = 1.2$  for vessel diameters  $T = 0.44, 0.64,$  and  $1.2$  m, and impeller size of  $D/T = 0.4$ . However, this value of  $C_1$  applies only for this particular  $D/T$  ratio because, as shown by Nienow et al., (1985) and Eq. (2.7),

$C_1$  is a strong function of impeller to vessel diameter ( $D/T$ ).

Smith and Warmoeskerken (1985) determined that at very high gas flow rates, the stable 3-3 structure will break down to six ragged vibrating cavities. This work that confirmed the transition to flooding occurred at the same time the change in cavity formation was observed. Subsequently, they produced a single diagram known as a “regime map” with transitions from different flow regimes identified for a given vessel. Figure 2.9 shows a gas-liquid flow regime map by Smith and Warmoeskerken (1985) for a vessel with  $T = 1.2$  m and a six-blade impeller of  $D/T = 0.4$ . Three possible flow regimes are identified in this map: (A) vortex and clinging cavities, (B) large or ragged cavities at flooding, and (C) 3-3 structure containing three clinging and three large cavities. The A-B transition was from vortex-clinging cavities to large ragged cavities caused by high gas flow rates and low impeller speeds, resulting in a low power demand and eventually flooding. The B-C transition occurred between the 3-3 cavity structure and the large ragged cavities. Typically, there was an increase in the power draw as flooding was reached because the vibrating ragged cavities were not streamlined. The A-C transition was between the clinging-vortex cavities and the 3-3 structure. It was a gradual transition with no abrupt changes in power draw and it was associated with the inflection point in the power curve (e.g., see Fig. 2.7). The transitions A-B, B-C, and A-C were independent of whether the system was coalescing or noncoalescing, which agreed with the fact that cavities were independent of changes in surface tension (Bruijn et al., 1974). This implies that various cavity types are very important because they affect the power demand, the gas-liquid hydrodynamics around the impeller blades, and also form the interfacial area necessary for gas-liquid transport.

## 2.4 Gas-Liquid Mass Transfer

This section is subdivided into four major parts and is concerned with the gas-liquid mass transfer and the different methods in obtaining volumetric mass transfer coefficients. The first part will discuss mass transfer measurement methods. The second part will summarize the literature on oxygen-liquid mass transfer that will be later used for comparison with the bench-top scale vessel studies from this work. Parts three and four will address the limited literature on carbon-monoxide and syngas mass transfer rates, respectively.

### 2.4.1 $k_L a$ Measurement Methods

The methods used in the determination of the volumetric mass transfer coefficient ( $k_L a$ ) for oxygen can be divided into dynamic and steady state methods. The most commonly used  $k_L a$  measurement method is the dynamic-gassing out method with the mass transfer rate governed by the following relationship:

$$\frac{dC}{dt} = k_L a(C_i - C) \quad (2.17)$$

Linek et al. (1987) critically reviewed and experimentally verified the correct way of using the dynamic method to determine oxygen transfer in aerated agitated vessels. Typically there are semi-batch and batch dynamic-gassing out methods. In the semi-batch method, there is an instantaneous interchange of sparged gases with different oxygen concentrations at the same gas flow rates and impeller speeds which allows for a continuous gas holdup. The most common interchanges are  $N_2$  to  $O_2$  ( $N_2 \rightarrow O_2$ ) and  $N_2$  to air ( $N_2 \rightarrow \text{Air}$ ). In the batch method, the liquid is completely purged from  $O_2$  by  $N_2$  saturation then the agitation and the

gas flow rate are interrupted to allow bubbles to escape. Next, agitation is restarted and the gas flow rate is introduced with a different O<sub>2</sub> concentration from either air or pure O<sub>2</sub> gas. Alternatively, the liquid phase may be deoxygenated by either vacuum desorption or reaction with sulphite ions prior to sparging.

Steady state methods are widely used in dissolved oxygen measurements such as those by Gogate and Pandit (1999), Konig et al. (1979), Hickman (1988), Martin et al. (1994), and some are reviewed by Riggs (2004). Such methods involve a constant dissolved oxygen concentration in the liquid phase (i.e.,  $dC/dt = 0$ ). In order to achieve steady state, O<sub>2</sub> must be continuously removed from the liquid by a chemical or biochemical reaction with continuous gas flowing to the liquid phase. A common method is to continually replace the liquid phase with deoxygenated liquid involving two vessels with one purging and the other adding O<sub>2</sub>. Common chemical methods use sulphite oxidation and hydrazine (Zlokarnik, 1978). Some biochemical methods have used yeast respiration (Hickman, 1988) and some glucose oxidation. In general, chemical methods may introduce large errors in  $k_L a$  values if small errors are made in the concentration measurements of the liquid phase. Some chemical methods utilize complex reaction kinetics with the introduction of a specified chemical which are time intensive, making them overly complex. The hydrazine technique involves the reaction between hydrazine and oxygen according to:



Large discrepancies exist between the dynamic and chemical methods in the literature. Linek et al. (1990) found that the hydrazine method yielded, on the average, 25% higher  $k_L a$  values compared to the dynamic method, while the feeding steady state-method (FSM) using

$\text{Na}_2\text{SO}_3$  agreed with those from the dynamic method using air-nitrogen exchange. However, a simple steady state method with low chemical addition described by Hickman (1988), which does not require an assumption of a well-mixed liquid phase, was found to agree with the dynamic-gassing out method used in this study and with various data reported in literature, as discussed in Section 4.2.3. Hickman's steady state chemical technique known as "NEL/Hickman" utilized decomposition of hydrogen peroxide in the presence of an enzyme catalase according to:



This method relies on the transfer of oxygen into the liquid phase from decomposing hydrogen peroxide. The NEL/Hickman chemical method makes  $k_L a$  easy to determine since the reaction rate, the catalase concentration, and the hydrogen peroxide concentration in the reactor do not have to be known. All that is required is the liquid volume, inlet and exit gas flow rate, and the dissolved oxygen and hydrogen peroxide concentration at steady state (Hickman, 1988).

## 2.4.2 Oxygen-Liquid Mass Transfer

Knowing the gas-liquid mass transfer rate is very important to the design and scale-up of STRs. Despite many attempts in correlating  $k_L a$  for gas-liquid systems in STRs, there are large discrepancies in the literature and very little bench-top data predict industrial-scale operations. The existing volumetric mass transfer correlations are based either on nondimensional groups in the form  $k_L a = f(\text{Re}, \text{Fr}, \text{Fl}_g, D/T, \text{etc.})$ , or in the form of Eq. (2.6), which represents the Kolmogoroff's theory of energy input criteria (Yawalkar et al., 2002b).

Smith et al. (1977) measured gas-liquid mass transfer rates in baffled agitated tanks using air-water systems over a wide range in vessel diameters ( $T = 0.61, 0.91$  and  $1.83$  m), including industrial-scale, with a variety of agitator sizes (i.e.,  $D/T = 0.33, 0.5$ ). A volumetric gas-liquid mass transfer coefficient ( $k_L a$ ) for coalescing air-water systems was correlated to power density ( $P_g/V$ ) and superficial gas velocity ( $U_g$ ) in the form:

$$k_L a = 0.01 \left( \frac{P_g}{V} \right)^{0.475} U_g^{0.4} \quad (2.20)$$

In their study, a log-log plot of  $k_L a/U_g^{0.4}$  versus  $P_g/V$  did not follow a straight-line relationship at high power values. The non-linearity at constant  $U_g$  was assumed to be due to ineffective gas dispersion by the agitator. Several researchers have proposed correlations for the minimum impeller speed ( $N$ ) required for the agitator to be effective in dispersing gas and encouraging gas-liquid mass transfer (Westerterp et al., 1963; van Dierendonck et al., 1968; van't Riet et al., 1975; Nienow, 1977). However, the volumetric mass transfer data of Smith et al. (1977) for various tank sizes ( $T = 0.61, 0.91,$  and  $1.83$  m) were correlated at much lower impeller speed corresponding to incomplete gas dispersion. Thus, it can be concluded that most of the  $k_L a$  data taken by Smith et al. (1977) were for incomplete gas dispersion in the liquid. Their results also suggest that if the power input by the gas stream was accounted for, the data would follow a straight line, but with more scatter, and that the concern over minimum conditions for effective gas dispersion would not be necessary.

Linek et al. (1987) reviewed different dynamic methods for measuring  $k_L a$  and suggested the best one for measuring dissolved oxygen in water, electrolyte solutions, and viscous liquids. They measured the dissolved  $O_2$  concentration in tap water by interrupting the gas

flow and stirrer speed for the time necessary for bubbles to escape from the vessel, and successfully correlated  $k_L a$  in the form of Eq. (2.6) based on only one tank size ( $T = 0.29$  m). Linek et al. (1987) found good agreement with data of Smith et al. (1977), Fuchs et al. (1971), and Pollard (1978) with vessels of different size. In later work, Linek et al. (1989) showed a very good agreement between the pressure method and the standard dynamic method for dissolved oxygen measurements in coalescing water batch systems. They compared  $k_L a$  values using the pressure method when either pure oxygen or air is absorbed and found the absorption of pure oxygen and air to be identical. However, they also showed that for coalescing air-water systems, various incorrect techniques give practically the same  $k_L a$  values.

Chandrasekharan and Calderbank (1981) studied scale-up of aerated mixing vessels and presented their data in tabular form. The analysis of their data for mass transfer measurements in a large aerated mixing vessel ( $T = 1.22$  m) correlated very well to the power density and superficial gas velocity. Unfortunately, their own data for  $T = 1.22$  m, and earlier data from Figueiredo and Calderbank (1979) for  $T = 0.38$  and  $0.91$  m, resulted in a conclusion that scale-up is complex and difficult to predict based on small-scale measurements. They reported that scale-up at constant  $P_g/V$  and  $U_g$  does not predict the correct  $k_L a$  values, and that the constants  $C_1$ ,  $\alpha$ , and  $\beta$  of Eq. (2.6) are dependent on the scale of operation.

Figueiredo and Calderbank (1979) have pointed out that most of the scale-up criteria for the volumetric mass transfer coefficient in the form of Eq. (2.6) have been based on incorrect  $k_L a$  values. They modeled the solute mass balances according to several models (i.e., model I, II, III, and IV as defined in their study), which resulted in large differences in  $k_L a$

measurements. Subsequently, Linek et al. (1987) concluded that the  $k_{La}$  measurement method used by Figueiredo and Calderbank (1979) and their associated  $k_{La}$  values for  $T = 0.91$  are incorrect. The assumption of a quasi steady state in the gas phase lead to large errors in  $k_{La}$  for  $T = 0.91$  m vessel. This study will show that data obtained by method III for  $T = 0.91$  m by Figueiredo and Calderbank (1979) are in a good agreement with data by Chandrasekharan and Calderbank (1981) for a  $T = 1.22$  m tank, both of which are used in the overall correlation proposed in Chapter 4.

Pilot plant experiments usually relate mass or heat transfer rates to impeller operation and gas holdup (Calderbank, 1959; Rushton and Oldshue, 1953). Yawalkar et al. (2002a) critically studied the gas holdup in air-water STRs, and correlated their data with many other researchers using the energy input criteria. Their gas holdup correlation based on 122 data points with an  $R^2 = 0.81$  and a standard deviation of  $\pm 28\%$ . Their data showed a significant scatter around the correlating line with a maximum deviation of  $\pm 50\%$ . Using the definition of a minimum impeller speed for complete gas dispersion ( $N_{CD}$ ), as defined by Nienow et al. (1977), they attempted to provide a single correlation to predict the gas holdup on industrial scales over a wide range of geometric configurations and operating parameters. It was suggested by Nienow et al. (1977) and Chapman et al. (1983) that during scale-up, it is advantageous to define gas flow rate in terms of volumetric gas flow rate per minute per unit of liquid volume in the vessel (vvm), the inverse of the mean gas residence time, rather than in terms of  $U_g$ . The vvm approach is more commonly expressed in fermentation technology with  $vvm = 60Q_g/V$ . Therefore, Yawalkar et al. (2002a) regressed the gas holdup in the form:

$$\varepsilon = C_1 \left( \frac{N}{N_{CD}} \right)^\alpha vvm^\beta \quad (2.21)$$

The relative dispersion parameter  $N/N_{CD}$  is a key in the Yawalkar et al. study, and it represents the degree of gas dispersion at impeller speed  $N$  with respect to the impeller speed at which complete gas dispersion occurs ( $N_{CD}$ ) in the STR. They obtained a single gas holdup correlation over a wide range of system configurations and operating parameters:

$$\varepsilon = 0.104 \left( \frac{N}{N_{CD}} \right)^{0.62} vvm^{0.64} \quad (2.22)$$

This correlation has an  $R^2 = 0.90$  and the standard deviation of  $\pm 15\%$ . Yawalkar et al. (2002a) successfully predicted gas holdup over various vessel sizes from  $T = 0.57$  to  $2.7$  m with a maximum deviation of  $\pm 30\%$ . Equation (2.22) implies that for a given  $vvm$  and  $N/N_{CD}$ , gas holdup was approximately independent of tank size, impeller type,  $D/T$ ,  $C/T$ , type and location of sparger, and operating parameters.

As mentioned before, the volumetric mass transfer coefficient is directly proportional to gas holdup (Calderbank, 1959; Rushton and Oldshue, 1953); therefore, Yawalkar et al. (2002b) attempted to correlate  $k_L a$  with the dispersion parameter  $N/N_{CD}$  and superficial gas velocity  $U_g$  in the form:

$$k_L a = C_1 \left( \frac{N}{N_{CD}} \right)^\alpha U_g^\beta \quad (2.23)$$

They analyzed  $k_L a$  data available in the literature, two of which are discussed below (i.e., Bakker and van den Akker, 1994; Zhu et al., 2001), using the relative dispersion parameter  $N/N_{CD}$  for a wide range of STR sizes ( $T = 0.29$  to  $2.7$  m) equipped with six bladed standard

disc turbine (6DT), an A315 impeller, or a pitched blade turbine (PBT impeller). They observed approximately the same  $k_L a$  values at a given superficial gas velocity ( $U_g$ ) and particular  $N/N_{CD}$  parameter for various geometric configurations (i.e., reactor size, impeller type and size, sparger type, etc.). A correlation proposed by Yawalkar et al. (2002b) correlated almost all  $k_L a$  data points to within  $\pm 22\%$  for a wide range of STR sizes. This correlation had the form:

$$k_L a = 3.35 \left( \frac{N}{N_{CD}} \right)^{1.464} U_g \quad (2.24)$$

As suggested by Yawalkar et al. (2002b) the relative dispersion parameter  $N/N_{CD}$  was reliable in correlating and estimating hydrodynamic and mass transfer properties of gas-liquid STRs.

Bakker and van den Akker (1994) studied gas-liquid dispersion and mass transfer as a function of power consumption in a STR ( $T = 0.444$  m). They focused on the gas-dispersion of axial flow impellers such as a pitched blade turbine (PBT), a Lightnin A315 hydrofoil impeller, and a Leeuwrik impeller by linking power consumption and mass transfer to the flow pattern and the impeller hydrodynamics. Their  $k_L a$  values were correlated by Yawalkar et al. (2002b) to the relative dispersion parameter  $N/N_{CD}$  and found to be independent of the impeller type. The impeller speed at complete dispersion was determined from the power curves presented in their study.

Zhu et al. (2001) used the dynamic gassing out method to measure oxygen mass transfer rates in de-ionized water in a  $T = 0.39$  m diameter vessel. They studied six different impeller types (i.e., Lightnin A315 and A310, 45 degree pitched blade turbine, concave blade turbine,

Ruston turbine, and Ruston turbine with holes) under the same operating conditions, and correlated  $k_L a$  using the form of Eq. (2.6). Zhu's correlation (2001) was found to be in reasonable agreement with previous publications such as those of Linek et al. (1987), Hickman (1988), Warmoeskerken and Smith (1989), van't Riet (1979), etc. Their data were within  $\pm 30\%$  of previously published data by van't Riet (1979), which supports the previous claim that for given values of specific power and superficial gas velocity, approximately the same mass transfer rate can be achieved independent of impeller type. However, that was only possible at particular operating conditions, and not for all the covered data ranges in the associated studies, unless empirical constants in Eq. (2.6) were changed.

### 2.4.3 CO-Liquid Mass Transfer Rates from Syngas

Anaerobic bacteria may be utilized in fermentation of syngas components (i.e., CO, CO<sub>2</sub>, H<sub>2</sub>) to produce methane, acetate, methanol, butanol, and many other types of fuels and chemicals. In bench-top STRs, these fermentations are mass transfer limited due to very low gas solubilities. The increase in gas-liquid mass transfer leads to an increase in product production, and the type of bacteria used implies the type of product generated. Traditionally, to increase the syngas-liquid mass transport, the impeller speed is increased. Following is a literature survey on syngas-liquid mass transfer rates being important in syngas conversion and production.

Klasson et al. (1992) compared ethanol, hydrogen, and methane production in a continuously stirred tank reactor (CSTR), trickle-bed reactor (TBR), and packed-bubble column using syngas as the major carbon monoxide source. *Clostridium ljungdahlii* was used in converting CO, H<sub>2</sub>, and CO<sub>2</sub> to a mixture of acetate and ethanol with the use of

various reducing agents. When benzyl viologen was used as a reducing agent, the highest molar ratio (ethanol/acetate) of 1.1 was observed from all the batch experiments. However, in the two-stage continuous CSTR culture product ratios of ethanol to acetate reached 4:1 on a molar basis. In the production of methane, a two step process was used: formation of the methane prosecutors (acetate or hydrogen) and the biomethanation of the methane prosecutors employing the cultures of *Rhodospirillum rubrum* and *Methanobacterium formicicum*. Production through H<sub>2</sub> with a co-culture of *R. rubrum* and methanogens gave faster methane production rates through the water-gas-shift reaction. A simultaneous conversion of CO<sub>2</sub> and H<sub>2</sub> directly to CH<sub>4</sub> was obtained employing *M. formicicum* according to the metanation reaction:



The methane production rate reached steady state at about 1.6 mmol CH<sub>4</sub> h<sup>-1</sup>, which yields about 96% of the theoretical methane amount from the CO, H<sub>2</sub>, and CO<sub>2</sub> mixture. Klasson et al. (1992) measured 80% CO conversion in the TBR, or twice as high as the CSTR for a fermentation time of one hour. They concluded that a TBR packed with ceramic saddles gave higher conversions and higher productivities than a CSTR or bubble column. However, in the CSTR studies, CO mass transfer rates increased by 360% (from 28 to 101 h<sup>-1</sup> CO) when the agitation rate was increased by only 50% (from 300 to 450 rpm). Note that in gas-liquid mass transfer of sparingly soluble gases, such as CO, the primary resistance to gas transport is in the liquid film at the gas/liquid interface (Vega et al., 1989a; 1989b); therefore, it is desired to investigate the CSTR performance at higher agitation.

Cowger et al. (1992) used *R. rubrum*, an anaerobic photosynthetic bacterium capable of

caring out the water-gas-shift reaction, to produce hydrogen. This reaction is described by:



This reaction is important in shifting synthesis gas from CO-rich to H<sub>2</sub>-rich syngas since H<sub>2</sub> is typically a small fraction of syngas composition. Their work discussed the performance of *R. rubrum* in continuous stirred tank reactor (CSTR) and a trickle-bed reactor with emphasis on mass transfer and reaction kinetics in modeling reactor performance. All experiments were carried out at 30°C and pH 7. The sparger gas was continuously fed to each reactor as a mixture of H<sub>2</sub>, Ar, CO, and CO<sub>2</sub> (20/15/55/10%). Their results show the conversion of CO independent of cell concentration and dependent on the liquid recycle rate. For both reactors, the conversion of CO increased with increasing the liquid recycle rate at a constant gas flow rate. They concluded that the main resistance in the uptake of CO was explained by the CO mass transfer to the cells, since CO conversion was not affected by cell concentration level. However, Cowger et al. (1992) suggested additional experiments at different cell concentration levels in order to further understand any mass-transfer and/or kinetic limitations.

Klasson et al. (1993a; 1993b) expanded the work of Cowger et al. (1992) in studying *R. rubrum* for its ability to convert CO and water to CO<sub>2</sub> and H<sub>2</sub>. They studied the effect of different syngas phase compositions (N<sub>2</sub>, CO<sub>2</sub>, He, CO) with and without the CO gas component present and showed no H<sub>2</sub> production when CO was omitted from the gas composition. Klasson et al. (1993a) reported 87% conversion rate of CO to H<sub>2</sub> by *R. rubrum*. In other work, Klasson et al. (1993b) employed a non-steady state method using a modified Mond equation in order to separate mass transfer and kinetic limited regions of the

fermentation. They measured CO mass transfer rates from 15 to 35 h<sup>-1</sup> for an agitation rate range of 300-700 rpm. Klasson et al. (1993b) showed that the limiting factor for hydrogen production was not the metabolism of *R. rubrum*, but the mass transfer of CO into water with the main resistance in the liquid film at the gas/liquid interface. Their work determined that the maximum CO conversion was not limited by cell concentration, but by agitation rate, gas flow rate, and gas inlet composition.

Bradwell et al. (1999) discussed reactor design issues in anaerobic synthesis gas fermentation for the production of methane, organic acids, and alcohols. They found, on average, the highest CO mass transfer rates in TBR compared to CSTR and packed-bubble columns using different biological systems (i.e., *C. ljundahlilii*, *R. rubrum*, *M. formicium*, *M. barkeri*, SRB mixed culture) with either pure CO, or syngas as a feedstock. In the CSTR, the impeller speed varied from 200 to 450 rpm and gave  $k_La$  values from 14.2 to 101 h<sup>-1</sup>, while the TBR gave  $k_La$  values from 55.5 to 137 h<sup>-1</sup> for CO mass transfer. The use of a packed-bubble column resulted in an inefficient operation of gas-liquid transport with the volumetric mass transfer coefficient of 2.1 h<sup>-1</sup>.

Since the solubilities of CO and H<sub>2</sub> are low, syngas fermentations are typically limited by the gas-to-liquid mass transfer; hence, a microbubble dispersion method was proposed to enhance gas-to-liquid mass transfer (Sebba, 1987). In a CSTR operated at 200 rpm, a six fold increase was observed in  $k_La$  from 14.2 h<sup>-1</sup> (using conventional bubbles) to 90.6 h<sup>-1</sup> (using microbubble dispersion). This increase in  $k_La$  for a microbubble dispersion was achieved despite using a gas flow rate of half that used for conventional bubbles. Similarly, Kaster et al. (1990) measured a four fold increase in  $k_La$  values using a microbubble sparging compared to conventional sparging. In general, the results showed a several-fold increase in

the productivity of syngas fermentation using microbubble dispersions for all reactor types.

Since a common approach to enhance mass transfer rates is to increase the degree of mixing, stirred tank reactors have been extensively used for syngas fermentations in the laboratory because high  $k_La$  values can be achieved at high power densities ( $P_g/V$ ). However, increasing power density is not always economically feasible for very large reactors due to the power costs. Therefore, this work will address the gas-liquid mass transfer measurements in a bench-scale stirred tank reactor ( $T = 0.211$  m) at various operating conditions and predict the mass transfer rate in large-scale reactors being considered for commercial syngas fermentation.

## 2.5 Literature Review Summary

Gas-liquid mass transfer rates and the associated hydrodynamics of STRs for oxygen studies have been extensively reviewed, since such phenomena are important and can be applied in syngas-liquid mass transport. A great deal of work has been done, particularly in the area of STR scale-up, which will be used in Chapter 4 when syngas mass transfer scale-up is discussed. Determination of actual syngas-liquid mass transfer rates and STR scale-up for industrial-size vessels are of great importance in syngas fermentations necessary to commercially produce fuels and chemicals. Although oxygen and syngas mass transfer rates differ, the syngas-liquid mass transfer can be predicted from oxygen mass transfer rates at similar STR operating conditions. The work of this thesis will complete these studies, and is part of a long term research effort to ultimately produce fuels and chemicals through syngas fermentation.

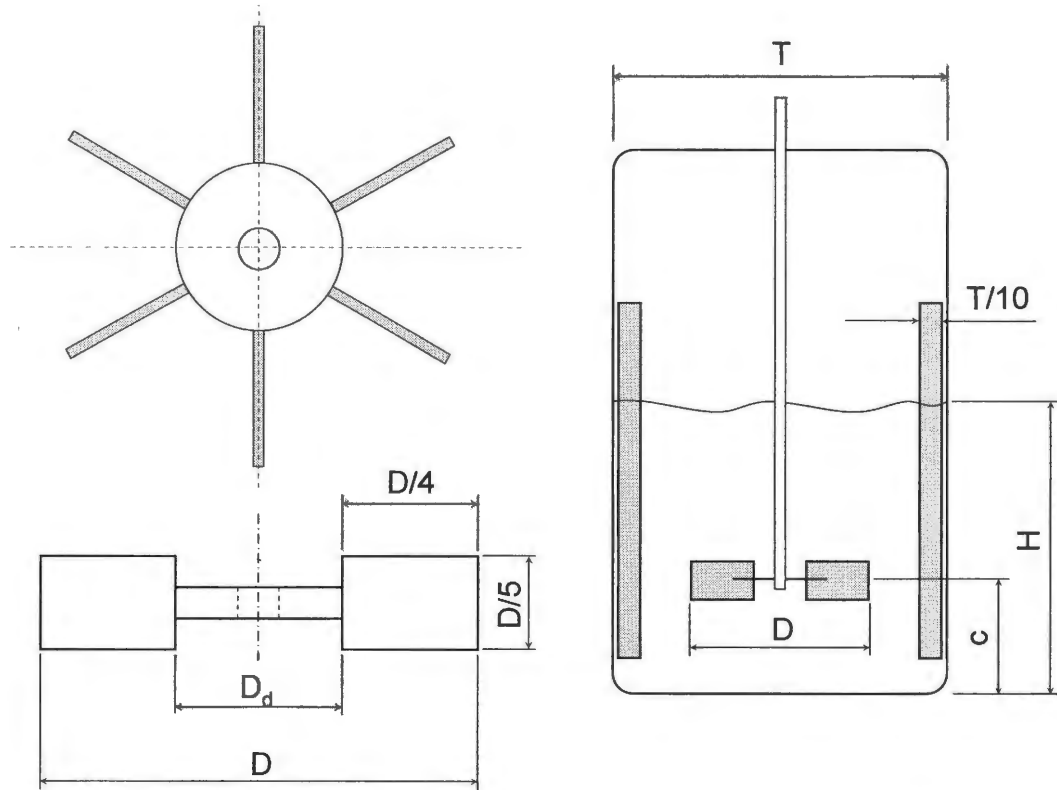


**Figure 2.1:** Standard vessel geometry fitted with a Rushton disc-turbine (6DT).

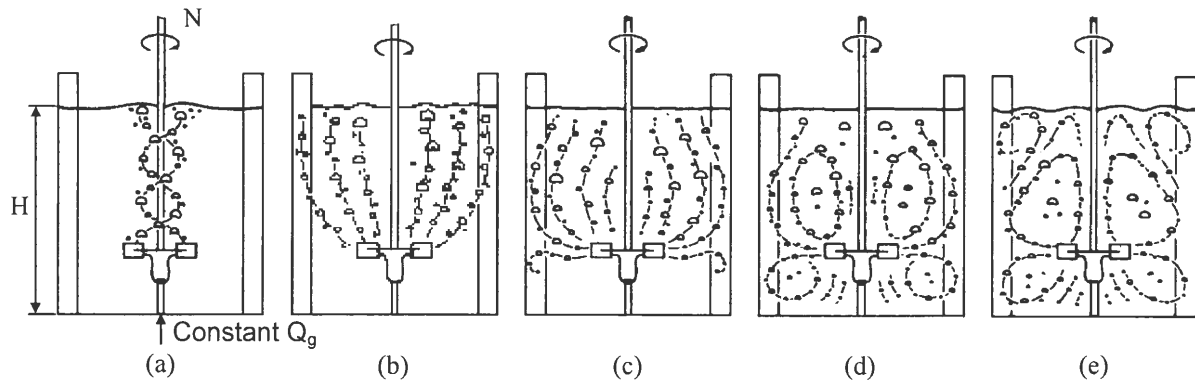


**Figure 2.2:** Bulk flow patterns at constant gas flow rate ( $Q_g$ ) with increasing impeller speed  $N$  (Nienow et al., 1985).

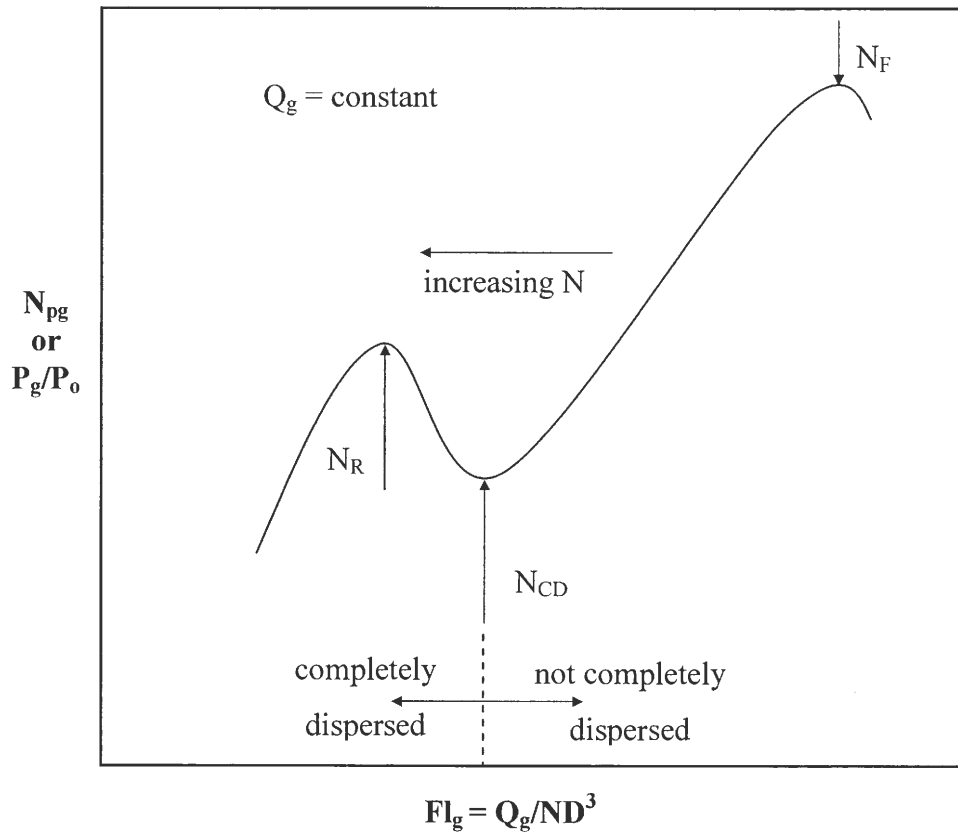


**Figure 2.3:** Generic gassed power number as a function of flow number for gas-liquid dispersion in STR systems with  $Q_g = \text{constant}$  (adopted from data by Nienow et al., 1977).

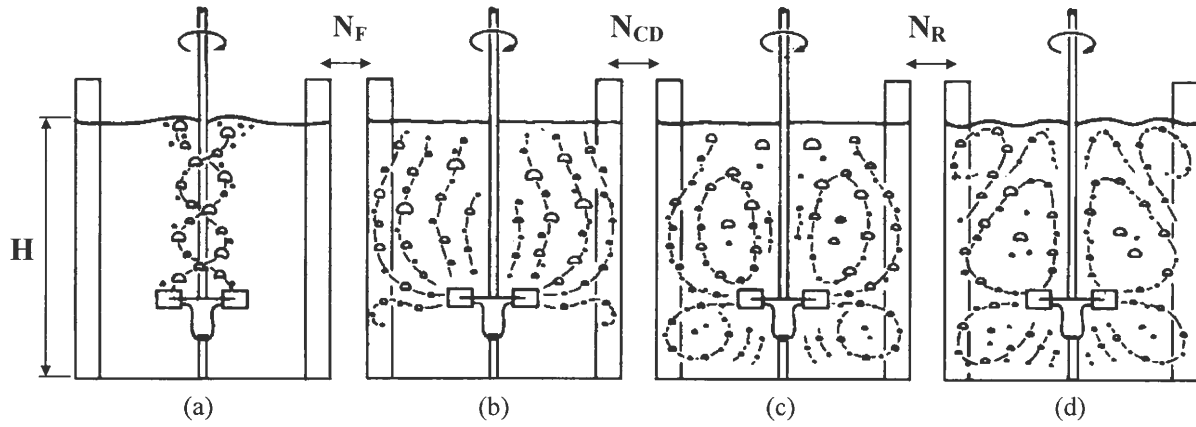


**Figure 2.4:** Main bulk flow regime transitions of a gas-liquid dispersion in a standard STR (adopted from Nienow et al., 1985).

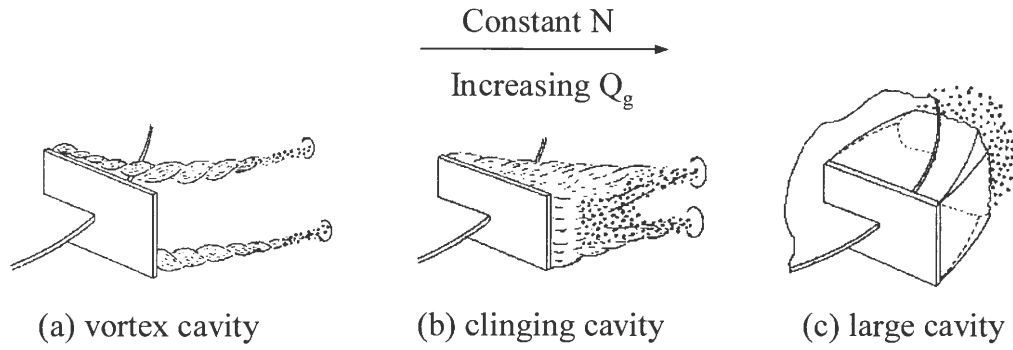


**Figure 2.5:** Cavity changes at constant  $N$  with increasing  $Q_g$  (Smith and Warmoeskerken, 1985).

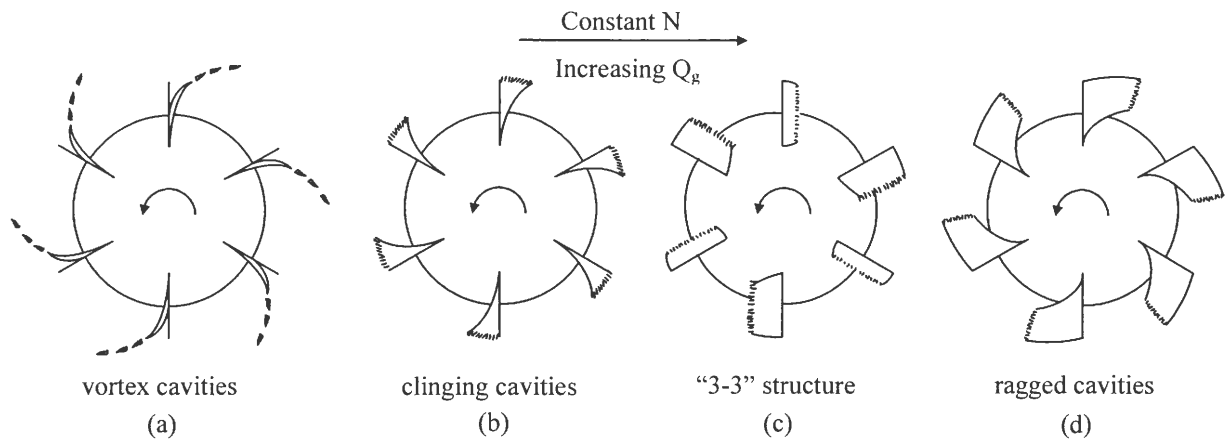


**Figure 2.6:** Cavity systems with increasing  $Q_g$  at constant  $N$  (Smith and Warmoeskerken 1985, and Nienow et al., 1985).

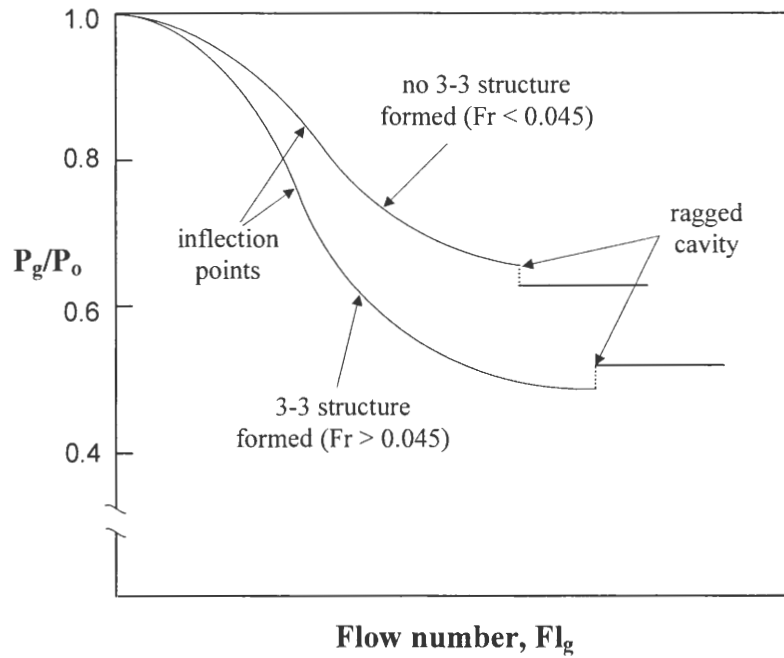


**Figure 2.7:** Gassed power ratio at constant impeller speed  $N$  (Nienow et al., 1985).

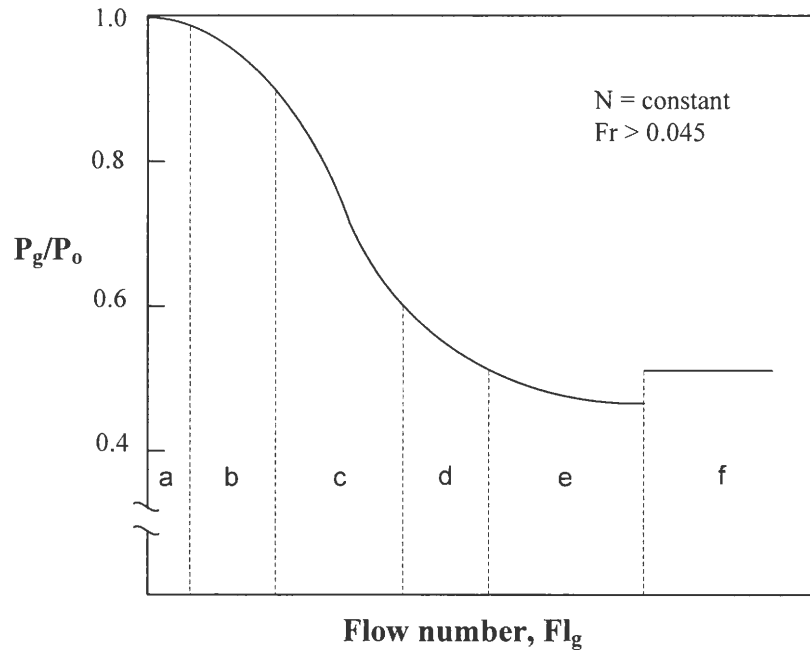


**Figure 2.8:** Gassed power curve with cavity formation (adopted from Smith and Warmoeskerken, 1985).

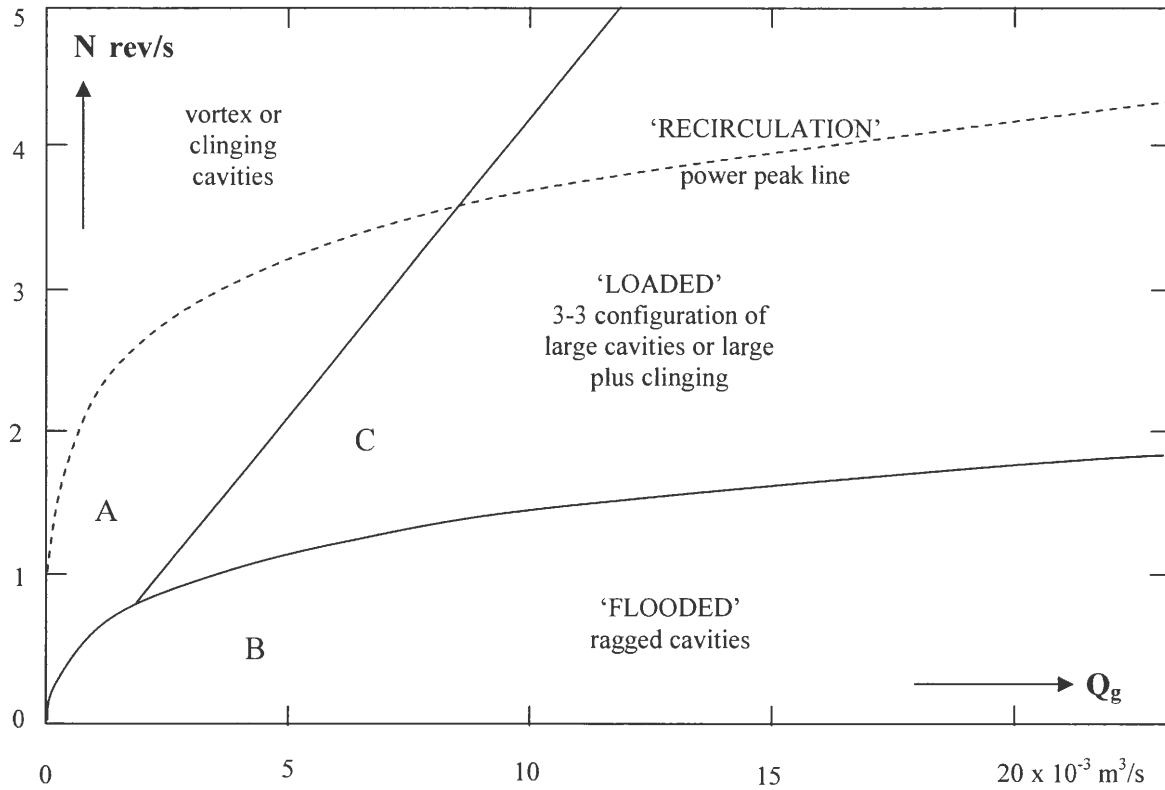


**Figure 2.9:** General flow map for  $T = 1.2$  m tank and  $D = 0.48$  m impeller (Smith and Warmoeskerken, 1985).

## CHAPTER 3: MATERIALS AND METHODS

### 3.1 Experimental Setup

Experiments are carried out in a BioFlow 110 Fermenter (New Brunswick Scientific Co., Edison, NJ), which is a dished bottom cylindrical vessel of diameter  $T = 0.211$  m filled with water to a height equal to the vessel diameter ( $H = T$ ). A six-bladed Rushton disc turbine of diameter  $D = 0.0747$  m ( $D/T = 0.35$ ) is used at a constant clearance ratio of one quarter the static liquid height above the base of the tank ( $c = H/4$ ). The impeller blade dimensions and all other vessel geometric factors in the system correspond to the well known standard vessel configuration (Holland and Chapman, 1966). A schematic of the vessel geometry and the entire experimental facility is given in Fig. 3.1. All work was done in a single 7 liter working volume, corresponding to  $H = T$ , glass stirred tank vessel fitted with a stainless steel top plate and four equally spaced baffles, at a width of  $T/10$ . The STR is maintained at a constant temperature ( $25^{\circ}\text{C}$ ) using a heat blanket and recirculating water bath. The impeller is driven by a variable-speed DC motor which is connected to the Primary Control Unit (PCU) of the BioFlo 110 Fermenter for dissolved oxygen measurements, or to an AC/DC converter for power measurements. A DC power meter is used for power measurements that are corrected for shaft friction, bearing losses, and electrical power losses; details of the power measurements will be discussed next.

### 3.2 Power Consumption Measurements in a STR

In this section various methods for measuring mechanical power will be introduced, and electrical power measurements will be discussed in more detail. The losses in the electric motor and shaft bearings are accounted for and experimentally determined.

Several methods can be used to obtain STR power measurements in dispersed gas-liquid systems, including air-bearing dynamometers, torque transducers, and electrical power measurements. The in-line torque transducer principle is one of the easiest ways of measuring the applied torque on the electric motor shaft, but it was not easily adaptable for our system because it must be mounted between the electric motor and the shaft.

Air-bearing dynamometers were discussed in detail by Nienow and Miles (1969), where either the motor or the vessel is mounted on a floating thrust plate and allowed to turn freely on its axis while the other component is held fixed. In the case of a floating motor with a fixed vessel, the motor will turn in the opposite direction of the impeller rotation due to the liquid force on the impeller. This allows for a direct torque measurement by the use of a resistant couple that is applied to stop the motor rotation. If the motor is fixed and the vessel is allowed to rotate about the vertical axis, a coil spring with the calibration scale can be used to measure the applied torque on the shaft. In either method the mechanical power is calculated from the following formula:

$$P_{\text{mech}} = T_{\text{mech}} (2\pi N) \quad (3.1)$$

In direct torque measurements, both of these methods are independent of the type of electric motor used, however, one should account for the frictional losses in the air-bearing systems.

If mechanical power is to be obtained by electrical power measurements, it is preferred to

use a motor operating with a direct current (DC) such that impeller speed (N) can be adjusted by applying a constant voltage potential across the DC motor. An Electro (model PS-5R) AC/DC converter is used to supply the STR motor (Magmotor Corporation, model C32-E-450X) with a constant DC voltage. The electric motor in this study is manufactured by Magmotor Corporation, with model number C32-E-450X. It is a 2-pole design DC motor with a cylindrical stator (inductor) and a magnet which can excite an induced circuit (rotor) through which the constant current flows for a given voltage potential. The voltage potential is adjusted to maintain the impeller speed (N) at a desired level to within  $\pm 0.0167$  rev/s ( $\pm 1$  rpm) while the air flow rate ( $Q_g$ ) is held fixed.

The total electrical power absorbed by the induced circuit is calculated from  $P_{e,t} = EI$ , and losses due to joule heating are accounted for by  $P_{\text{joule}} = RI^2$ . Hence, the total electrical power transformed into mechanical power is given by  $P_e = P_{e,t} - P_{\text{joule}}$ , which is also called the electromagnetic power. The electromagnetic power can also be determined by  $P_e = K\phi I (2\pi N)$  where  $K\phi$  is a manufacturer supplied torque constant (0.6109 Nm/A). In addition to joule electrical losses, there are electrical losses due to hysteresis of the armature and mechanical losses due to friction on the bearings as well as windage losses. These other losses can be lumped together as mechanical torque losses ( $T_{\text{loss}}$ ) and easily determined by power measurements without a load on the impeller as a function of the impeller speed (Fig. 3.2). In this work, mechanical torque losses are assumed to be the same whether gassed or ungassed power measurements are to be determined. Therefore, mechanical power determined by electrical measurements is expressed by:

$$P_{\text{mech}} = (K\phi I - T_{\text{loss}}) 2\pi N \quad (3.2)$$

The impeller speed  $N$  of the DC motor is measured by a tachometer connected to the PCU and displayed on the screen of BioFlo 110 Fermenter. Once a steady impeller speed is reached for a desired gas flow rate, the current ( $I$ ), the voltage potential ( $E$ ), and the product of the two, which represents the DC electric power, are simultaneously sampled by a digital EXTECH True RMS Power Analyzer that is directly connected to a computer through an RS-232 interface for data logging. For each power measurement, 200 data points are recorded at a frequency of 2 Hz and mean values are reported as the final power values, and are repeatable within a maximum standard deviation of  $\pm 1.25\%$  from the mean. Typically, power measurements are reproducible to within  $\pm 0.5\%$ . The maximum uncertainty in the gassed power measurements at the full flow meter scale is estimated to be  $\pm 0.83\%$ , with the worst case percent uncertainties in measured gassed and ungassed power numbers of  $\pm 1.6\%$  and  $\pm 1.4\%$ , respectively.

### **3.3 Dynamic Gassing-Out Method for Dissolved Oxygen Concentrations**

The volumetric gas-liquid mass transfer rates for dissolved  $O_2$  measurements are determined using a dynamic gassing-out method (Linek et al., 1987; van't Riet, 1979; Zhu et al., 2001). Dynamic methods for  $k_L a$  measurements consist of recording concentration profiles as a function of time in the liquid following a step change in oxygen concentration in the inflowing gas. Dissolved oxygen concentrations are recorded using an InPro-6800 series polarographic type probe with a single layer silicon membrane cover for faster response

(Mettler Toledo, Woburn, MA). For all DO measurements, the probe is placed directly in the region of the impeller discharge, and the probe is calibrated each time at the same operating conditions at which the measurements are obtained. For a given test condition (i.e., a specified impeller speed and gas flow rate), the liquid is first deoxygenated by sparging nitrogen until a zero reading is reached. The nitrogen flow rate is then turned off and the impeller speed stopped to allow all the nitrogen bubbles to escape from the liquid. The impeller is then turned on and the three way valve controlling the gas supply is switched to air. Dissolved oxygen measurements are recorded with a fast response DO probe until the liquid is saturated with oxygen. The liquid saturation is reached in less than two minutes for most operating conditions.

The probe response time,  $\tau_p$ , is defined as the time needed to record 63% of a stepwise change, and for the proper DO probe functionality,  $\tau_p$  should be much smaller than  $1/k_L a$ . In practice, this is seldom the case and many different probes have been designed to account for response time. Van't Riet (1975) has demonstrated that in van de Sande's model, the ultimate error in  $k_L a$  is less than 6% when  $\tau_p \leq 1/k_L a$ . When the probe is described as a first order system, the response  $U_v$  of a probe with response time is given as (van de Sande, 1974):

$$U_v = b_p \left| C_i + (C_o - C_i) \left\{ \frac{1}{1 - \tau_p k_L a} \exp(-k_L a t) + \left( 1 - \frac{1}{1 - \tau_p k_L a} \right) \exp\left(-\frac{t}{\tau_p}\right) \right\} \right| \quad (3.3)$$

in which  $b_p$  is a constant ( $\text{Vm}^3 \text{kg}^{-1}$ ),  $C_i$  is the equilibrium concentration ( $\text{kgm}^{-3}$ ), and  $C_o$  is the concentration at  $t = 0$ . Equation 3.3 shows that the influence of  $\tau_p$  on the value  $U_v$  can be neglected when  $\tau_p \ll 1/k_L a$ . The actual  $U_v$  value is not important because  $k_L a$  is determined from the change in  $U_v$  with time. Table 3.1 compares actual values of  $k_L a$  with those that

would be measured by a probe response time  $\tau_p = 5$  s calculated from Eq. (3.3) (van de Sande, 1974). Comparison of  $k_L a$  values from Table 3.1 shows that although  $\tau_p$  is not much less than  $1/k_L a$ , the measured values do not differ significantly from the actual values.

**Table 3.1:** Actual  $k_L a$  values compared to  $k_L a$  values for  $\tau_p = 5$  s (van de Sande, 1974).

| $k_L a$ (s <sup>-1</sup> )<br>actual | $k_L a$ (s <sup>-1</sup> )<br>Eq. (3.3) | Deviation<br>% |
|--------------------------------------|---|----------------|
| 0.065                                | 0.065                                   | 0              |
| 0.08                                 | 0.078                                   | 2.5            |
| 0.10                                 | 0.094                                   | 6              |
| 0.12                                 | 0.11                                    | 8              |

A significant factor that affects the probe response time is the probe tip membrane type because O<sub>2</sub> must diffuse through the membrane body to be detected. Figure 3.3 shows a comparison of mass transfer measurements for Silicon and Teflon-type membranes. The Silicon-type membrane is a single layer coating membrane, while the Teflon-type membrane is a two layer coating membrane. The Teflon-type membrane is manufactured perhaps to last longer in fermentation processes and it is not suitable for transient measurements. Obviously, the Silicon-type membrane has higher  $k_L a$  values (Fig. 3.3) and an associated faster response time.

In this work a Silicon-type probe is used in the mass transfer measurements. The probe response time is determined by immersing the probe tip completely in a flow of pure nitrogen from a gas cylinder, then switching the flow to the air stream. Using this method, the response time is measured to be  $\tau_p \approx 7.5$  s, which is acceptable to obtain accurate volumetric gas-liquid mass transfer coefficients. For the range of  $k_L a$  values studied in this work ( $k_L a <$

0.06 s<sup>-1</sup>) and with the DO probe response about  $\tau_p \approx 7.5$  s, the deviation from actual  $k_L a$  values is less than 2% when compared to the  $k_L a$  range tested in Table 3.1.

The calculation of the volumetric mass transfer coefficients  $k_L a$  from the transient response curve assumes that:

- (i) the liquid phase is well mixed,
- (ii) gas absorption is liquid phase controlled, and
- (iii) the oxygen concentration in the liquid at the gas-liquid interface is in equilibrium with the oxygen concentration in the gas.

Hence, the dissolved oxygen concentration data are analysed to determine the mass transfer coefficient,  $k_L a$  based on the liquid phase model:

$$\frac{dC}{dt} = k_L a (C_i - C) \quad (3.4)$$

where  $C$  is the dissolved gas concentration in the liquid at time  $t$ , and  $C_i$  is the steady state gas concentration at the gas-liquid interface assumed to be in equilibrium with the bubble.

Integration of Eq. (3.4) yields:

$$C^* = \frac{C - C_o}{C_i - C_o} = 1 - \exp(k_L a (t - t_o)) \quad (3.5)$$

where  $C^*$  is the normalized dissolved oxygen concentration at time  $t$ ,  $C_o$  is the initial dissolved oxygen concentration, and  $t_o$  is the time at the initiation of air sparging. A typical dissolved oxygen concentration given by Eq. (3.5) is a first order response as a function of time. For a given test condition, the  $k_L a$  is determined using JMP 5.1 (SAS Institute, Inc.) by fitting the data with a first order response function. An example of dissolved O<sub>2</sub>

concentration data at an impeller speed of  $N = 400$  rev/min and a gas flow rate  $Q_g = 5$  L/min of air is shown in Fig. 3.4. Several replicates for each operating condition were completed and the resulting standard deviation was typically within  $\pm 2.3\%$  of the mean, with the maximum value of  $\pm 5.0\%$ .

### **3.4 Myoglobin Method for Dissolved Carbon Monoxide Concentrations**

This section will summarize a myoglobin-protein method for measuring dissolved pure CO in water that was used by Riggs (2004). Modifications to this method are necessarily to measure dissolved CO concentrations using artificial syngas as the stream gas. The associated measurement errors with this technique will be discussed and ways to eliminate them will be summarized.

#### **3.4.1 Experimental setup for CO measurements from syngas**

Syngas is modeled as a four component gas mixture of  $N_2$ ,  $H_2$ , CO, and  $CO_2$  having volume fractions of 52%, 10%, 20%, and 18%, respectively. The artificial gas is directly supplied to the STR from gas cylinders, as shown in Fig. 3.5, through a multi-gas component rotameter with a needle valve for precise flow rate control. The multi-gas component rotameter is a four-gas-inlet single-gas-exit device used to generate the artificial syngas mixture. The mixture is supplied to the STR through Tygon FEP-lined tubing to minimize gas diffusion through the tube walls. A Masterflex L/S peristaltic pump system is used for the Tygon LFL recirculation line (Fig. 3.5) and is capable of a maximum liquid pumping rate of 2.2 L/min. When the pump is operated at this maximum flow rate, it takes less than 0.5

seconds for the liquid to travel from the bottom of the tank to the sample port. The sample port (Fig. 3.6) consists of a Swagelok stainless steel union cross fitted with septa on both sides, and is connected via plastic (PFA) inline fitting to the recirculation line. The septa provide a place for a needle syringe to penetrate and withdraw a liquid sample. Ten micro-liter samples are withdrawn every 5 or 10 seconds, depending on the operating conditions (i.e.,  $N$ , and  $Q_g$ ) with gastight high performance syringes (Hamilton).

Dissolved carbon monoxide concentration samples are measured using a Cary-50 Bio spectrophotometer from Varian. The spectrophotometer is set-up to measure light absorption in the wavelength range 400 to 700 nm because the peak for myoglobin occurs at 423 nm. Myoglobin used in the dissolved CO concentration measurements is purchased through Sigma-Aldrich and is derived from horse heart as lyophilized powder at least 90% pure. Samples are prepared and scanned in 1.5 mL nominal volume semi-micro disposable Polystyrene cuvettes. These cuvettes have a 10 mm path length and are usable in the spectral range of 340 to 800 nm.

#### **3.4.2 Preparation and Collection of Liquid Samples**

Before collecting dissolved CO liquid samples, syringes numbered 1-15 are rinsed with water. All of the syringes are then injected into the sampling port as shown in Fig. 3.6. The syringe tips are located in the recirculation line while the recirculation pump is on. This allows for good liquid-needle contact, which aids in the syringe functionality. The size of the septa (12 mm) is chosen to easily accommodate eight samples on each side of the sampling port and to allow for easier plunger access. Great care is required when positioning the needle in the sampling port since the possibility of withdrawing small gas bubbles is high.

Any amount of bubbles collected in the liquid samples will give highly inaccurate CO concentrations; any samples that did contain any gas bubbles were immediately discarded. Any bubbles in the recirculation line are concentrated along the centerline of the recirculation stream. To account for undesired bubbles, a position of low bubble region is chosen as shown in Fig. 3.7. It is highly recommended that (i) the needles are previously positioned as shown in Fig. 3.7 which will eliminate bubbles from the samples, and (ii) all the needles are previously injected into the sampling port which will improve consistency in withdrawing the samples and therefore the accuracy in taking data itself.

The specified syngas flow rate of interest is adjusted prior the start of the experiment. After the syringes are positioned and the recirculation pump is on, the syngas valve mounted in the exiting stream of the multi-gas rotameter is opened. A digital stop-watch is started at the same time the syngas flow rate is initiated. A single 10  $\mu\text{L}$  liquid sample is collected every 5 or 10 seconds as needed. Two carbon monoxide saturated samples are taken approximately after 4-5 minutes of sparging syngas through the liquid. Usually the steady state is reached in less than 2 minutes as tested from multiple sample runs at low operating conditions.

### **3.4.3 Measuring Dissolved Carbon Monoxide Concentrations**

Riggs (2004) provided a detailed method for measuring pure CO dissolved in water. This method has been adjusted for dissolved CO measurements from artificial syngas, and summarized below. Additional comments for improvement are also provided.

### 1. Making deoxygenated buffer solution and preparing sample for analysis

Approximately 30 mL of potassium phosphate pH 7.0, poured into a small beaker, is used as a deoxygenated buffer solution. Every cuvette is then filled with 1 mL of this buffer solution. Sodium dithionite is added to the solution to deactivate any oxygen present in cuvettes. The solution is mixed by shaking the cuvette several times with the cap in place to ensure the sodium dithionite is dissolved. Anywhere from 4 to 8  $\mu\text{L}$  of myoglobin protein is added to the cuvette depending on the protein concentration strength (see step 2). The cuvette is again shaken to ensure proper mixing. The cuvette is then filled with 10  $\mu\text{L}$  of either CO saturated, deoxygenated, or trial sample and, again, gently shaken.

### 2. Identifying the protein concentration and spectra fitting

An extra sample of CO saturated solution from syngas previously taken can be used to find an amount of protein needed to obtain an absorption value from the spectrophotometer in the range 0.55-0.60 at the highest peak. The amount of protein added to the solution will depend on the prepared protein concentration strength. When analyzing pure CO, the absorption value is adjusted to around 1.5 at the highest peak, which gives much more resolution for sample analysis (Riggs, 2004). The CO contribution in artificial syngas is 20% of the pure CO condition and provides a lower resolution in the CO myoglobin technique. In other words, the absorption measured by the spectrophotometer for CO from artificial syngas is much less than the absorption of the pure CO gas due to an additional absorption of gas components from the syngas mixture. It is strongly recommended that: (i) each syringe is used for only one type of solution but not rinsed and used for other solutions (i.e., a syringe

for a buffer solution should not be used to analyse the saturated CO solution), (ii) when the amount of protein is injected there are additional droplets attached to the outside of the needle that require removal with a soft tissue to ensure the protein concentration is correct, and (iii) approximately the same amount of force is applied to the plunger while injecting samples for analysis.

After CO saturated and deoxygenated samples are analysed, the rest of the samples, corresponding to the transient data of CO concentrations, should fit altogether as shown in Fig 3.8. When the samples are analysed in the order as collected (i.e., 1,2,3,...,15), the peaks will start to shift to the left of the deoxygenated peak following the path designated by the arrow as shown in Fig. 3.8. Theoretically, no sample should overshoot the CO saturated sample, but it is possible to have small fluctuations due to the errors in injecting buffer and or protein which is typical for this type of method. Therefore, it is strongly recommended that the samples be analysed in order so that such errors can be detected. Choosing a syringe position as described above (i.e., in the low bubble region) greatly aids in omitting bubbles. However, it may be possible to still have a bubble in the needle itself (the metal part) which can not be visually detected. Such samples will overshoot the peak of the next sample to be analysed (e.g., if sample 5 overshoots sample 6), and they should be removed from the data set. The protein concentration is then determined from:

$$C_p = \frac{A}{l \cdot \epsilon_a} \quad (3.6)$$

where  $C_p$  is the protein concentration,  $A$  is the absorption value,  $l$  is the path length of the cuvette, and  $\epsilon$  is the absorption coefficient ( $\epsilon_a = 157 \mu\text{M}^{-1} \text{cm}^{-1}$  for myoglobin).

Spectra Solve is used to load all the samples between the deoxygenated and CO saturated peaks and the “Fit Shape” option in Spectra Solve interpolates a selected data cell between the two assigned cells (i.e., the two known concentration cells) and provides a percentage of similarity to each spectra. These data are used to determine the concentration in the sample through the following equation:

$$\text{Sample Concentration} = (\text{Protein Conc.})(\% \text{ of CO Sat. Spectra}) \left( \frac{\text{Total Cuvette Vol.}}{\text{Sample Vol.}} \right) \quad (3.7)$$

#### 3.4.4 Determining the $k_L a$ Values for CO Concentration Data from Syngas

Figure 3.9 shows a typical CO concentration data from artificial syngas as a function of time in a STR ( $T = 0.211$  m and  $T/D = 0.35$ ) at an impeller speed of  $N = 700$  rev/min and a gas flow rate of  $Q_g = 12$  L/min of syngas. The calculation of the volumetric mass transfer coefficients  $k_L a$  from the transient response curve includes the same assumptions as previously made for oxygen measurements. Integrating the mass transfer rate equation (Eq. (3.4)) to read:

$$\ln \left( \frac{C_i - C_o}{C_i - C} \right) = (k_L a)t + B \quad (3.8)$$

where  $B$  is a constant of integration and  $C_i$ ,  $C_o$ , and  $C$  are as defined in Section 3.3. Since the initial amount of dissolved CO in the liquid is zero,  $C_o$  can be neglected and Eq. (3.8) reduces to:

$$\ln \left( \frac{C_i}{C_i - C} \right) = (k_L a)t + B \quad (3.9)$$

Equation (3.9) is a straight line relationship with the slope equal to volumetric gas-liquid mass transfer coefficient ( $k_L a$ ). Figure 3.10 shows an example of the  $k_L a$  calculation, for CO dissolved in water, from the averaged data set in Fig. 3.9 at impeller speed  $N = 700$  rev/min and gas flow rate  $Q_g = 12$  L/min of syngas.

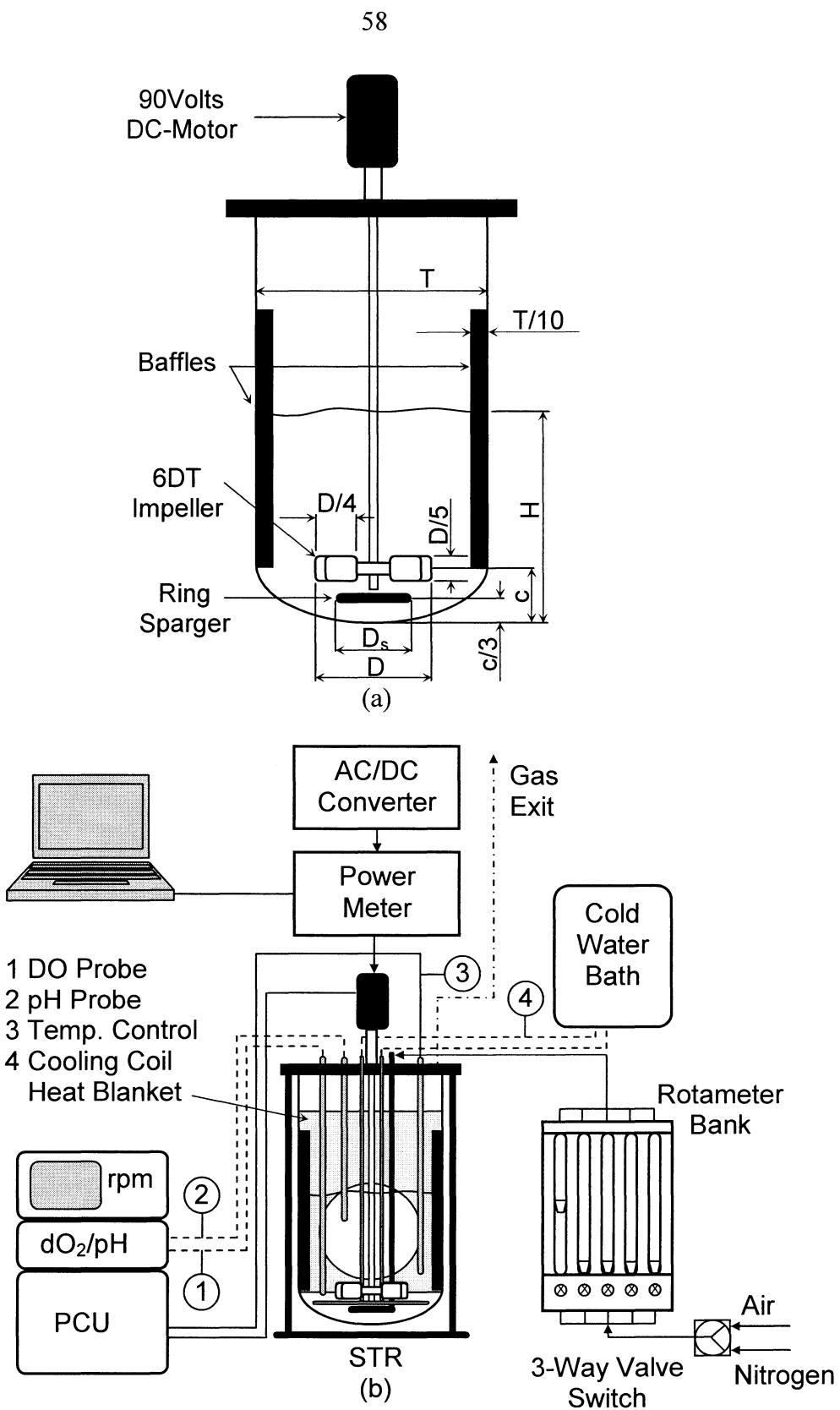


**Figure 3.1:** Experimental (a) stirred-tank reactor geometry and (b) facility setup.

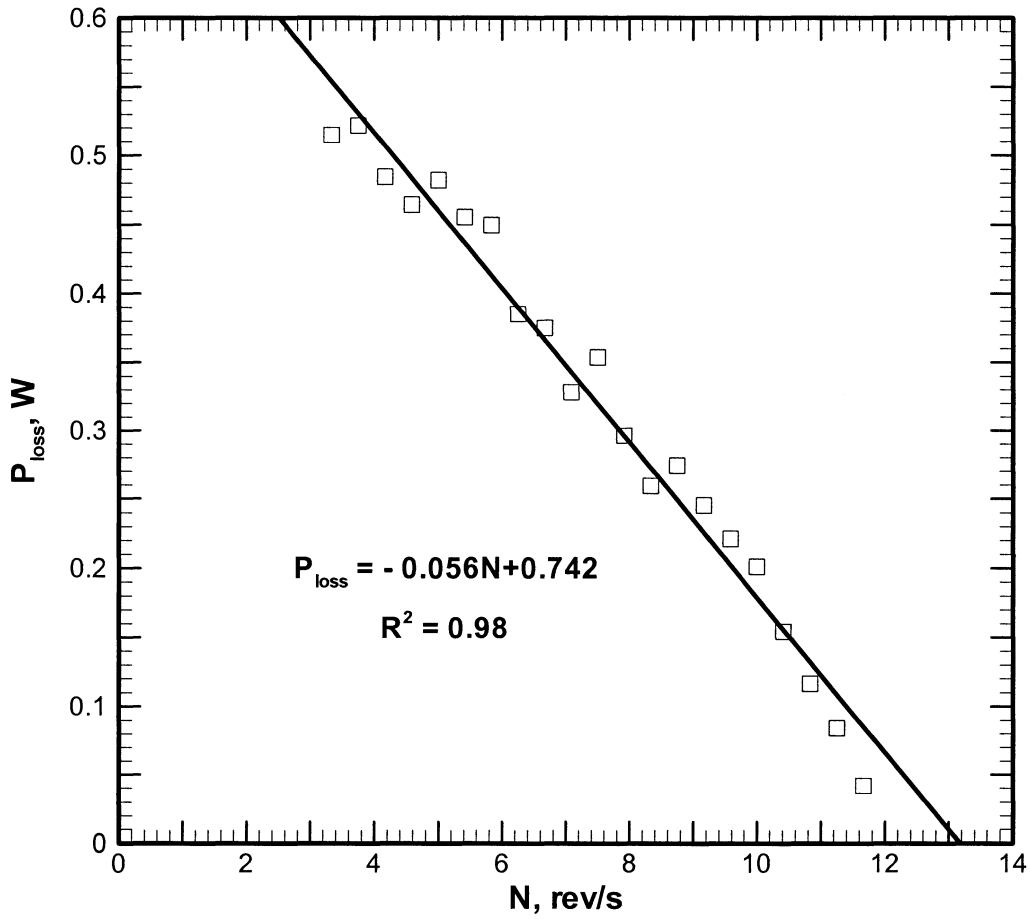


**Figure 3.2:** Mechanical power losses for the DC motor used in this study.

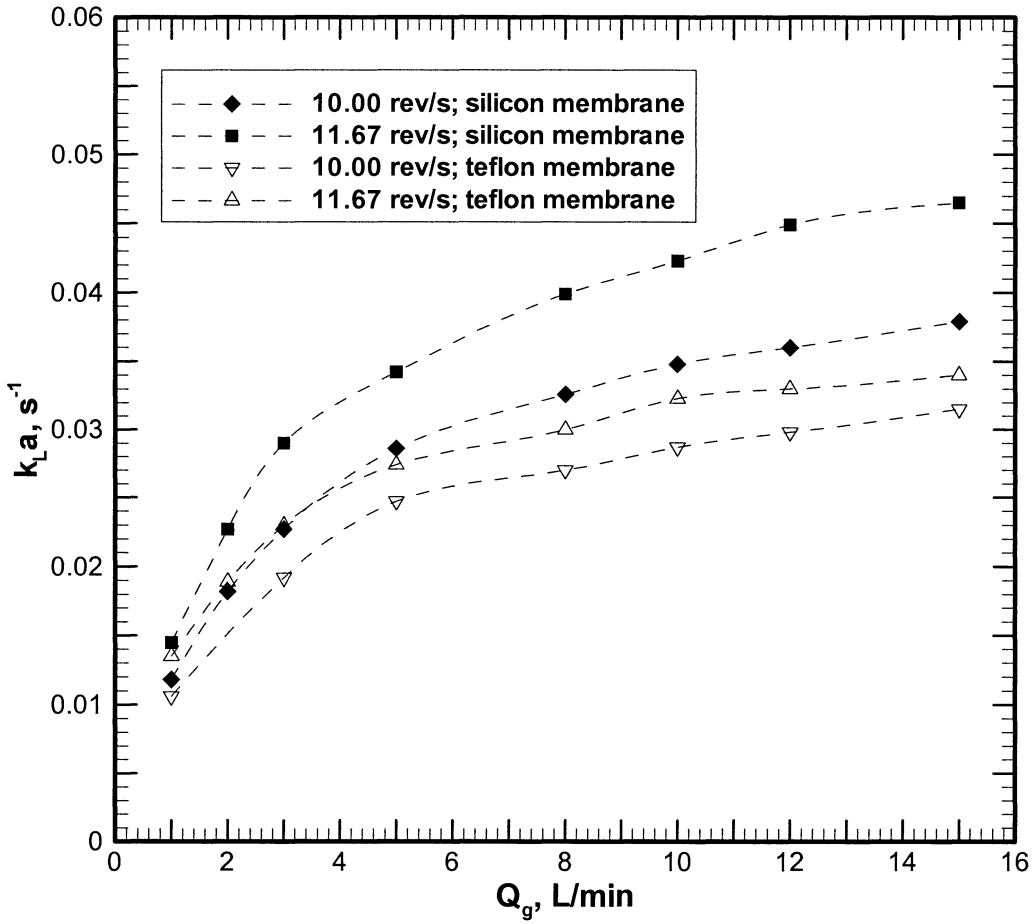


**Figure 3.3:** Comparison of Silicon and Teflon probe tip membranes for measuring  $k_L a$  values of dissolved  $O_2$  in water.

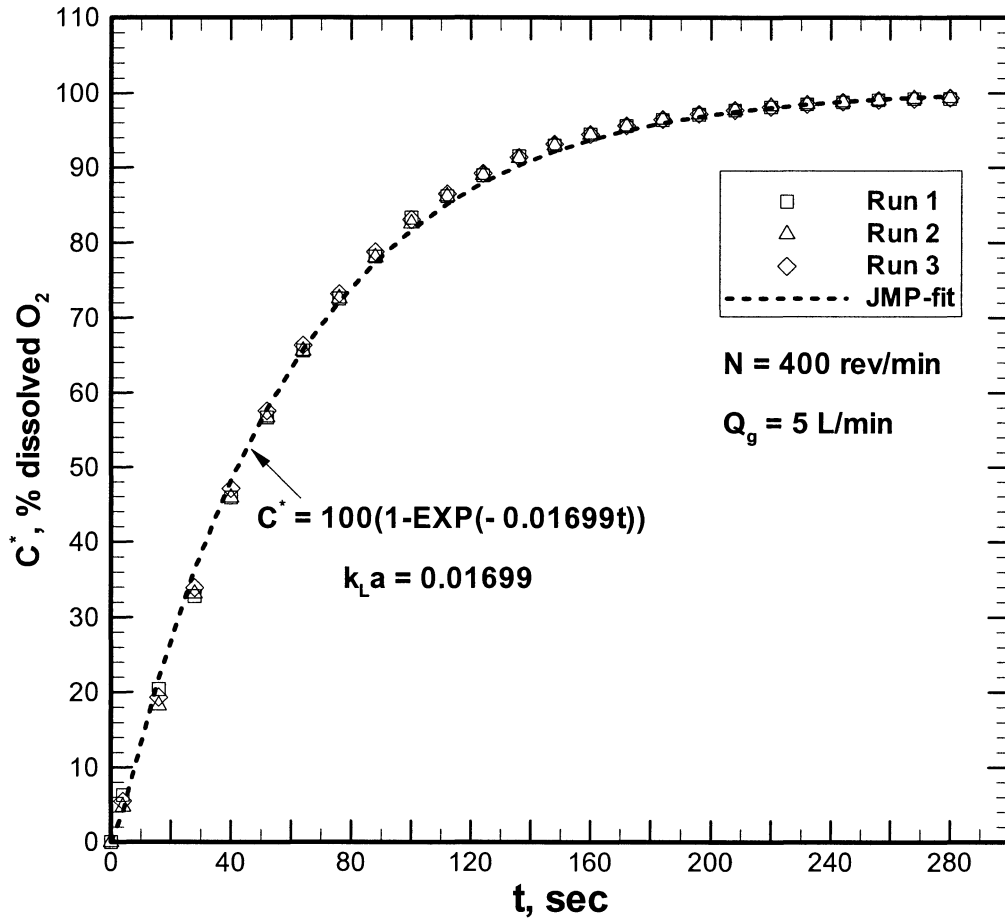


**Figure 3.4:** Normalized dissolved  $O_2$  concentration as a function of time at  $N = 400$  rev/min, and  $Q_g = 5$  L/min of air.

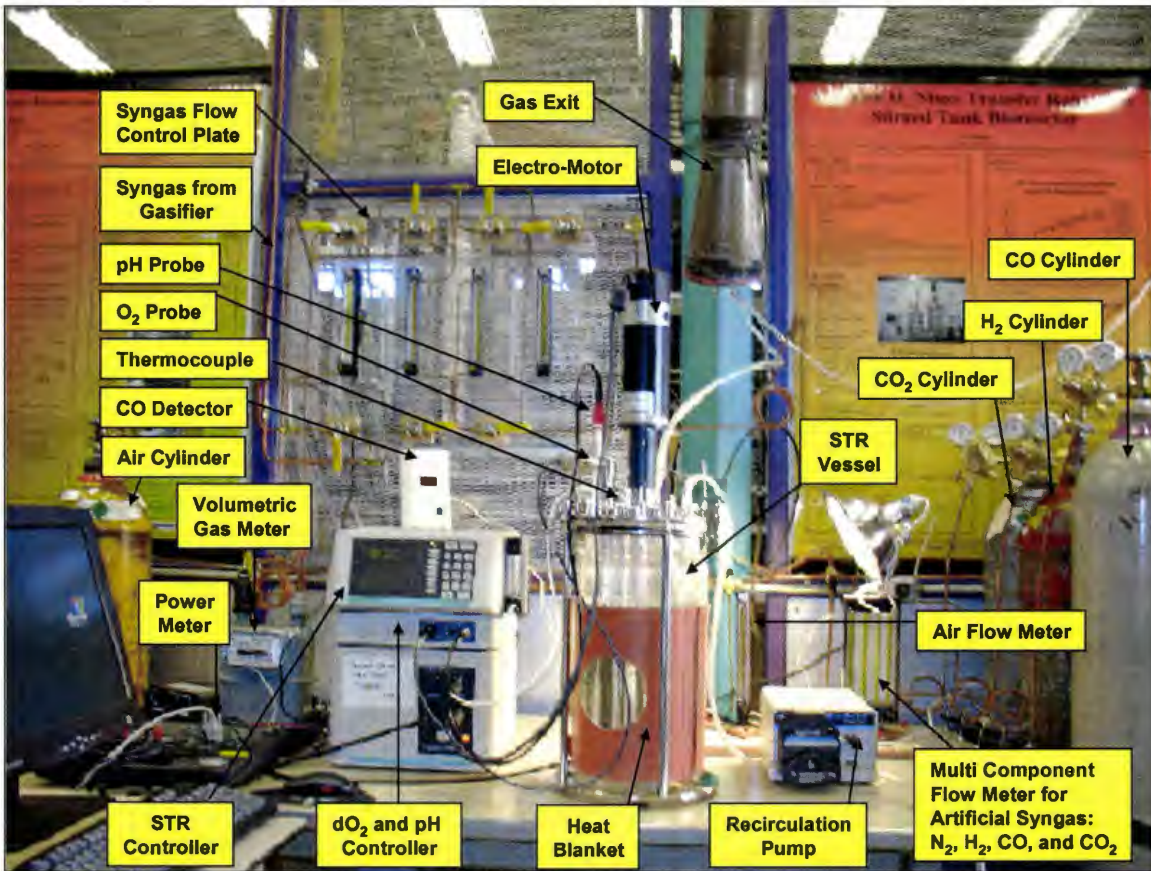
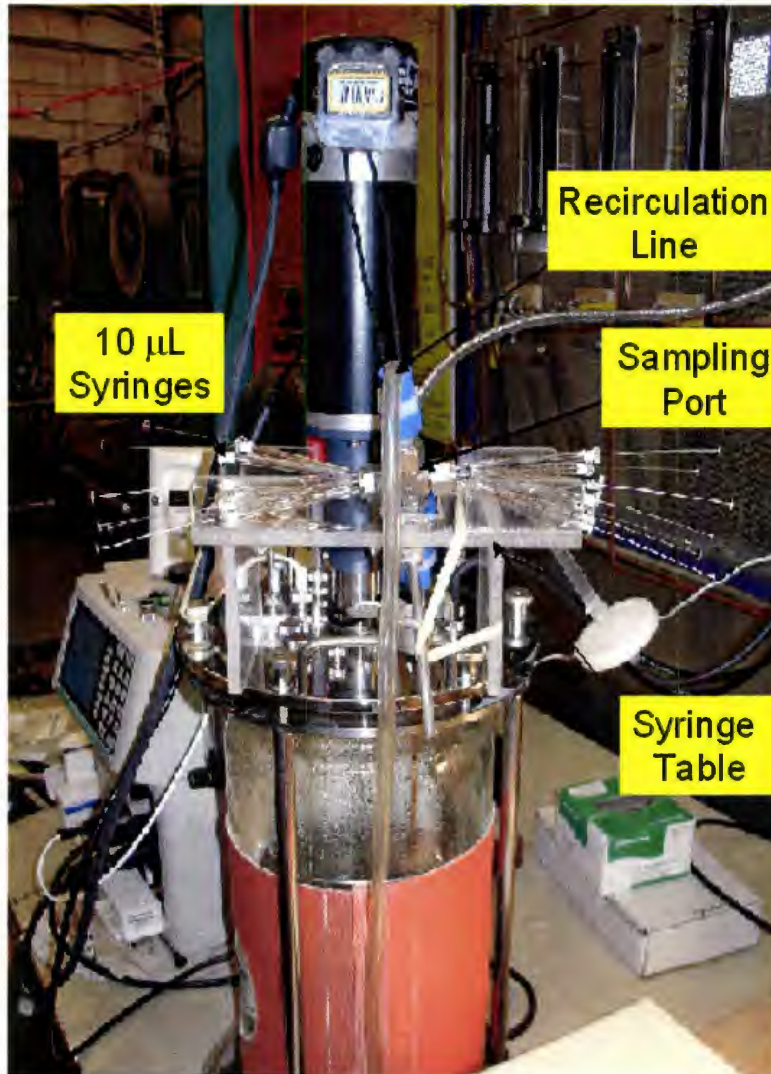
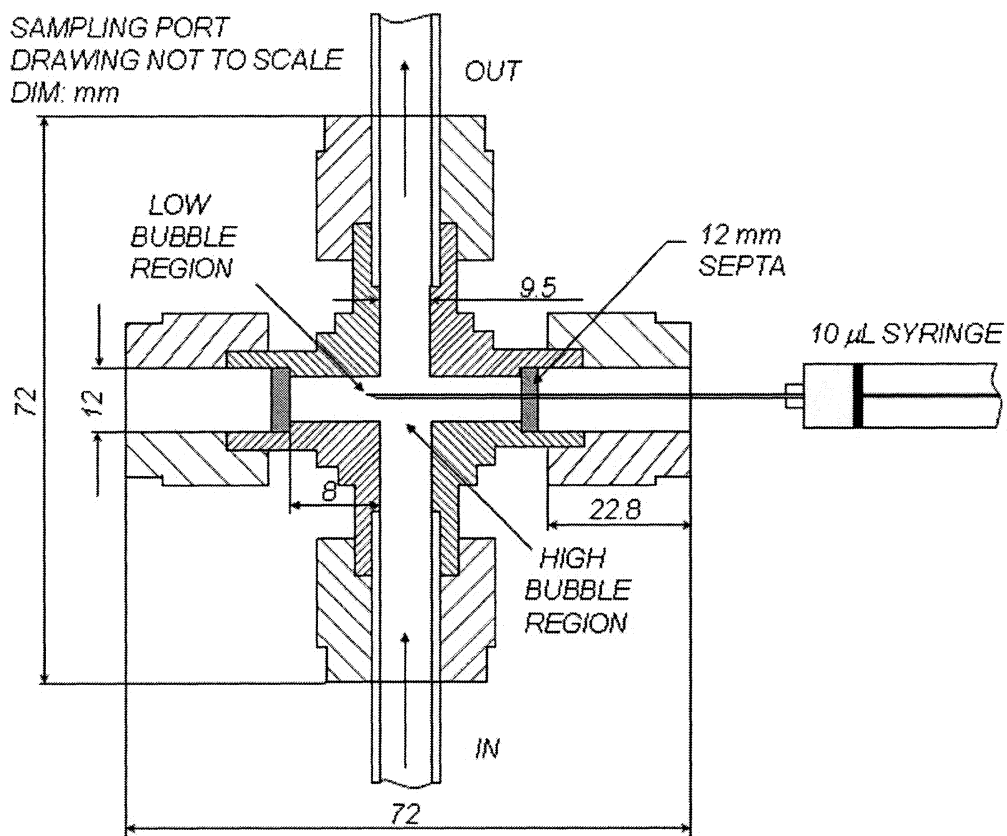


Figure 3.5: STR experimental facility.



**Figure 3.6:** Recirculation line for carbon monoxide sample withdrawal.



**Figure 3.7:** Cross section of the sampling port with 10 µL syringe positioned in the low bubble region.

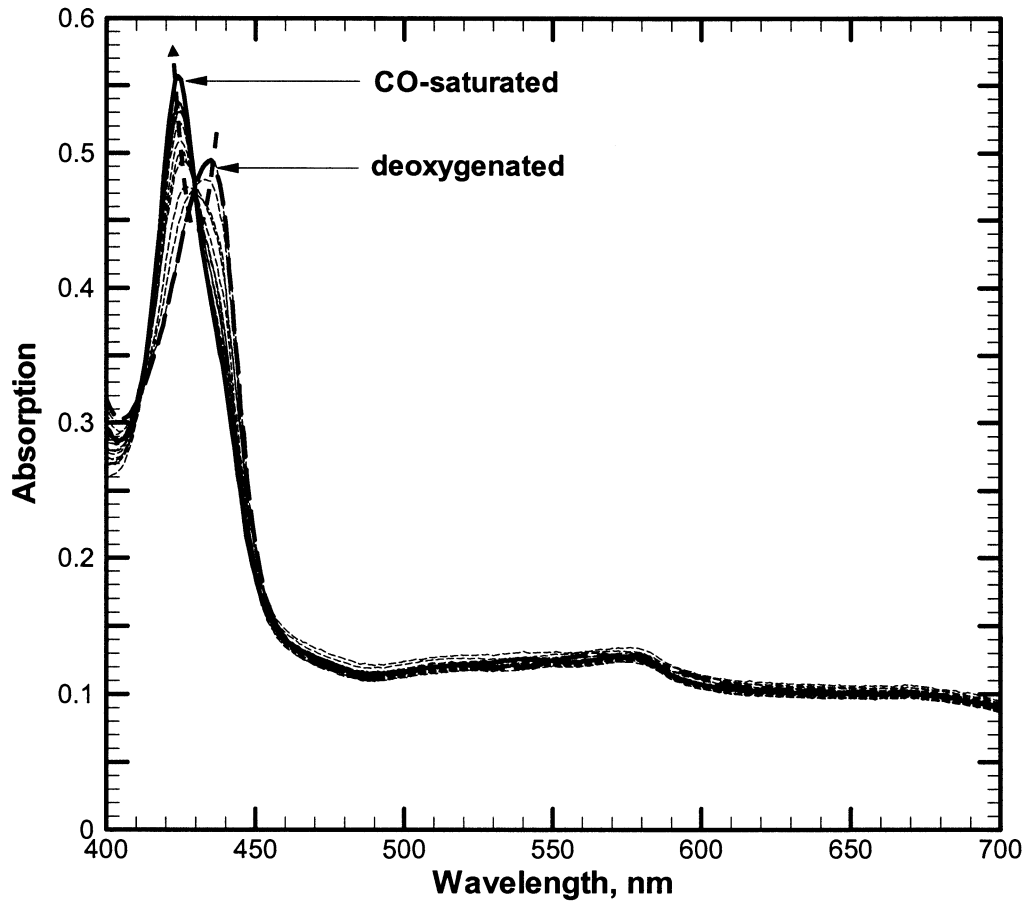


**Figure 3.8:** Typical path followed by collected samples between CO-saturated and deoxygenated peaks to be interpolated by the Spectra Solve.

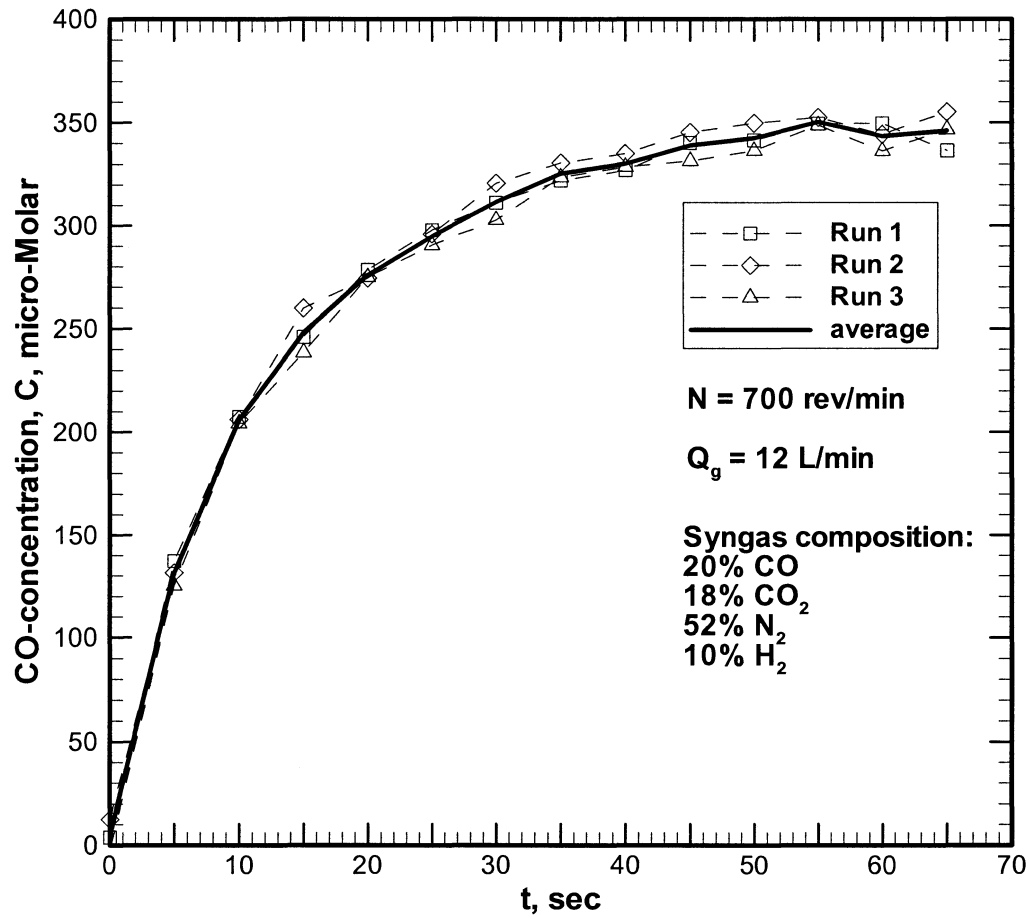


**Figure 3.9:** Dissolved CO-concentration as a function of time at  $N = 700$  rev/min and  $Q_g = 12$  L/min of syngas.

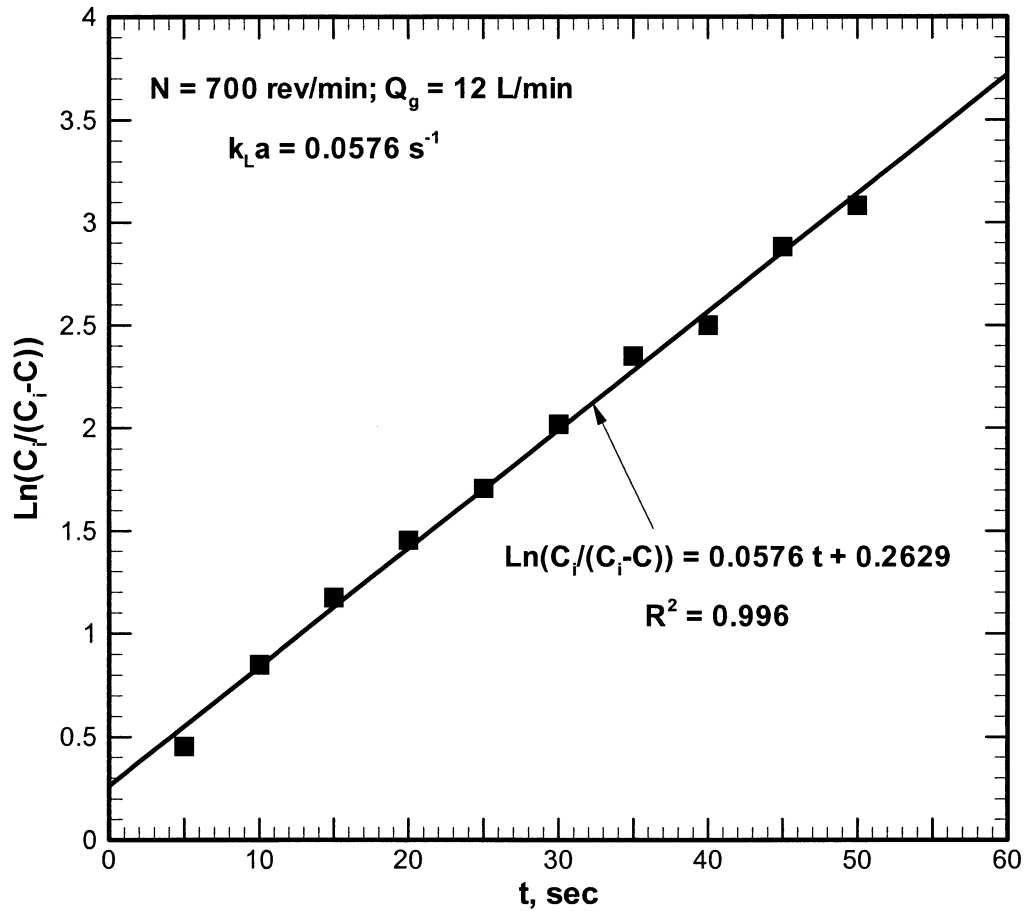


**Figure 3.10:** Determination of volumetric mass transfer coefficient ( $k_L a$ ) for CO in a STR ( $T = 0.211 \text{ m}$ ,  $D/T = 0.35$ ) at  $N = 200 \text{ rev/min}$  and  $Q_g = 12 \text{ L/min}$  of artificial syngas.

## CHAPTER 4: RESULTS AND DISCUSSION

Chapter 4 is subdivided into five main sections. Section one will introduce a STR power correlation. Section two will discuss the dissolved oxygen measurements and the scale-up model for gas-liquid mass transfer in a STR. The third section will compare pure O<sub>2</sub> and air measurements and the proposed model importance. The fourth section will present a model for syngas-liquid mass transfer measurements to predict the carbon monoxide mass transfer rates from those of air, and compare them to those of air. Finally, the last section will briefly discuss gas-liquid mass transfer scale-up issues.

### 4.1 Power Correlation for Gas-Liquid Dispersions in a STR

This section will present mechanical power measurements for an air-water dispersion system in a  $T = 0.211$  m STR. A correlation for gassed power will be proposed in the form suggested by Michael and Miller (1962). Various flow regimes and the gas-liquid hydrodynamics will be emphasized throughout the gassed power analysis.

Power measurements were studied in the  $T = 0.211$  m filled with tap water to a height  $H = T$  while air was dispersed in the vessel. Air flow rates ranged  $1 \leq Q_g \leq 15$  L/min and the impeller speed varied  $3.33 \leq N \leq 13.33$  rev/s (200 to 800 rev/min). An impeller clearance of  $c = T/4$  is used as recommended by Neinow et al. (1977), since it allows dispersion into the lower vessel region at a reasonably low power input while maintaining a satisfactory level of agitation in the upper vessel region. All measurements were made with air supplied from a

ring sparger mounted below the impeller at  $c/3$  from the vessel base.

Figure 4.1 shows one common way of looking at the mechanical power measurements for aerated and unaerated liquids,  $P_g$  and  $P_o$ , respectively, with varying impeller speed at constant gas flow rate. If the gas flow rate is held constant, the gassed power increases with impeller speed, and is generally lower with increasing air flow rate.

When the gassed power number  $N_{pg}$  is plotted against the flow number  $Fl_g$  at constant gas flow rate a family of curves is obtained as shown in Fig. 4.2. While maintaining a constant gas flow rate, the impeller speed was varied to cover the range of bulk flow phenomena as indicated in Fig. 2.4. Flooding occurs at low impeller speeds, and this phenomenon is accompanied by a high gas flow number since the flow number is inversely proportional to the impeller speed (i.e., Eq. (2.5)). Impeller speeds at which flooding occurs ( $N_F$ ) correspond to the local maximum in the gassed power number  $N_{pg}$  and are confirmed by visual observations. The local minimum in the family of curves in Fig. 4.2 corresponds to the transition between loaded and completely dispersed bulk flow regimes, and is defined as the impeller speed at which complete dispersion occurs  $N_{CD}$ , as shown in Fig. 2.4 as the transition from (b) to (c) bulk flow patterns.  $N_{CD}$  is the most desirable operating impeller speed at the particular gas flow rate since it requires the lowest power input to completely disperse the gas throughout the vessel above and below the impeller. The local maximum, marked by  $N_R$  in Fig. 4.2, represents the impeller speed at which gross gas recirculation occurs.

The bulk flow transitions identified in Fig. 4.2 (i.e.,  $N_F$ ,  $N_{CD}$ ,  $N_R$ ) are not recorded for all gas flow rates considered in this study for several reasons. Firstly, high impeller speeds require high power consumption rates. Secondly, if scale-up is to be carried out from a

bench-top to an industrial-scale, there will be an expected limit in allowed power usage for the large vessel sizes (i.e.,  $T = 2$  m and larger) in which they operate to achieve gross gas recirculation regime. Thirdly, if scale-up is to be performed for an industrial-scale vessel, then a bench-top vessel should be studied in the same hydrodynamic ranges as expected in industry to achieve kinetic and hydrodynamic similarity while geometric similarity is held constant.

Another common way of representing gassed power  $P_g$  is by taking data at constant impeller speed while varying the gas flow rate. Figure 4.3 shows the effect of gas flow rate on power consumption. Figure 4.3 shows the power fall at a constant impeller speed as the aeration rate increases because of the growing cavity size on the back of the impeller blade.

If the gassed to ungassed power demand ( $P_g/P_o$ ) is plotted against the flow number  $Fl_g$  (Fig. 4.4) a family of curves can be approximated by a single power curve which passes through different cavity formation regimes (i.e., Fig. 2.8). Gassed power decreases at a constant impeller speed as the aeration rate increases because of the growing cavity size on the trailing face of the impeller. The minimum value of  $P_g/P_o$  for the ranges in this study (0.38) is in the range of  $0.3 \leq P_g/P_o \leq 0.5$ , as expected for a Rushton turbine (Chapman et al., 1983).

With increasing gas flow rate ( $Q_g$ ) at constant operating speed  $N$  the curves start to peel away from the power curve as they transition from loaded to flooded regions. Eventually the impeller becomes fully flooded. When operating in the flooded region a large amount of gas is wasted and the time for gas-liquid mass transport is short, which leads to an unsatisfactory impeller operation in the gas-liquid dispersion. Prior to flooding, the following sequence of stable cavity formation has been reported on the impeller trailing face while  $Q_g$  increases

(Warmoeskerken and Smith, 1982): six vortex cavities, six clinging cavities, combination of three clinging plus three large cavities between the alternating blades known as 3-3 structure, growing 3-3 structure, six large cavities of two different sizes, and flooding ragged cavities. The inflection point identified in Fig. 4.4 corresponds to the transition from six clinging to 3-3 structure when three large cavities are being formed (Warmoeskerken and Smith, 1982).

Figure 4.5 shows gassed power requirements for a gas-liquid system in a  $T = 0.211$  m STR with  $D/T = 0.35$ . The method used to obtain the gassed power draw correlation is based on the empirical approach by Michael and Miller (1962) to yield:

$$P_g = 1.16 \left( \frac{P_o^2 N D^3}{Q_g^{0.56}} \right)^{0.39} \quad (4.1)$$

Equation 4.1 correlates 205 data points within a standard deviation of  $\pm 15\%$  and  $R^2 = 0.97$ , and is in good agreement with other correlations such as those of Pharamond et al. (1975), and Michael and Miller (1962), as shown in Fig. 4.5.

The ungassed power number from Eq. (2.2) as a function of Reynolds number is shown in Fig. 4.6. Generally, the ungassed power number is not constant and it varies with Reynolds number. However, this change is minimal in a turbulent STR ( $Re \geq 2 \times 10^4$ ) and an average ungassed power number ( $\bar{N}_{po}$ ) can be obtained for a particular vessel geometry according to Bujalski et al. (1987). A single correlation proposed by Bujalski et al. (1987) for a wide range of Rushton disc turbines in fully baffled vessels from  $T = 0.22$  to 1.83 m has been used to predict average power numbers to within  $\pm 3\%$  in the form:

$$\bar{N}_{po} = 2.5 \left( \frac{x_1}{D} \right)^{-0.2} \left( \frac{T}{T_o} \right)^{0.065} \quad \text{Eq. (4.2)}$$

where  $x_1$  is the disc thickness and  $T_o = 1$  m is a reference vessel size. The average ungassed power number determined experimentally from power measurements in the range of  $Re \geq 2 \times 10^4$  for  $T = 0.211$  m vessel used in this study is  $\bar{N}_{po} = 4.8$  (Fig. 4.6); Eq. (4.2) provides an average power number of  $\bar{N}_{po} = 5.1$ . The average power number is in the good agreement with the correlation proposed by Bujalski et al. (1987) with the difference of 6% assumed to be most likely due to different experimental setups (i.e., the sparger location below the impeller) and the correlation error.

## 4.2 Dissolved Oxygen Probe Measurements in a STR

This major section is divided into four subsections. In the first subsection, a STR scale-up correlation will be developed. The second subsection will introduce means for choosing STR operational conditions to yield similar hydrodynamics and the associated flow regimes. The third subsection will discuss available  $k_L a$  values from literature used to obtain a general scale-up correlation, which is presented in the last subsection.

### 4.2.1 Scale-Up Correlation Model

In the literature, correlations in the form of Eq. (2.6) have been reported by various researchers to be unsuccessful in STR scale-up analysis or are correlated with the change in exponents (Lines, 2000; Stenberg and Andersson, 1988; Rushton and Bimbinet, 1968; Nienow and Wisdom, 1978). The exponents of Eq. (2.6) vary considerably, depending on

the geometry of the system, the range of variables studied, and the experimental method used in mass transfer measurements. In this work, the dynamic method utilizing a fast response DO probe will be considered, which is also one of the most popular methods in resolving volumetric mass transfer measurements. Hence, it is hypothesized that if the range of variables studied and the geometry of the system could be accounted for in mass transfer measurements, it may be possible to perform a STR scale-up analysis. It has been previously mentioned that for successful STR operation, the tank should operate at the impeller speed at which complete dispersion occurs ( $N_{CD}$ ). Therefore the STR scale-up should be performed around the impeller speed at complete dispersion. Since reliable correlations for impeller speeds at flooding, complete dispersion, recirculation, and after and before large cavity formation exist for a wide range of STR sizes and operating with standard 6 blade Rushton (6DT) impellers, the impeller speeds at which such phenomena exist can be calculated from Eqs. (2.7), (2.8), (2.9), and (2.10), respectively.

The model used for the volumetric gas-liquid scale-up is obtained from the best fit of physically important parameters in STR operation using JMP 5.1 statistical package (SAS Institute, Inc.). The scale-up model yields the following form:

$$\frac{k_L a}{U_g^z} = K \left( \frac{N}{N_{CD}} \right)^x \left( \frac{T}{D} \right)^y \quad (4.3)$$

where  $K$  is an empirically determined constant,  $N$  is the tank operating impeller speed,  $N_{CD}$  is the impeller speed for complete dispersion (Eq. (2.8)), and  $x$ ,  $y$ , and  $z$  are empirically determined exponents. The scale-up model in Eq. (4.3) is a function of the  $T/D$  ratio in a similar way as Eqs. (2.7), (2.8), (2.9), and (2.10) show a  $T/D$  dependence. Although the

geometry is maintained constant (i.e., the STR equipment is standardized to  $D$  with  $H = T$ ), the  $T/D$  dependence becomes necessary since it was varied by different researchers. The superficial gas velocity ( $U_g$ ) is an important variable in gas-liquid mass transport since it provides the actual amount of dispersed gas to the vessel. The dispersion parameter  $N/N_{CD}$  accounts for the gas-liquid hydrodynamics of the various bulk flow regimes (i.e., flooding, loading, complete dispersion, recirculation, and ALC-BLC transition) at operating impeller speed ( $N$ ) normalized to the impeller speed for complete dispersion ( $N_{CD}$ ). The dispersion parameter  $N/N_{CD}$  can be thought of as the degree of the dispersion at the impeller speed  $N$  relative to the degree of complete dispersion at the impeller speed  $N_{CD}$ . It is the amount of gas dispersed at impeller speed  $N$  relative to the amount of gas needed for the complete dispersion at impeller speed  $N_{CD}$  in the vessel. It should be noted that the proposed scale-up model (Eq. (4.3)) requires means of knowing the range of STR operational conditions (i.e.,  $N$  and  $Q_g$  or  $U_g$ ) at which the same or similar hydrodynamics can be achieved for gas-liquid dispersion in a STR. A method for determining similar STR hydrodynamics will be discussed next.

#### **4.2.2 Normalized Hydrodynamic Flow Regime Maps**

Data obtained using bench-top equipment cannot be applied to industrial-scale vessels without a detailed understanding of the local impeller hydrodynamics and gas filled cavities, and their role in determining the bulk flow phenomena. Smith and Warmoeskerken (1985) determined that at very high gas flow rates, the stable 3-3 structure will break down to six ragged vibrating cavities, which confirmed that the transition to flooding occurred at the same time the change in cavity formation was observed. Subsequently, they produced a

single diagram known as “regime map” with transitions from different flow regimes identified for a given vessel (e.g., Fig. 2.9).

From an industrial point of view, it is very important to identify the transitions between the various flow regimes since different power consumption occurs in different flow regimes (e.g., Figs. 2.3, 2.7, 2.8). The best STR performance for the most efficient operation is at  $N = N_{CD}$ , where the minimum power is utilized for complete gas dispersion (see Fig. 2.3). If the flow regime map is normalized with respect to the minimum impeller speed at complete gas dispersion ( $N_{CD}$ ), and plotted as a function of gas flow rate ( $Q_g$ ), a flow regime map can be produced for a given STR as shown in Fig. 4.7. Such flow regime maps are useful in understanding the STR operational ranges for successful scale-up analysis.

The “before large cavity-after large cavity” (BLC-ALC) line in Fig. 4.7 corresponds to the transition from the vortex-clinging cavities to the first large cavity and is given by Eq. (2.10). The gassed power consumption is approaching its minimum value in the concave portion of Fig. 2.8, which corresponds to the initiation of large cavity formation and growth. From an economical perspective, this value is of primary interest because it provides the minimum power consumption for complete gas dispersion; that is, it is the best operating condition for an industrial-scale STR used in fermentation processes.

It can be expected that for successful scale-up, the flow regimes should be similar, and in order to understand the physics of gas-liquid contacting, some operating condition limits are required. Therefore, it is desirable both economically and physically to perform the scale-up for minimum power consumption and similar hydrodynamics. Hydrodynamic similarity and low power consumption will be satisfied in the regions identified in Fig. 4.7 as ALC (after large cavity), completely dispersed, and loaded. Such regions are physically realistic in

industrial-size vessels and are identified as the shaded region of Fig. 4.7. Generally, when the STR is operated in the after large cavity regime (ALC) at the impeller speed ( $N$ ) normalized to the impeller speed at complete gas dispersion ( $N_{CD}$ ), it would represent the amount of dispersed gas in the liquid needed to achieve low power consumption (see Fig. 2.8). Similarly, the flooding-loading transition, complete dispersion, and recirculation line are normalized to the impeller speed at complete dispersion ( $N_{CD}$ ) and calculated from the empirical correlations found in Eqs. (2.7), (2.8), and (2.9), respectively. Data available in the literature that falls within the shaded region in Fig. 4.7 have been used in the proposed scale-up correlation. These data are described next.

#### 4.2.3 Available $k_L a$ Data in the Literature

Literature data summarized in Table 4.1, and found in the shaded region of Fig. 4.7 are used in the correlation development in the form of Eq. (4.3). Table 4.1 also provides the data range of the current study only for comparison, and has not been used in the correlation development.

A reliable power input correlation is needed for some literature data since some investigators did not specify actual input power or impeller speed. Extensive data for input power in STR gas-liquid dispersions by a six-bladed disc turbine over a vessel size range of 0.21 to 3.33 m, and for superficial gas velocities  $U_g \leq 0.053$  m/s were correlated by Hughmark (1980) and presented in the form:

$$\frac{P_g}{P_o} = 0.1 \left( \frac{Q_g}{N V} \right)^{-1/4} \left( \frac{N^2 D^4}{g D_i V^{2/3}} \right)^{-1/5} \quad (4.4)$$

Equation (4.4) is based on 391 data points with a standard deviation between calculated and experimental values of  $\pm 11.7\%$ . This correlation is used with the literature data described below to determine either  $P_g$  or  $N$  when only one value is given.

**Table 4.1:** Literature data used in the general scale-up correlation development (Eq. (4.6)).

| Reference                              | T, m     | D, m       | D/T            | $U_g \times 10^2$ , m/s | N, rev/s   | N/N <sub>CD</sub> | $P_g/V$ , W/m <sup>3</sup> | Impeller       |
|--|----------|------------|----------------|-------------------------|------------|-------------------|----------------------------|----------------|
| Smith et al. (1977)                    | 0.61     | 0.2, 0.31  | 0.33, 0.5      | 0.44-1.66               | 1.67-5.2   | 0.28-2.44         | 50-5000                    | 6DT            |
|  | 1.83     | 0.67, 0.91 | 0.37, 0.5      | 0.9-4.6                 | 0.917-1.8  | 0.25-1.26         | 80-1500                    | 6DT            |
| Linek et al. (1987)                    | 0.29     | 0.1        | 0.34           | 0.212-0.424             | 7.5-14.17  | 1.4-3.8           | 500-5000                   | 6DT            |
| Chandrasekharan and Chalderbank (1981) | 1.22     | 0.4        | 0.33           | 0.35-1.8                | 1.75-4.37  | 0.85-1.56         | 94-1160                    | 6DT            |
| Figueiredo and Chalderbank (1979)      | 0.91     | 0.27       | 0.3            | 0.634-1.27              | 4.17-8.33  | 0.86-2.42         | 410-4800                   | 6DT            |
| Yawalkar et al. (2002b)                | 0.44-2.7 | 0.17-1.35  | 0.33, 0.4, 0.5 | 0.212-2.5               | 0.54-11.98 | 0.51-1.77         | 92-3507                    | 6DT, A315, PBT |
| van't Riet (1979)                      | 0.5      | 0.17       | 0.33           | 0.5-3.6                 | 5.4-13.2   | 0.67-2.65         | 500-7000                   | 6DT            |
| Pollard (1978)                         | 1.81     | 0.6        | 0.33           | 0.85-1.24               | 1.34-2.51  | 0.71-1.22         | 130-900                    | 6DT            |
| Fuchs et al. (1971)                    | 0.6      | 0.25       | 0.43           | 0.83-1.67               | 2.25-4.32  | 0.85-1.64         | 350-10000                  | 6DT            |
| Hickman (1988)                         | 0.6      | 0.2        | 0.33           | 0.2-1.7                 | 2-7.1      | 0.72-1.61         | 100-2000                   | 6DT            |
|  | 2        | 0.66       | 0.33           | 0.37-1.7                | 1.67       | 0.66-1.42         | 1600                       | 6DT            |
| Martin et al. (1994)                   | 0.56     | 0.19       | 0.33           | 0.93-1.91               | 3.25-8.26  | 0.68-1.73         | 170-2400                   | 6DT            |
| Current Study                          | 0.211    | 0.0747     | 0.35           | 0.238-0.715             | 6.67-13.33 | 0.87-3.0          | 260-2660                   | 6DT            |

Van't Riet (1979) studied mass transfer rates using the dynamic gassing-out method in a  $T = 0.5$  m diameter vessel. Good agreement was shown in his study with the sparged air data from Calderbank (1958), Robinson and Wilke (1973), Smith et al. (1977), and Valentin and Preen (1962) for vessel volumes of 2.5 to 4400 liters using pure water. Data were graphically represented at low, intermediate, and large superficial gas velocities in the form of Eq. (2.6), correlating data from his study with literature data to within approximately 20-40%. Van't Riet (1979) concluded that a mass transfer correlation is possible in the form of Eq. (2.6) if  $\alpha$  (0.35-0.5) and  $\beta$  (0.3-0.6) were varied. This correlation form, using power per

unit volume and superficial gas velocity, was not useful in obtaining a single correlation for different vessel sizes in van't Riet's study and the compared literature data. However, using a model in the form of Eq. (4.3), van't Riet's data are successfully correlated for the range of variables studied in his work and are represented in Fig. 4.8.

Pollard (1978) carried out tests in a large mixing vessel ( $T = 1.8$  m) equipped with a standard Rushton turbine. Mass transfer measurements were monitored using a dissolved oxygen probe having a response time of about 3 seconds. His results were given in tables for the widest possible range of operational conditions from which data that fall in the after large cavity formation (ALC) region are correlated in Fig. 4.8. A large amount of Pollard's data were taken in the before large cavity formation (BLC) region. Additionally, some data were collected at vary high gas flow rates for which the power consumption was limited due to the large vessel size. This resulted in operating conditions near the flooding condition and those data are not included in Fig. 4.8. Since the temperatures at which the mass transfer data were measured were also provided in the tables, it was possible to convert all the  $k_L a$  values to a standard temperature of  $20^\circ\text{C}$  according to Smith et al. (1977):

$$\frac{k_L a \mu}{(\theta + 273)} = \text{constant} \quad (4.5)$$

Fuchs et al. (1971) studied the effects of surface aeration on scale-up procedures for fermentation processes in STRs of various sizes ( $T = 0.13$  to  $3.33$  m). They determined that surface aeration is more intensified in large vessels. Their data were represented graphically for each vessel size in the form of Eq. (2.6). Only their data for  $T = 0.6$  m are used in Fig 4.8 because these data were taken in the after large cavity formation region. Their data from smaller diameter STRs were obtained at too high impeller speeds to yield unrealistic power

demands when scaled up to an industrial STR. Large diameter STRs were operated at too low impeller speeds due to excessive power requirements and did not completely disperse the gas throughout the vessel. These conditions resulted in a large inconsistency in the STR hydrodynamics and gas-liquid flow regimes, and hence, they are not used in Fig. 4.8.

Hickman (1988) conducted steady state hydrogen-peroxide experiments to determine oxygen mass transfer measurements in vessel diameters  $T = 0.6$  and  $2$  m using a six-blade Rushton turbine. The mass transfer results were graphically represented for each vessel size in the form of Eq. (2.6) with exponents  $\alpha$  (0.40-0.54) and  $\beta$  (0.57-0.68), and a combined correlation was proposed with additional scatter (Hickman, 1988). Their results from both vessels in which after large cavity formation was determined are used in Fig. 4.8.

Martin et al. (1994) studied the performance of a Rushton turbine and a Prochem Maxflo T turbine with modifying coalescence behavior using either electrolyte or surfactant solutions. They concluded that  $k_L a$  values were much lower in the surfactant solution than in the electrolyte solution and that  $k_L a$  values were dependant on  $P_g/V$  and  $Q_g$ , but were independent of agitator type. Martin's data were graphically available for a  $0.33T$  Rushton turbine in the  $T = 0.56$  m vessel and are well correlated in Fig. 4.8.

#### **4.2.4 General Scale-Up Correlation for Dissolved Oxygen in Water**

Figure 4.8 shows a general scale-up oxygen mass transfer correlation using data from the literature for a wide range of vessel diameters ( $T = 0.21$  to  $2.7$  m) in the form of the proposed model in Eq. (4.3):

$$\frac{k_L a}{U_g^{0.93}} = 1.59 \left( \frac{N}{N_{CD}} \right)^{1.342} \left( \frac{T}{D} \right)^{0.415} \quad (4.6)$$

Equation (4.6) is based on a total of 282 data points and has an  $R^2$  value of 0.97 with the majority of the data correlated within  $\pm 20\%$ . It should be noted that Eq. (4.6) is largely dependent on the dispersion parameter ( $N/N_{CD}$ ), and less dependent on the reactor to impeller size ratio.

To graphically view the significance of the model or focus attention on whether an effect is significant, it is desirable to display the data from the point of view of the hypothesis for that effect such as an X-ray picture showing the inside of the data rather than a surface view from the outside. The leverage plot is this kind of view of the correlating data, a view calculated to give a maximum insight into how the fit carries the data.

The graphical display of an effect's significance test is called a "leverage plot" (JMP 5.1, SAS Institute, Inc.). This kind of plot shows for each point what the residual would be both with and without that effect in the model. The effect in a model is tested for significance by comparing the sum of squared residuals to the sum of squared residuals of the model with that effect removed. Residual errors that are much smaller when the effect is included in the model confirm that the effect is a significant contribution to the fit. An example of the leverage plot definition is shown in Fig. (4.9) adopted from the JMP 5.1 statistical package (SAS Institute, Inc.). The distance from a point to the line of fit shows the actual residual. The distance from the point to the horizontal line of the mean shows what the residual error would be without the effect in the model. In other words, the mean line in this leverage plot represents the model where the hypothesized value of the parameter (effect) is constrained to zero. The term "leverage" is used because a point exerts more influence on the fit if it is

farther away from the middle of the plot in the horizontal direction. At the extremes, the differences of the residuals before and after being constrained by the hypothesis are greater and contribute a larger part of the sums of squares for that effect's hypothesis test.

Figure 9b shows the leverage plot with confidence curves. The confidence lines indicate whether the test is significant at the 5% level by showing a confidence region for the line of fit. If the confidence region between the curves contains the horizontal line, then the effect is not significant. If the confidence curves cross the horizontal line, the effect is significant.

The leverage plots with confidence curves for  $N/N_{CD}$ ,  $U_g$ , and  $T/D$  are shown in Figs. 4.10a-c, where the slopes for the lines of fit correspond to the x, y, and z exponents in Eq. (4.6). The largest contribution is by the dispersion parameter  $N/N_{CD}$ , and the superficial gas velocity  $U_g$  as shown in Figs. 4.10a and 4.10b. Although  $T/D$  least contributes to the fit (Fig. 4.10c), the  $T/D$  dependence is still important and it will be assumed constant for gas-liquid studies in STRs since it is only a function of geometry. However, independence of Eq. (4.6) on  $T/D$  ratio is also feasible if the data were correlated at a constant  $T/D$  ratio employing an even larger dependence on the relative dispersion parameter ( $N/N_{CD}$ ) and somewhat more scatter.

The high dependence of the mass transfer rate on  $N/N_{CD}$  can be explained by the nature of the impeller speed for complete dispersion ( $N_{CD}$ ). Rearranging Eq. (2.8) to read:

$$N_{CD} = 4 \frac{Q_g^{0.5} T^{0.25}}{D^2} \quad (4.7)$$

From Eq. (2.8), impeller speed at complete dispersion is a weak function of Froude number,  $Fr = N^2 D/g$  (i.e., the ratio of the inertial to gravitational forces), compared to the gas flow number ( $Fl_g = Q_g/ND^3$ ) which is a large function of impeller size and gas flow rate.

Therefore, at constant  $D/T$ , the impeller speed at complete gas dispersion from Eq. (4.7) is directly proportional to the square root of gas flow rate ( $N_{CD} \propto Q_g^{0.5}$ ), or the amount of gas at complete dispersion. Similarly, the  $N/N_{CD}$  ratio will be proportional to the ratio of the amount of gas at impeller speed  $N$  relative to the amount of gas at impeller speed  $N_{CD}$ .

After the general scale-up correlation Eq. (4.6) was obtained from available literature data, volumetric mass transfer coefficients were determined in a bench-scale vessel ( $T = 0.211$  m) and found to fit the proposed correlation if the hydrodynamic conditions are satisfied (Fig. 4.8). Figure 4.11 shows that  $k_{La}$  increases in a nonlinear fashion with increasing gas flow rate at constant impeller speed. The error bars in this figure represent  $\pm 1$  standard deviation from a series of multiple runs (typically 3). Figure 4.12 reveals an almost linear  $k_{La}$  increase with increasing impeller speed at constant gas flow rate. Although a wide range of operational conditions are investigated for  $T = 0.211$  m, only the operational conditions shown by the shaded region in the hydrodynamic flow regime map (Fig. 4.7) are correlated by Eq. (4.6); this is in the gas flow rate range of  $5 \leq Q_g \leq 15$  L/min. This region corresponds to the operational conditions after large cavities have been formed (ALC) at gas flow rates from  $Q_g \geq 5$  L/min, up to the recommended upper gas flow rate bound of  $Q_g = 15$  L/min. At higher gas flow rates, large amounts of gas are not effectively utilized unless gas recirculation is employed. Additionally, excessive power requirements are needed to guarantee complete gas dispersion at high gas flow rates. It should be noted that the shaded region in Fig. 4.7 is also bounded by the flooding-loading transition. There is also an overshoot at the recirculation line since a gradual transition actually exists and the map was constructed from correlations obtained by other investigators differing in the recirculation

definition.

### **4.3 Scale-Up and Hydrodynamic Dependence of Gas-Liquid Mass Transfer Correlation for Dissolved O<sub>2</sub> in Water**

This section is subdivided into two parts. The first part will discuss gas-liquid mass transfer mechanisms, and part two will compare the  $k_{L,a}$  values for pure O<sub>2</sub> and air data in the ALC region.

#### **4.3.1 Gas-Liquid Mass Transfer Mechanisms in a STR**

Gas-liquid mass transfer mechanisms as described by Eq. (2.14), are simultaneously due to both diffusion and advection. However, the molecular diffusion process alone is not fast enough for industrial requirements and is so slow that it is usually ignored. For example, if the gas and liquid are placed together in a vessel, and if we wait long enough, the molecules will form a uniform mixture reaching an equilibrium condition as a result of the concentration gradient and random molecular motion. In gas-liquid mixing, steady state mass transfer is reached in much shorter time periods because of the bulk fluid motion induced by the impeller. The resulting flow patterns are the result of the advective flow and the inertial effects of the stirrer. This implies that the various flow regimes are significant because they affect the power demand, the gas-liquid hydrodynamics around the impeller blades, and the ultimate gas-liquid mass transfer.

### 4.3.2 Hydrodynamic Dependence of Dissolved O<sub>2</sub> Correlations

Figure 4.13 shows a single correlation in the form of Eq. (2.6) regressed for the entire range of the operational conditions studied ( $1 \leq Q_g \leq 15$  L/min and  $6.67 \leq N \leq 13.33$  rev/s) in  $T = 0.211$  m vessel:

$$k_L a = 0.045 \left( \frac{P_g}{V} \right)^{0.46} U_g^{0.62} \quad (4.8)$$

Equation (4.8) is based on a total of 40 data points and has an  $R^2$  value of 0.99 with a standard deviation error of  $\pm 6.4\%$ . The  $k_L a$  correlation with power density and superficial gas velocity (Eq. 4.8) is not sensitive to the range of bench-scale operating conditions and is independent of the STR hydrodynamics and the associated flow regimes.

Figure 4.14 shows that when the data of this study from the BLC region are plotted with the data from ALC region using Eq. (4.6), a poor correlation results because STR flow regimes are disregarded. A separate correlation is needed for the data taken at gas flow rates in the range of  $1 < Q_g < 5$  L/min; the region before large cavities are formed (BLC) in Fig. 4.7. However, after large cavity data (ALC) that correspond to the shaded region of Fig. 4.7 fit well the general scale-up correlation obtained from literature data (Eq. (4.6)) as shown in Fig. 4.14.

In our interest of understanding the dispersion behavior of a single gas component into water, dissolved oxygen mass transfer values are measured for pure oxygen dispersed in water at a constant temperature of 25°C. The volumetric gas-liquid mass transfer measurements from pure O<sub>2</sub> are collected for the same operating conditions at which the oxygen measurements were obtained from air. The  $k_L a$  values using pure O<sub>2</sub> as a function of

gas flow rate ( $Q_g$ ) or impeller speed ( $N$ ) are shown in Figs 4.15 and 4.16, respectively. The results are similar to the dissolved oxygen measurements from air. The BLC-data are approximately in the region of  $1 \leq Q_g \leq 5$  L/min while ALC-data correspond to the gas flow rate range of  $5 \leq Q_g \leq 15$ . Comparing  $k_{La}$  values of pure oxygen in Fig. 4.15 to Fig. 4.11 for dissolved oxygen measurements from air, the  $k_{La}$  values are higher for pure oxygen than for air at the same operating conditions. The gas-liquid mass transfer for pure gases is entirely due to a single gas component mass transfer, and for the multi component systems, gas-liquid mass transfer is affected by simultaneously dissolving additional gas components. For a mixture of ideal gases, the gas density and molar gas concentration of individual gas components are related to the partial pressure through the ideal gas law (Incorpera and DeWitt, 2002). Hence, from Dalton's law of partial pressures it follows that:

$$x_k = \frac{C_k}{C} = \frac{p_k}{p} \quad (4.9)$$

where  $x$  is the mole fraction of the amount of any species  $k$  from multi-gas constituents (Incorpera and DeWitt, 2002). The driving potential for the gas-liquid mass transfer is the concentration gradient in Eq. (2.17), which, for a gas mixture is smaller because the local concentration is proportional to the partial gas pressure Eq. (4.9). For a single component gas, the driving potential is higher because the partial pressure is identical to the total gas pressure. Therefore, in the mixture of ideal gases, the mass transfer rates are lower when compared to a single gas component mass transfer.

The correlation for  $k_{La}$  values using pure oxygen in the form of Eq. (2.6) is shown in Fig. 4.17 for the same operating conditions as dissolved  $O_2$  measurements from air:

$$k_L a = 0.062 \left( \frac{P_g}{V} \right)^{0.44} U_g^{0.6} \quad (4.10)$$

This correlation is based on a total of 40 data points and has an  $R^2$  value of 0.97 with a standard deviation error of  $\pm 8.6\%$ . In the  $k_L a$  model (Eq. 2.6), both exponents  $\alpha$  and  $\beta$  for  $k_L a$  values of pure  $O_2$  are about 4% and 3% smaller, respectively, from those of the  $k_L a$  values from air. However, the  $k_L a$  values for pure  $O_2$  are about 30% higher, on average, when compared to  $k_L a$  values from air, which is accounted by the difference in constant  $C_1$ , being 42% higher for pure  $O_2$  measurements than for  $O_2$  in air.

When the gas-liquid scale-up model (Eq. (4.3)) is applied in the analysis of pure  $O_2$  data, the flow regime dependence reveals the same behavior as for the  $O_2$  measurements from air (Fig. 4.14). Figure 4.18 shows a single correlation for the ALC-data from the shaded region of Fig. 4.7 based on total of 25 points with an  $R^2$  of 0.99 and the standard deviation of  $\pm 3.6\%$ :

$$\frac{k_L a}{U_g^{0.81}} = 1.36 \left( \frac{N}{N_{CD}} \right)^{1.048} \left( \frac{T}{D} \right)^{0.415} \quad (4.11)$$

Figure 4.18 shows also that a poor correlation will result when data from the BLC region are used in STR scale-up model from Eq. (4.3).

To compare the scale-up equation for pure  $O_2$  (at  $\theta = 25^\circ\text{C}$ ) to the scale-up correlation for  $O_2$  from air (at  $\theta = 20^\circ\text{C}$ ), Eq. (4.11) is compensated for temperature using Eq. (4.5):

$$\frac{k_L a}{U_g^{0.81}} = 1.2 \left( \frac{N}{N_{CD}} \right)^{1.048} \left( \frac{T}{D} \right)^{0.415} \quad (4.12)$$

The constant  $K$  decreased to 1.2 and is entirely responsible in the temperature change, while the exponents  $x$ ,  $y$ , and  $z$  remained constant. In both models, Eq. (2.6) and Eq. (4.3), the exponents for pure  $O_2$  measurements are smaller when compared to  $O_2$  measurements from air. This can be explained by the driving potential for gas-liquid mass transport being higher for single gas components, demanding smaller gas flow rates and less power input to achieve a similar mass transfer rate. However, the constant  $K$  is about 24% higher for the air data in the scale-up model, while the constant  $C_1$  is 42% smaller for the air data in the correlation form of Eq. (2.6). The difference in  $k_L a$  values between pure  $O_2$  and air measurements in the model form Eq. (2.6) is entirely due to the change in constant  $C_1$  with  $\alpha$  and  $\beta$  exponents showing almost no effect. However, in the scale-up model, this difference is equally due to the change in the  $x$  and  $z$  exponents, emphasizing the importance of  $U_g$  and  $N/N_{CD}$ , and the interplay between mass transfer driving potential and hydrodynamic influence. The scale-up model in Eq. (4.3) is highly flow regime dependant, and can be reliably used in STR scale-up if gas-liquid mass transfer takes place in similar hydrodynamic operating conditions, and with similar gas compositions. In addition, the  $k_L a$  mass transfer model in the form of Eq. (2.6) correlated all the data studied for both  $O_2$  and air and is independent of the STR hydrodynamics and the associated flow regimes in a  $T = 0.211$  m STR.

#### **4.4 Scale-Up Correlation for Dissolved CO in Water from Syngas**

It has been shown that scale-up of STRs requires similar operating conditions that for any reactor size can be chosen by the use of hydrodynamic flow regime maps. Hence, mass transfer scale-up correlations for air and pure  $O_2$  are correlated in the ALC region (Fig. 4.7).

It should be noted that the ALC region is the only region of interest since the power consumption approaches a minimum after large cavities are formed. This section will present a scale-up correlation for syngas-liquid mass transfer in the ALC region, and predict the  $k_La$  values for carbon monoxide from those of air.

A composition of a gas-mixture modeled from CO, CO<sub>2</sub>, N<sub>2</sub> and H<sub>2</sub> (artificial syngas) on the volumetric basis (20, 18, 52, 10%) is used to measure dissolved carbon monoxide concentrations. The operating conditions correspond to those of the ALC region at gas flow rates of  $5 \leq Q_g \leq 15$  L/min of artificial syngas, and impeller speeds of  $6.67 \leq N \leq 11.67$  rad/s. Figure 4.19 shows a scale-up correlation for dissolved carbon monoxide mass transfer at 30°C in tap water in the form of Eq. (4.3):

$$\frac{k_La}{U_g^{1.31}} = 11.67 \left( \frac{N}{N_{CD}} \right)^{1.894} \left( \frac{T}{D} \right)^{0.415} \quad (4.13)$$

Equation (4.13) is based on a total of 25 data points studied in the ALC region and has an R<sup>2</sup> value of 0.98 with a standard deviation of  $\pm 8.0\%$ . The  $k_La$  values at constant impeller speed and at constant gas flow rate are shown in Figs. 4.20 and 4.21, respectively. Figure 4.20 shows approximately a straight line relationship of similar slopes for the  $k_La$  values at constant impeller speed, which is also recognized for air and pure O<sub>2</sub> data in the ALC region. However, at constant gas flow rate (Fig. 4.21), the  $k_La$  values for CO increase exponentially as compared to the approximate linear increase in Figs. 4.12 and 4.16 for air and pure O<sub>2</sub> data, respectively. Hence, Eq. (4.13) shows a higher dependence on  $U_g$  and  $N/N_{CD}$  parameters.

Comparing the CO scale-up (Eq. (4.13)) to that of air Eq (4.6), the x and z exponents are

higher for the CO data at approximately the same gas fractions. This difference in the exponentials is most likely explained by the lower CO solubility in water from that of air such that the saturation limit is reached much faster in the CO system at the same operating conditions. In other words: (i) if the solubility is infinite, it will take a long time to reach a steady state value and therefore produce a slower mass transfer rate, and (ii) if the solubility is very low, a steady state will be reached faster and produce a higher mass transfer rate. Therefore, at the same operating conditions (i.e.,  $N/N_{CD}$ ,  $U_g$ ), the  $x$  and  $z$  exponents in the scale-up model determine how fast the mass transfer is reached. The dependence on of the T/D ratio is assumed to be the same as for air scale-up correlation discussed previously, because these geometrical parameters are held constant.

Since syngas-liquid mass transfer rates are difficult to obtain, it is highly important to predict the  $k_L a$  values for CO in syngas from those of O<sub>2</sub> in air. Such a correlation can be obtained by assuming: (i) the same dependence on the T/D ratio, and (ii) the hydrodynamic conditions produced by a given  $N$  and  $U_g$  in air are identical to those produced using syngas of the same  $N$  and  $U_g$ . Hence, with the temperature compensation to 30°C, the constant in Eq (4.6) becomes  $K = 2.0$  and by simply dividing Eqs. (4.13) and (4.6), the dissolved CO mass transfer rates can be predicted from those of air according to:

$$k_{L a_{CO}} = 5.84 \left( \frac{N}{N_{CD}} \right)^{0.55} U_g^{0.38} k_{L a_{air}} \quad (4.14)$$

where  $k_{L a_{CO}}$  and  $k_{L a_{air}}$  are gas-liquid mass transfer coefficients for CO from artificial syngas (20% CO, 18% CO<sub>2</sub>, 52% N<sub>2</sub>, 10% H<sub>2</sub>) and for O<sub>2</sub> from air, respectively, both at 30°C. Equation (4.14) correlates CO mass transfer rates in a STR operating in the ALC region and

is based on the air scale-up correlation of 282 data points obtained from the literature (Eq. (4.6)) to  $R^2 = 0.97$ . It should be noted that Eq. (4.14) is a scale-up correlation for CO  $k_L a$  values from artificial syngas as a function of  $k_L a$  from air, given the assumptions above are satisfied. For a single vessel size studied in this work ( $T = 0.211$  m,  $D/T = 0.35$ ), Fig. 4.22 shows measured versus predicted CO mass transfer rates from those of air at 30°C.

Similarly by dividing Eqs. (4.6) and (4.12), the  $k_L a$  values for pure O<sub>2</sub> can be predicted using  $k_L a$  values from air at 20°C:

$$k_L a_{O_2} = 0.76 \left( \frac{N_{CD}}{N U_g^{0.41}} \right)^{0.3} k_L a_{air} \quad (4.15)$$

Figure 4.23 shows measured dissolved O<sub>2</sub> mass transfer rates predicted from those of air.

## 4.5 Gas-Liquid Scale-Up Model Discussion

Scale-up in mixing applications, such as of a volumetric gas-liquid mass transfer coefficient ( $k_L a$ ) in a STR, is based on a similarity principle. For transferring bench-top data to industrial scale, according to the similarity principle, it is reasonable to assume that the following scaling criteria are applicable: (i) geometric similarity, (ii) kinematic similarity, and (iii) dynamic similarity. The geometric similarity requires constant ratios between length dimensions in both vessels. The kinematic similarity requires that the ratios of the velocities between corresponding points in geometrically similar vessels are equal. The dynamic similarity occurs between two vessels if they are geometrically and kinematically similar, and the ratios of forces between the corresponding points in both vessels are the same.

The skill required in scaling mixing applications is knowing which parameters to scale, because not all may be satisfied simultaneously. In fact, it is often not possible to achieve "complete similarity" and a dimensional analysis cannot be used to solve every problem (Zlokarnik 2001). The kinematic and dynamic similarities may be combined into hydrodynamic similarity. Geometric similarity is usually satisfied in practice, since the bench-top and industrial size STRs are generally the same shape. Hence, one may think of a STR scale-up as a complete hydrodynamic similarity between the two geometrically similar vessels, which implies a similarity in flow patterns. Studies on flow patterns in STRs are reported by Metzner and Taylor (1960), Smith (1972), and Aiba (1959). Smith reported "Gas flow pattern is important. It controls the degree of recirculation and back mixing of the gas phase, which in turn determines the mean concentration driving force for mass transfer". Similar flow patterns mean similar ratios of forces between the bench-top and industrial scale STRs.

In mixing applications, the degree of complexity often makes dimensional analysis not applicable. Often different correlations apply in the laminar and turbulent regimes, which supports the fact that scale-up in a STR may be applicable in a certain flow regime. Thus, the guiding hypothesis in the general scale-up model (Eq. (4.3)) is: (i) determining an empirical correlation as a function of scaling parameters, for the most useful operating regime which must be physically possible in the scale-up range studied, (ii) choosing scaling parameters to describe approximately the same flow patterns between the bench-top and industrial scales while the geometry aspect ratios are fixed, (iii) developing a correlation model by normalizing the scaling parameters from (i) and (ii) including other relevant parameters of physical importance to the system, and (iv) performing scale-up analysis

around the useful operating regime which will allow for the flow pattern similarity between geometrically similar reactors.

For a general STR scale-up model as shown previously in Eq. (4.3), the empirical correlation for impeller speed in the most useful scale-up operating regime (i.e., complete dispersion Eq. (2.8)) was already correlated by Nienow et al. (1977). The impeller speed ( $N$ ) is used as a scaling parameter since it introduces the power by which STR flow patterns are generated. Additionally, a STR scale-up model developed for gas-liquid mass transfer includes superficial gas velocity ( $U_g$ ) and tank to impeller diameter ratio ( $T/D$ ), as physically important parameters in affecting gas-liquid mass transport. Then the scale-up is performed around the useful operating regime in range of  $0.25 \leq N/N_{CD} \leq 3.0$ , as shown in Table 4.1, which will assure hydrodynamic similarity between different reactor sizes. It should be noted that, when  $N/N_{CD} = 1$  all reactors will operate their lowest power demand.

Similarly, a gas-liquid scale-up model for air-lift reactors (ALR), and bubble column reactors (BCR) can be developed if one considers the following: The useful operating regime in which scale-up is to be performed is for the maximum gas holdup ( $\epsilon_{max}$ ), with the gas buoyancy power ( $P_b$ ) being entirely responsible for the flow pattern generation and defined by:

$$P_b = Q_g H g (\rho - \rho_G) \quad (4.16)$$

In STRs, the flow patterns are generated by the impeller, attached to an electric motor, drawing an electric power while the contribution of the buoyancy power introduced by the gas is negligible at  $H = T$ . In ALRs and BCRs, all the mixing power available is induced by the buoyancy power ( $P_b$ ) which determines the flow patterns. In other words, both ALRs and

BCRs gas-liquid transport phenomena (i.e.,  $k_L a$  and  $\varepsilon$  measurements) are entirely influenced by the buoyancy power. In gas-liquid mixing, the buoyancy power ( $P_b$ ) for ALRs and BCRs of a typical geometry  $H/T = 10$ , is usually much bigger than in STRs of similar size. It seems reasonable that the scale-up of an ALR or a BCR can be completed using the buoyancy power ( $P_b$ ) analog to impeller power used for a STR scale-up analysis. To proceed with the gas-liquid scale-up, it is desirable to choose the most useful operating regime for which the scale-up is to be performed. Such a regime could be around the maximum gas holdup ( $\varepsilon_{\max}$ ) that will occur and the buoyancy power needed to reach this value,  $P_{b\varepsilon_{\max}}$ . The regime corresponding to the maximum gas holdup is analogous to complete dispersion. Thus, a correlation of the buoyancy power as a function of reactor geometry and gas flow rate is desired for a range of reactor sizes similar to Eq. (4.7), perhaps in the form:

$$P_{b\varepsilon_{\max}} = f(Q_g, D, H) \quad (4.17)$$

where  $D$  is the reactor diameter, and  $H$  is the static liquid height. Then, a suggested gas-liquid scale-up model for ALRs or BCRs similar to the STR model (Eq. (4.3)) is of the following form:

$$\frac{k_L a}{U_g^z} = K \left( \frac{P_b}{P_{b\varepsilon_{\max}}} \right)^x \left( \frac{H}{D} \right)^y \quad (4.18)$$

In Eq. (4.18) the mixing parameter  $P_b/P_{b\varepsilon_{\max}}$  presents the degree of gas-liquid mixing at the mixing buoyancy power ( $P_b$ ) relative to the degree of gas-liquid mixing at the buoyancy power at which maximum gas holdup occurs ( $P_{b\varepsilon_{\max}}$ ). This mixing parameter ( $P_b/P_{b\varepsilon_{\max}}$ ) is analog to the dispersion parameter ( $N/N_{CD}$ ) and it is used to describe the flow pattern

similarity between reactors of different size (i.e., gas-liquid hydrodynamics) while the geometric similarity is satisfied. Although, the mixing parameter is a function of superficial gas velocity ( $U_g$ ), the  $U_g$  term is included in Eq (4.18) since the same flow patterns can be generated at different  $U_g$ 's in different reactor diameters resulting in the same mixing parameter at different superficial gas velocity. The  $U_g$  term is responsible for the gas-liquid mass transfer driving potential. Similarly, the exponents  $x$  and  $z$  account for the hydrodynamic influence and mass transfer driving potential, respectively, and the important interplay between the two necessary for a scale-up analysis. The  $H/D$  aspect ratio is included to account for different liquid height and reactor diameters similar to Eq (4.3). Note that for the scale-up model in Eq. (4.18), the reactor geometry and the geometry of the gas distribution plates need to be standardized in a similar way as the STR and 6DT impeller geometries. Otherwise, additional terms must be included to account for the geometric similarity.

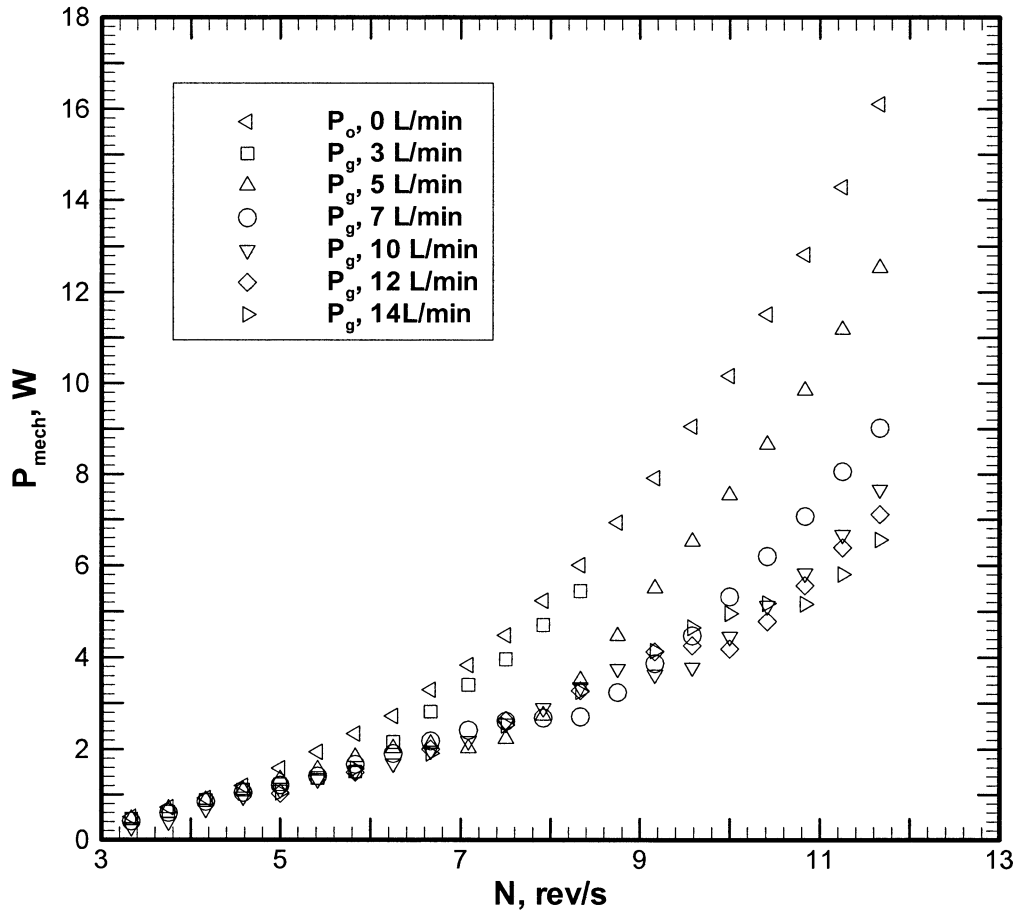


**Figure 4.1:** Unaerated  $P_o$  and aerated  $P_g$  powers as a function of  $N$  at constant  $Q_g$ .

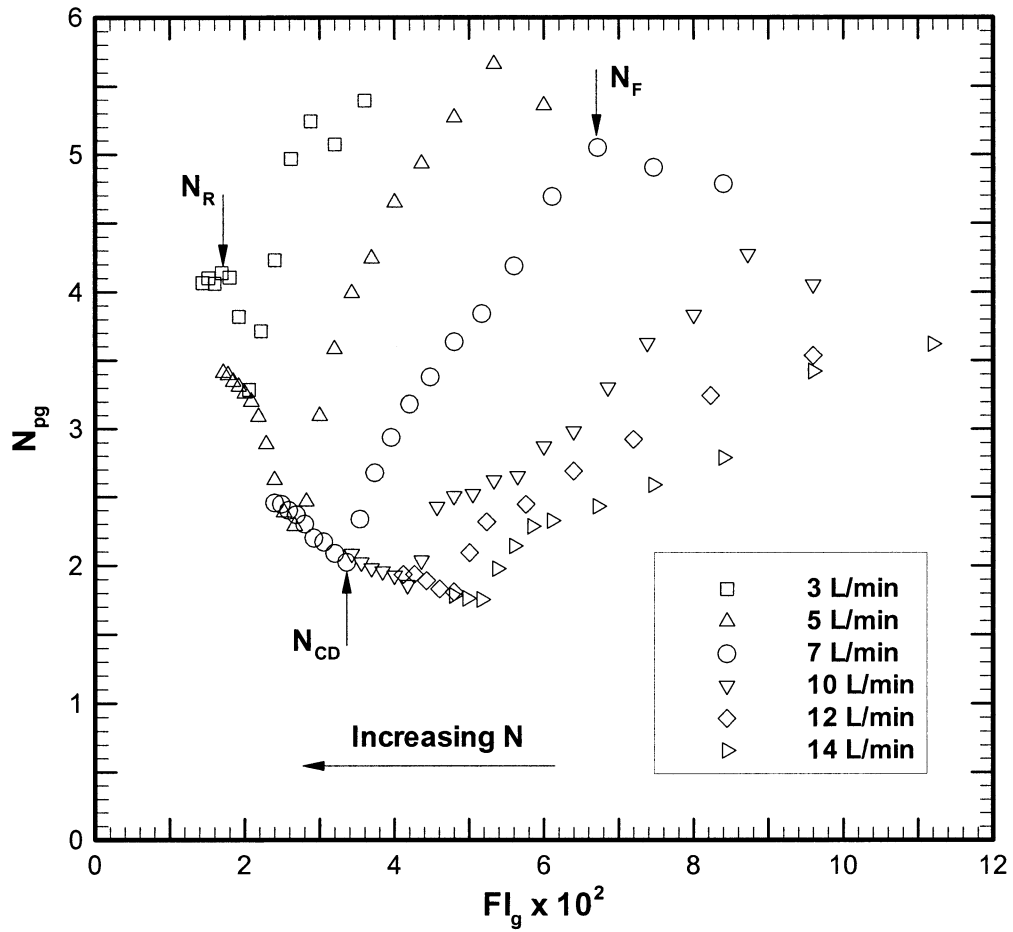


**Figure 4.2:** Gassed power number  $N_{pg}$  vs. the flow number  $Fl_g$  at constant  $Q_g$ .

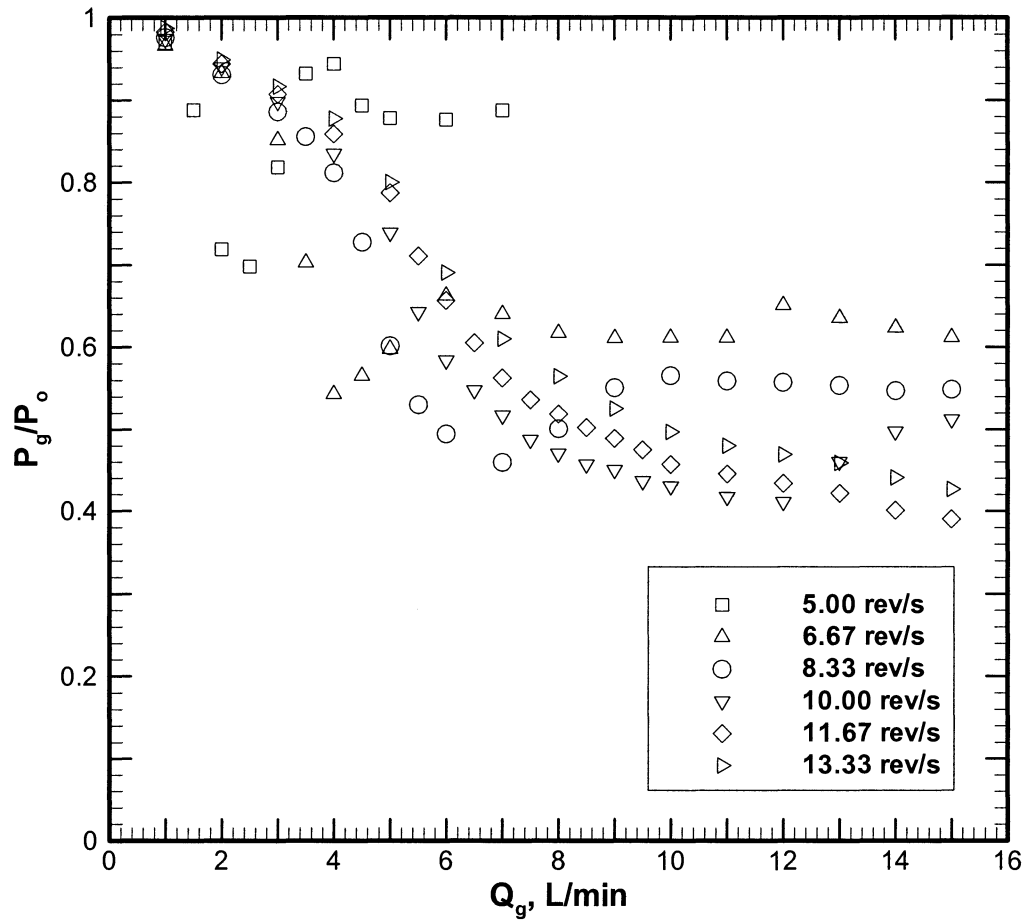
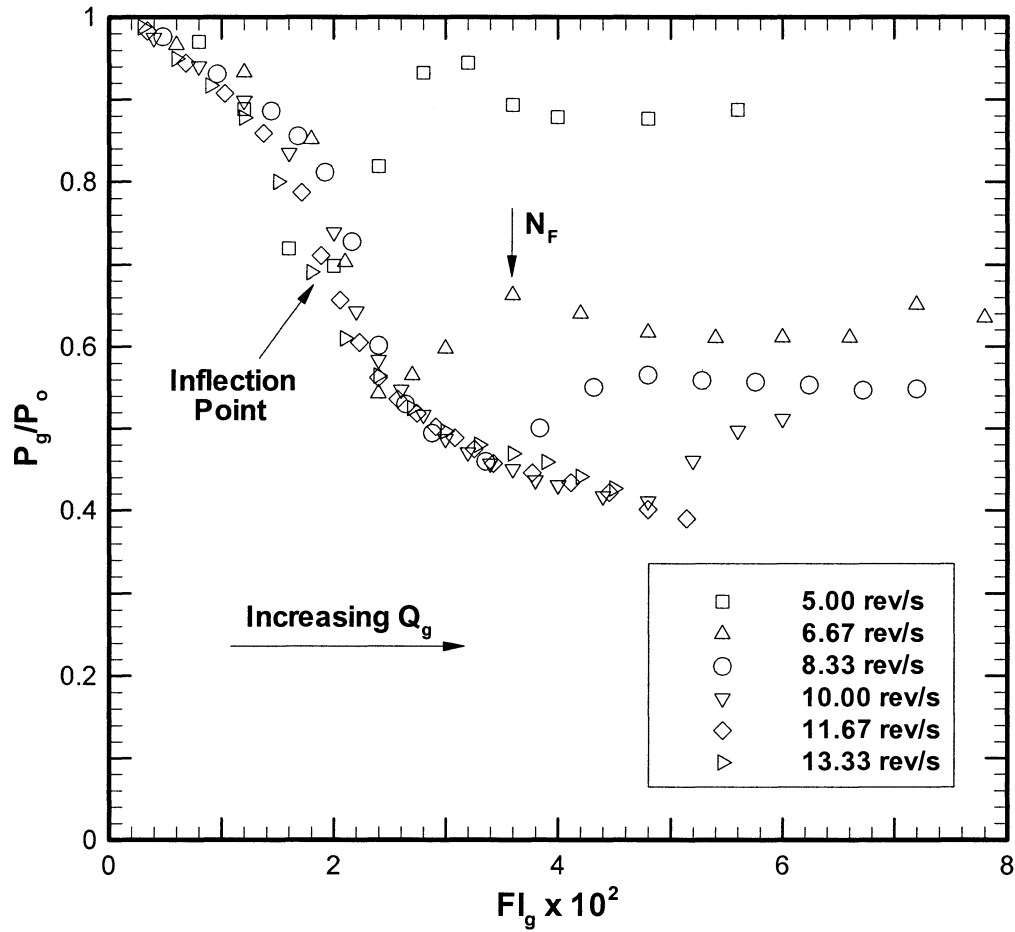
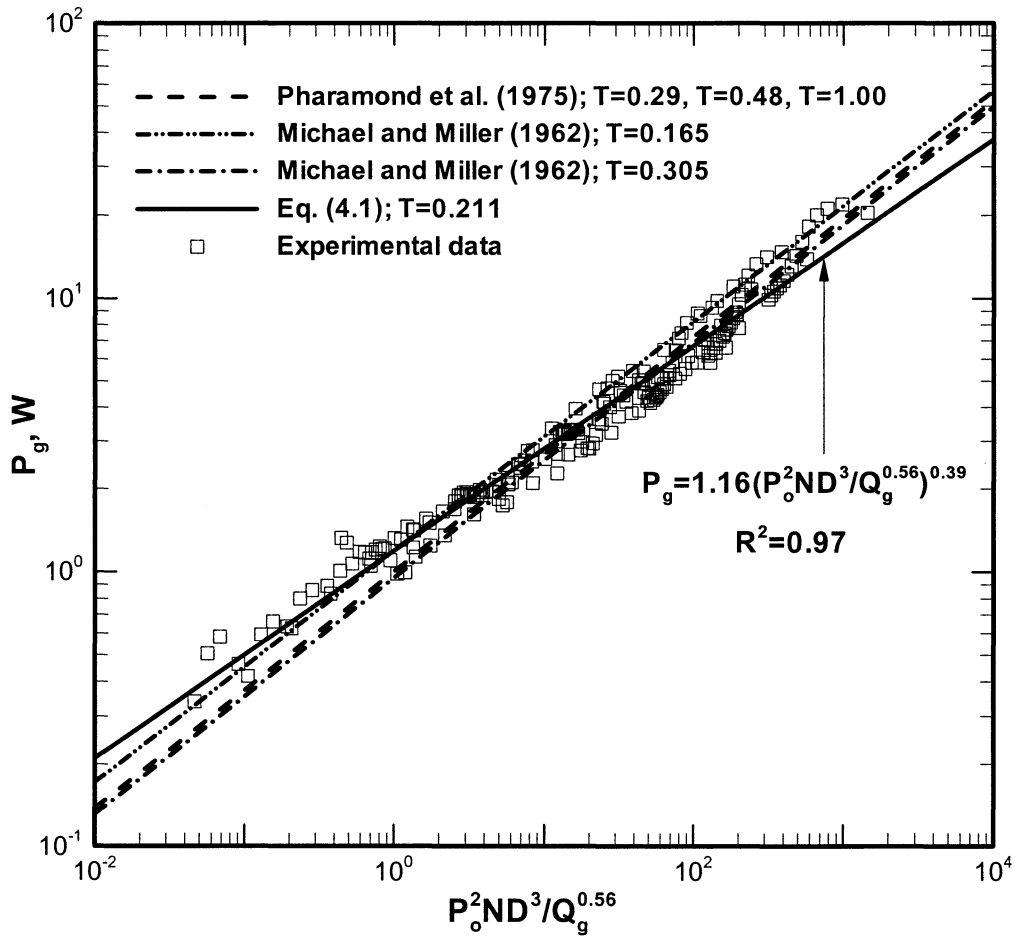


Figure 4.3: Gassed to ungassed power ratio  $P_g/P_o$  vs. gas flow rate  $Q_g$  at constant  $N$ .



**Figure 4.4:** Gassed to ungasged power ratio  $P_g/P_o$  vs. Flow number  $Fl_g$  at constant  $N$ .



**Figure 4.5:** Gassed power ( $P_g$ ) vs.  $P_o^2 ND^3 / Q_g^{0.56}$  for air dispersed in tap water with  $D = 0.0747$  m standard disc turbine (6DT) in  $T = 0.211$  m tank.

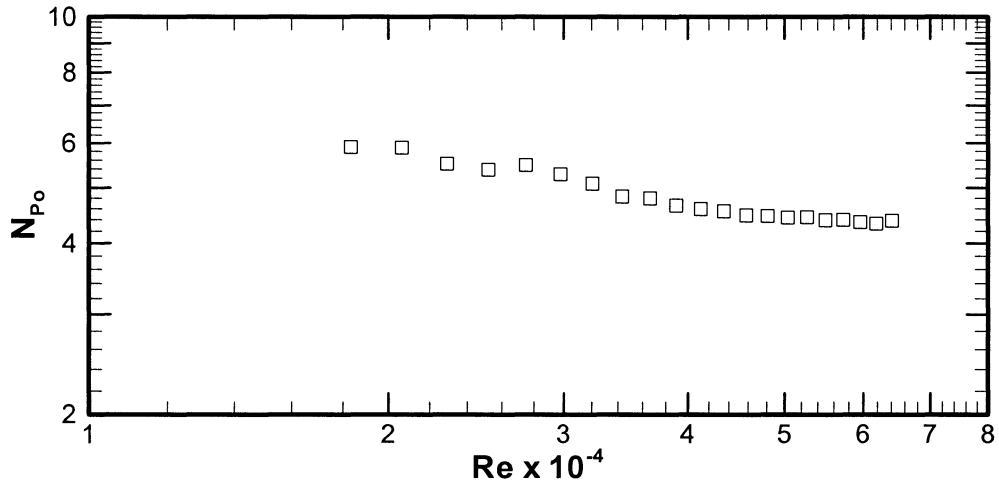


**Figure 4.6:** Power number ( $N_{po}$ ) vs Reynolds number ( $Re$ ) for  $x_1/D = 0.0167$ ,  $D/T = 0.35$ , and  $c = T/4$ .

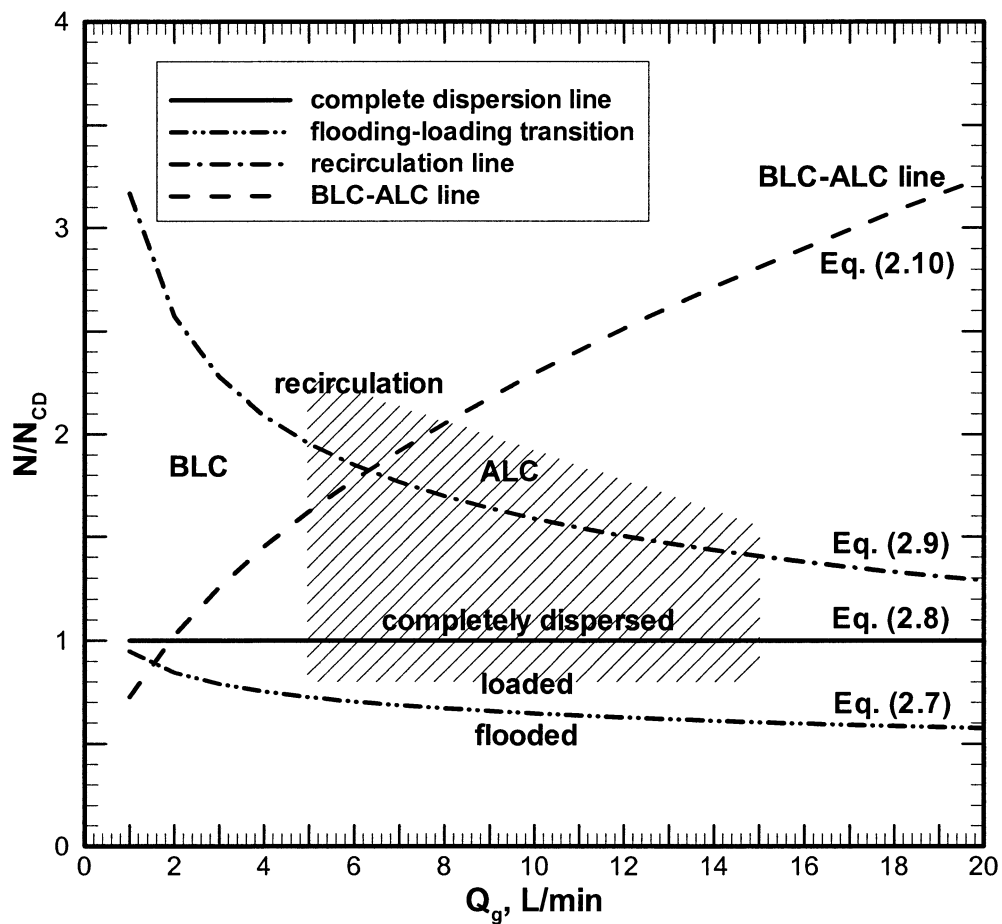


**Figure 4.7:** Hydrodynamic flow regime map for a  $T = 0.211$  m vessel and  $D/T = 0.35$ .

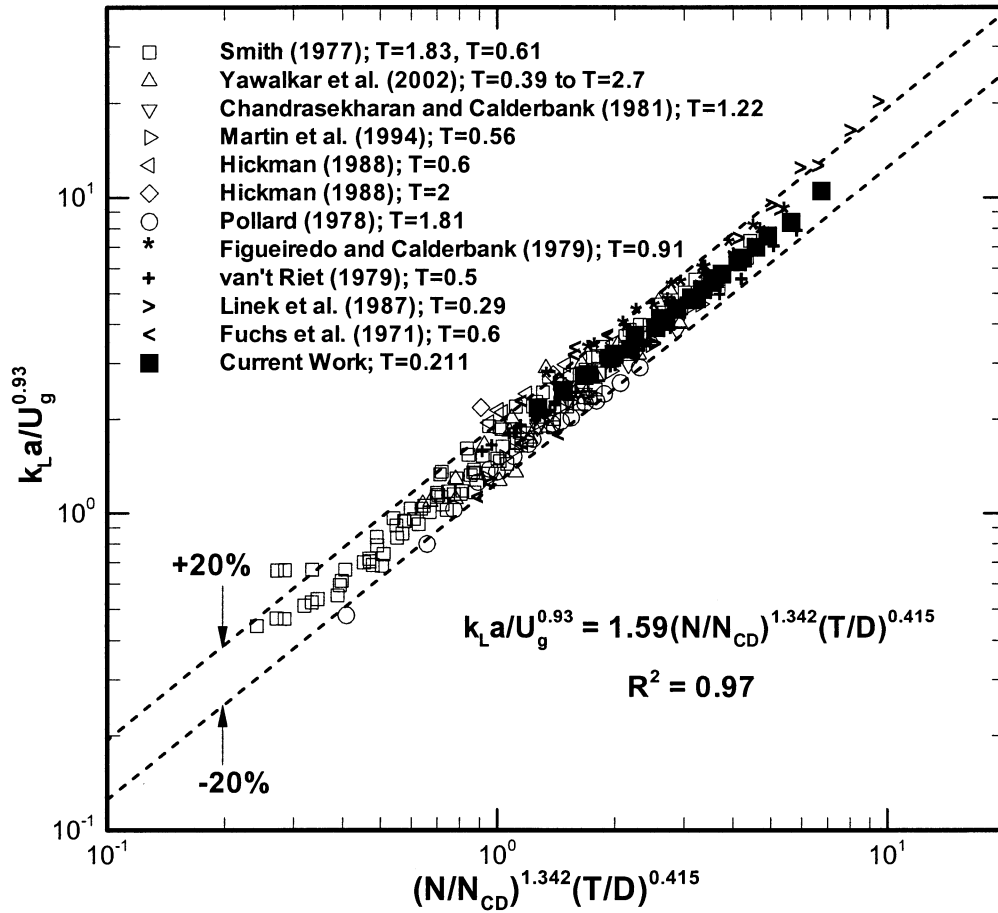


**Figure 4.8:** Scale-up correlation for volumetric gas-liquid mass transfer coefficient ( $k_L a$ ) in terms of relative dispersion parameter ( $N/N_{CD}$ ) and tank to impeller diameter ratio ( $T/D$ ).

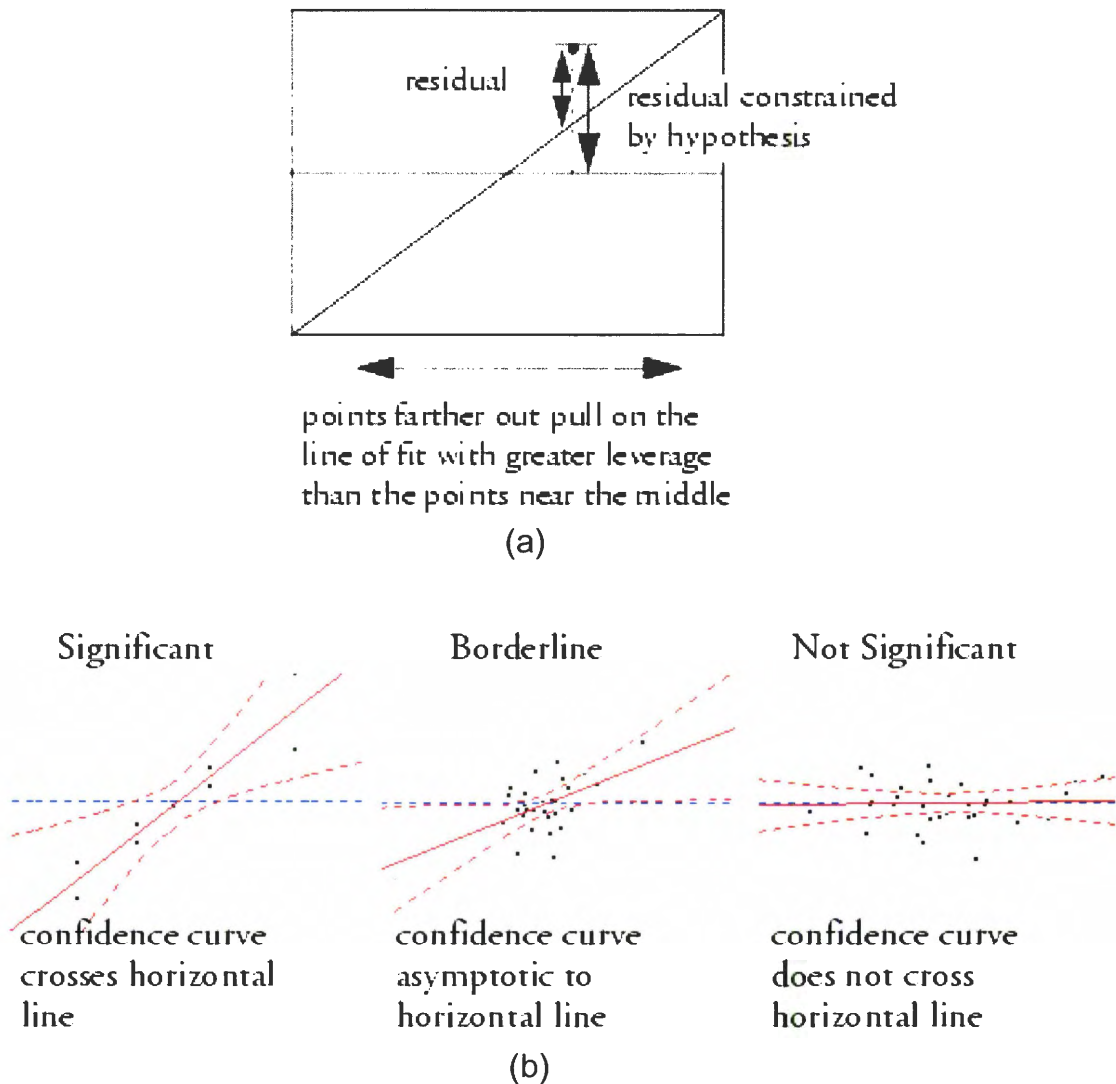


**Figure 4.9:** Illustration of a general leverage plot from JMP5.1 (a); comparison of significance shown in leverage plots (b), adopted from JMP5.1 (SAS Institute, Inc.).

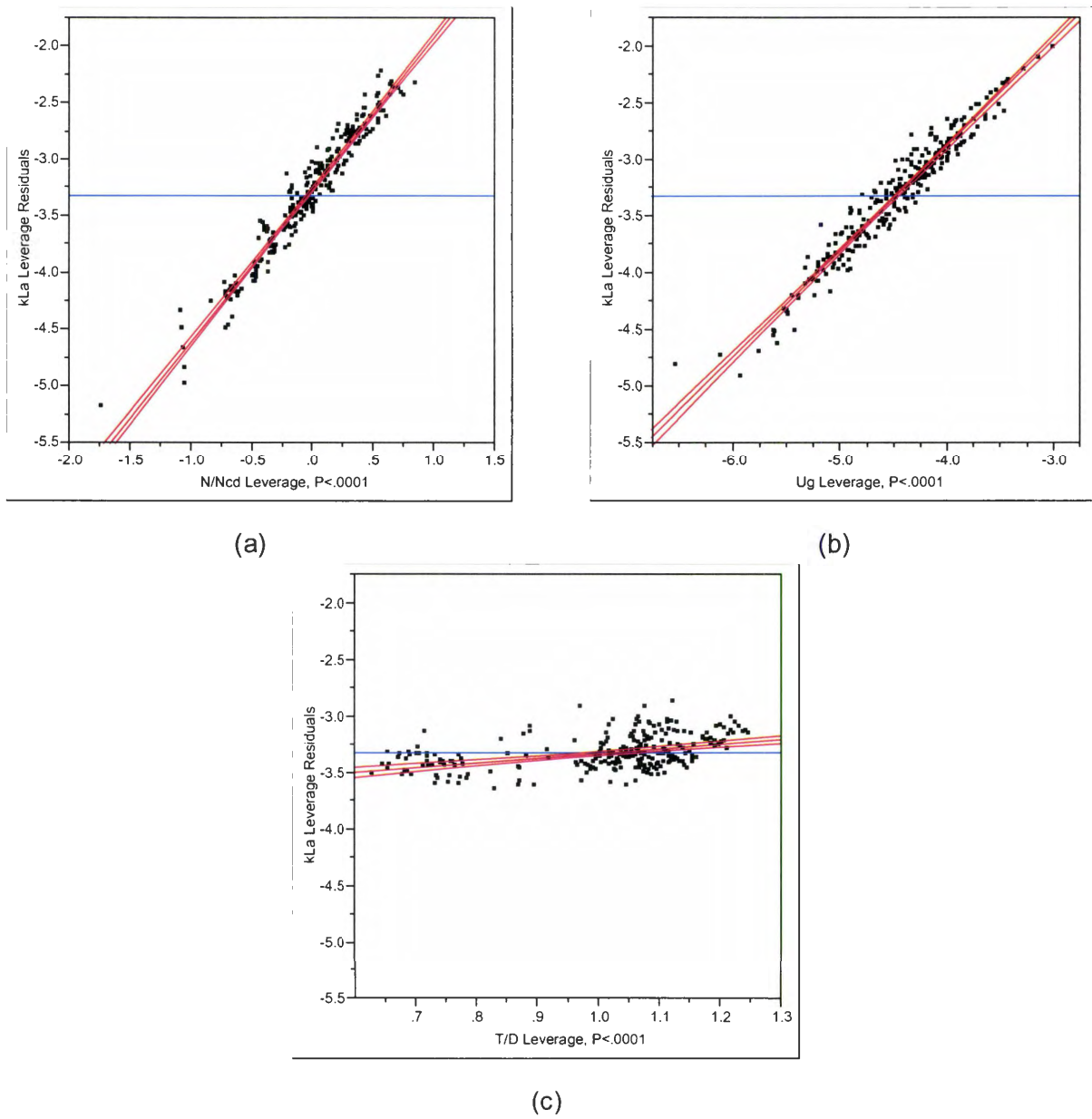


**Figure 4.10:** Contribution of the correlating parameters  $N/N_{CD}$  (a),  $U_g$  (b), and  $T/D$  (c) to the significance of the scale-up model of Eq. (4.3).

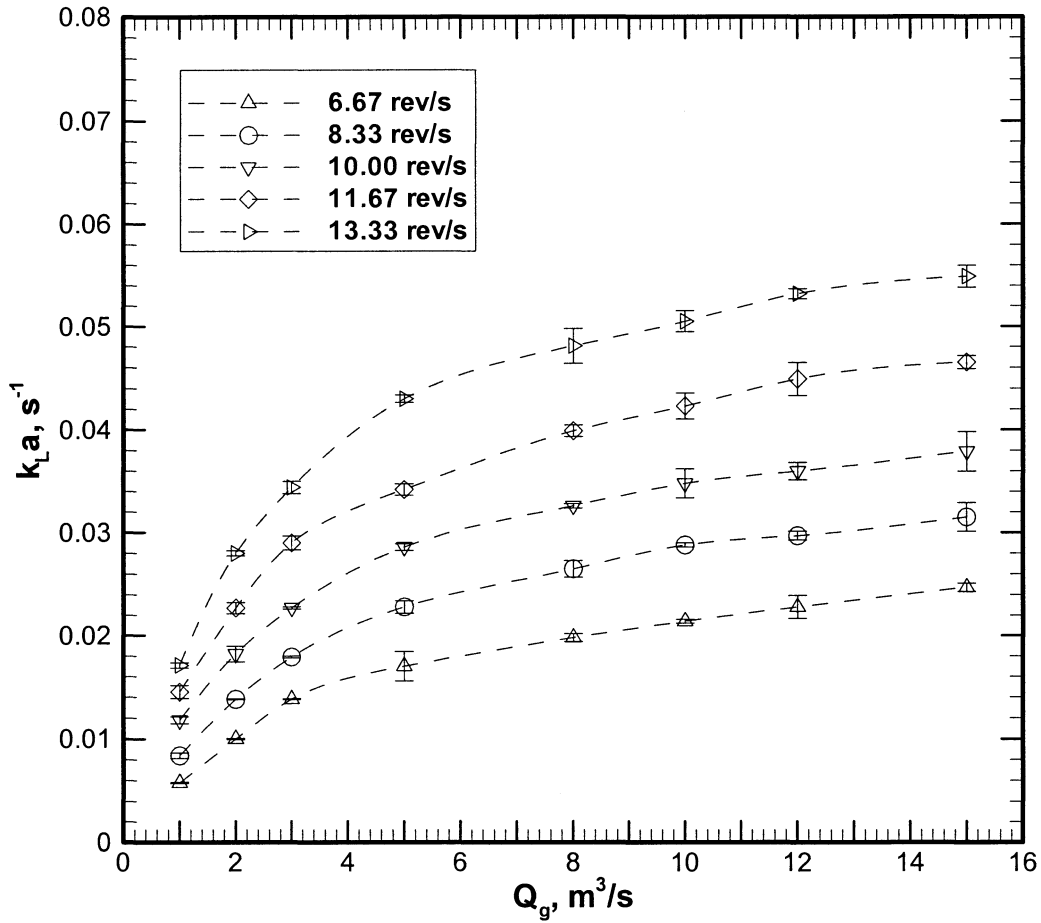


**Figure 4.11:** Volumetric mass transfer coefficient ( $k_{La}$ ) as a function of gas flow rate ( $Q_g$ ) at constant impeller speed ( $N$ ) for dispersed air in tap water with  $D = 0.0747$  m impeller in  $T = 0.211$  m vessel.

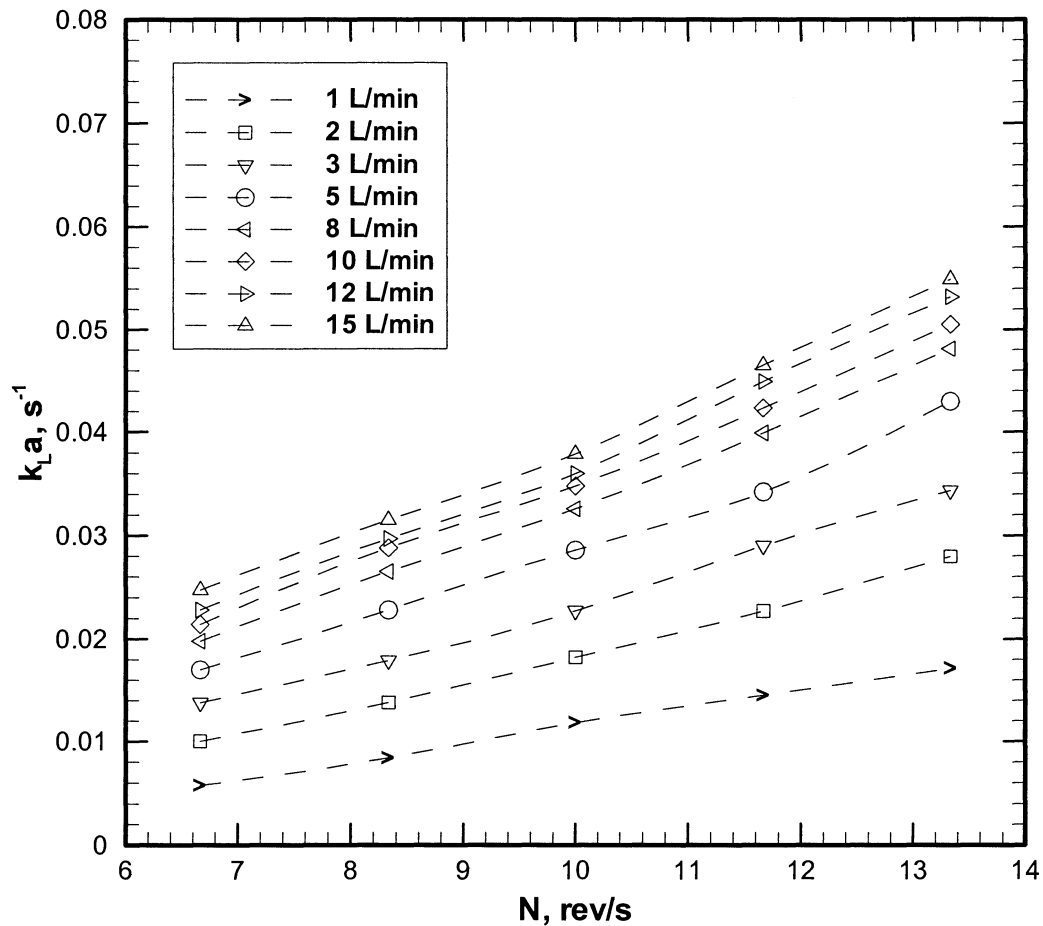


**Figure 4.12:** Volumetric mass transfer coefficient ( $k_L a$ ) as a function of impeller speed ( $N$ ) at constant gas flow rate ( $Q_g$ ) for dispersed air in tap water with  $D = 0.0747$  m impeller in  $T = 0.211$  m vessel.

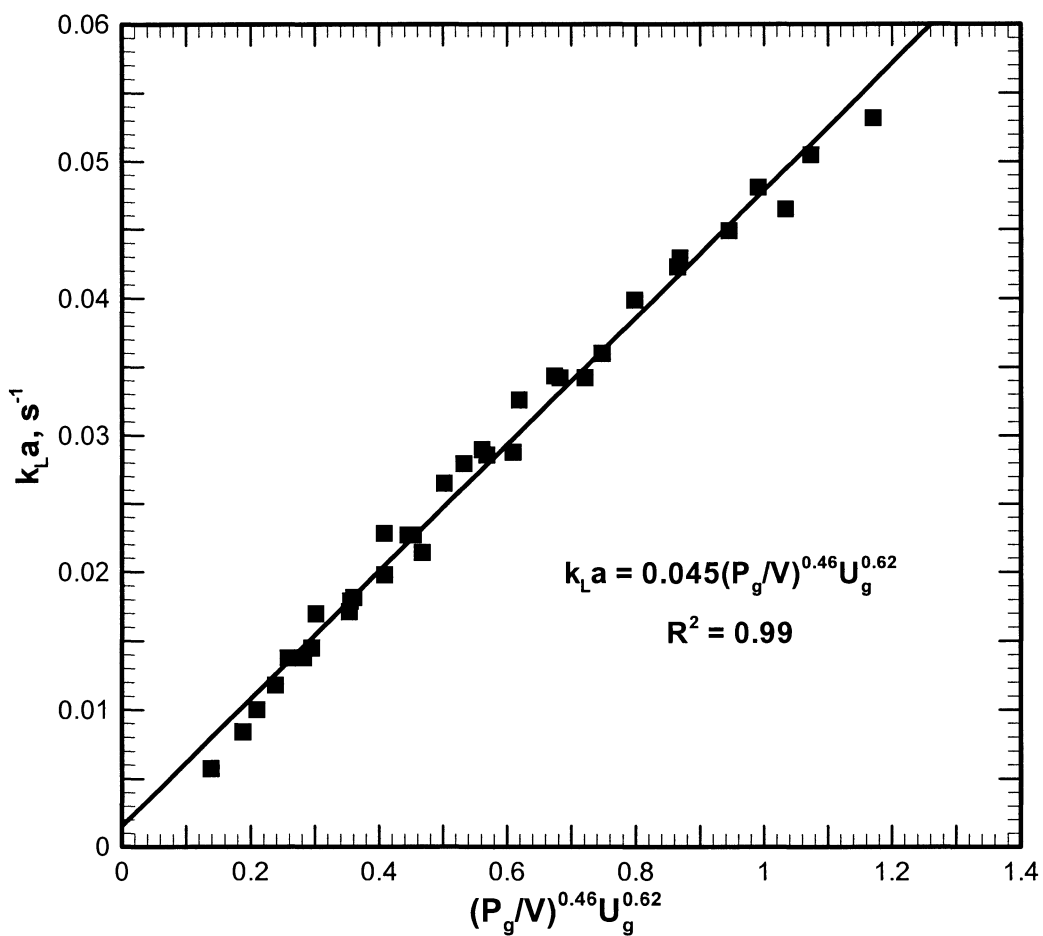


**Figure 4.13:** Volumetric mass transfer coefficient ( $k_L a$ ) as a function of gassed power density ( $P_g/V$ ) and superficial gas velocity ( $U_g$ ) for dispersed air in tap water in  $T = 0.211$  m vessel and  $D/T = 0.35$ .

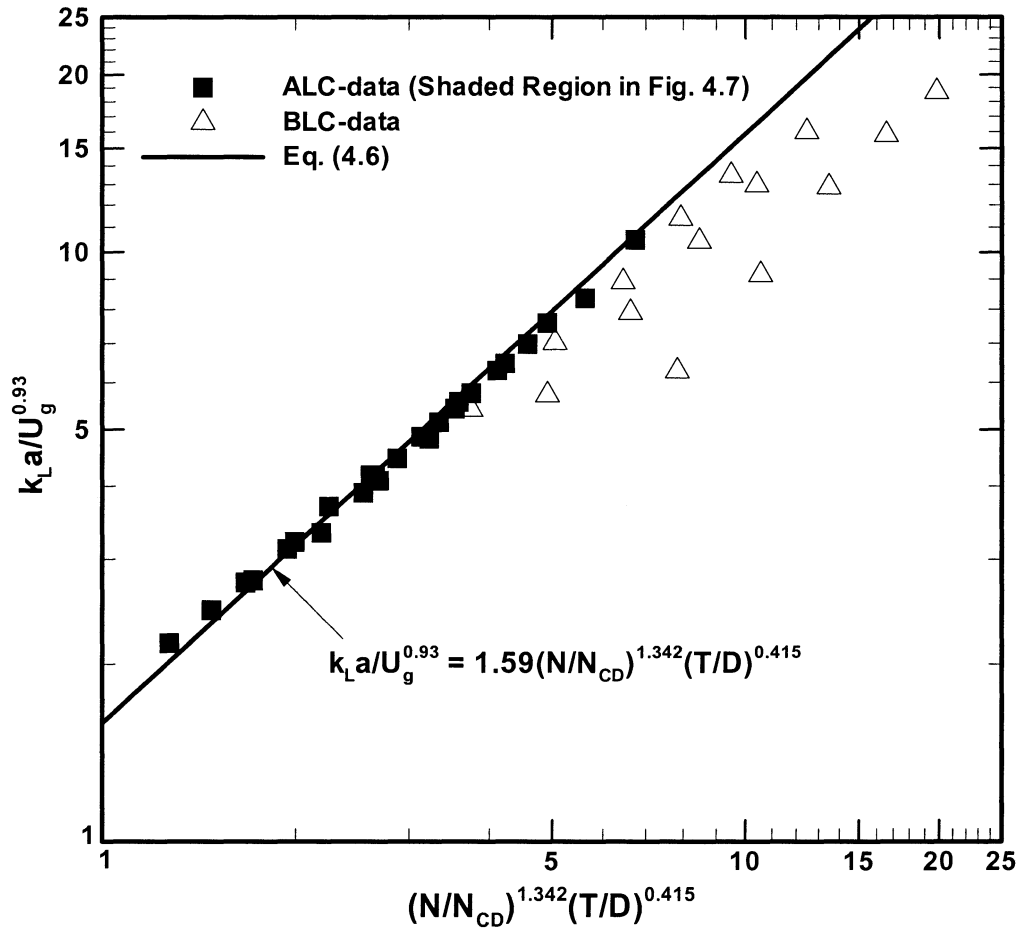


**Figure 4.14:** Comparison of ALC and BLC data to the flow regime dependant scale-up correlation for volumetric gas-liquid mass transfer from dispersed air in tap water (Eq. (4.6)).

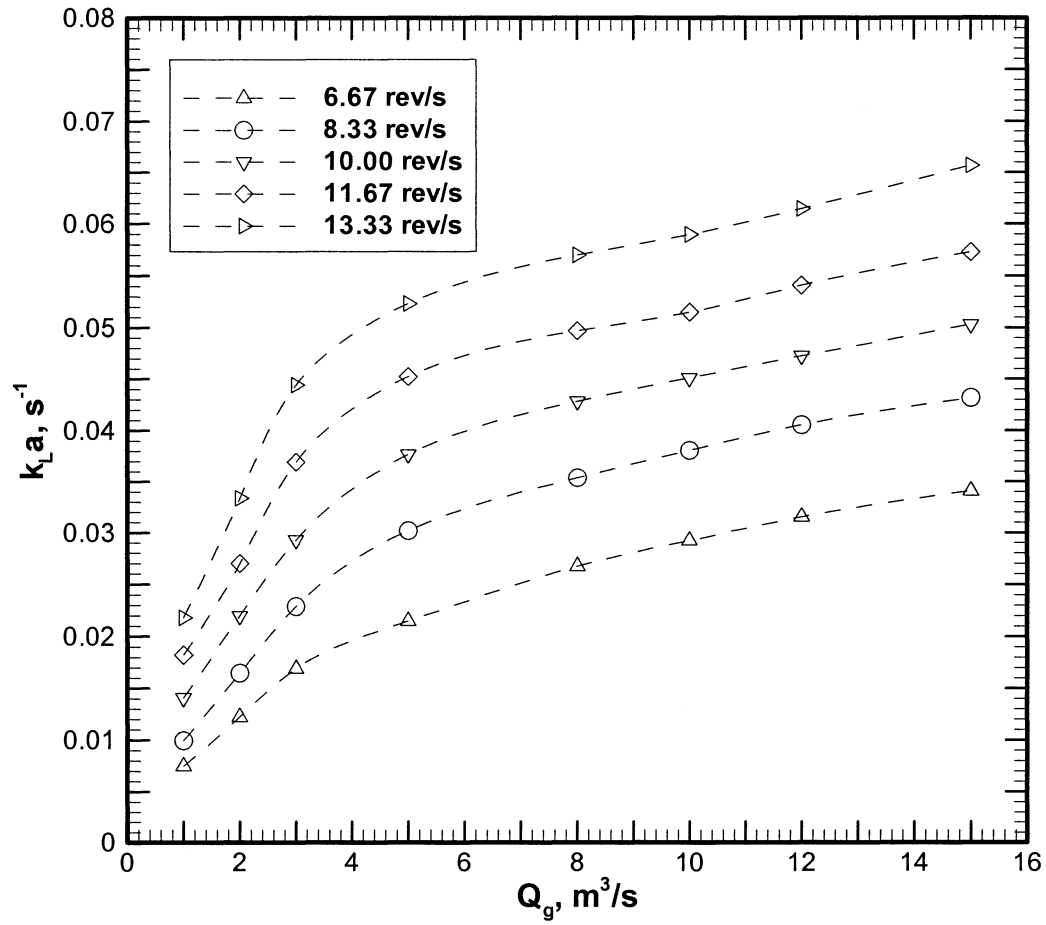


**Figure 4.15:** Volumetric mass transfer coefficient ( $k_{La}$ ) as a function of gas flow rate ( $Q_g$ ) at constant impeller speed ( $N$ ) for dispersed oxygen in tap water with  $D = 0.0747$  m impeller in  $T = 0.211$  m vessel.

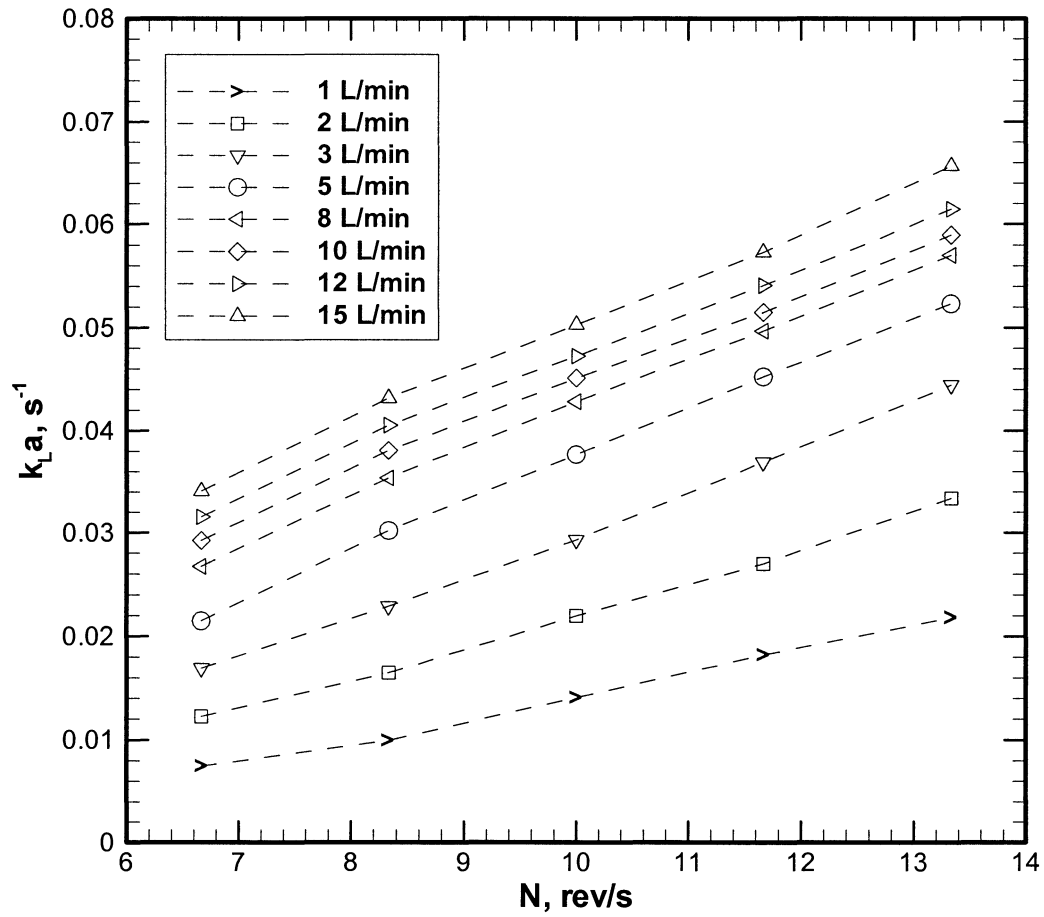


**Figure 4.16:** Volumetric mass transfer coefficient ( $k_La$ ) as a function of impeller speed ( $N$ ) at constant gas flow rate ( $Q_g$ ) for dispersed oxygen in tap water with  $D = 0.0747$  m impeller in  $T = 0.211$  m vessel.

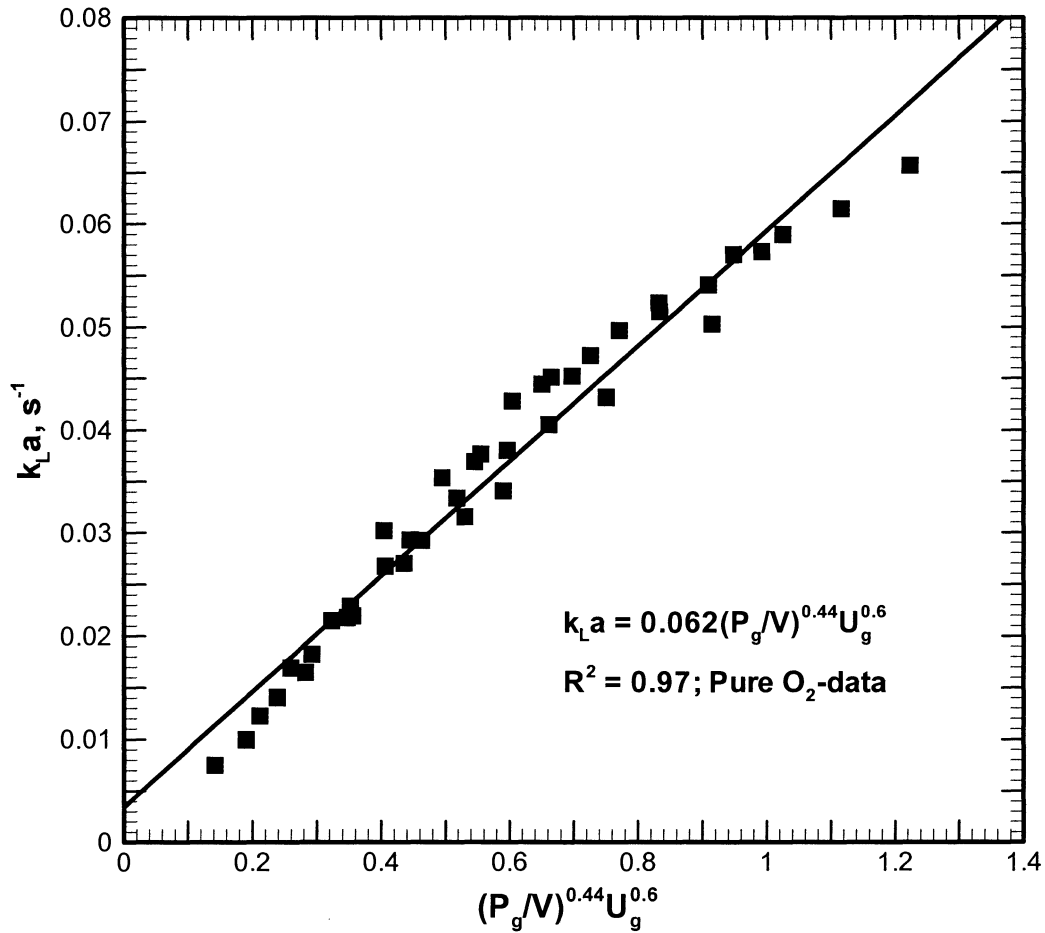


**Figure 4.17:** Volumetric mass transfer coefficient ( $k_{L,a}$ ) as a function of gassed power density ( $P_g/V$ ) and superficial gas velocity ( $U_g$ ) for dispersed oxygen in tap water in  $T = 0.211$  m vessel and  $D/T = 0.35$ .

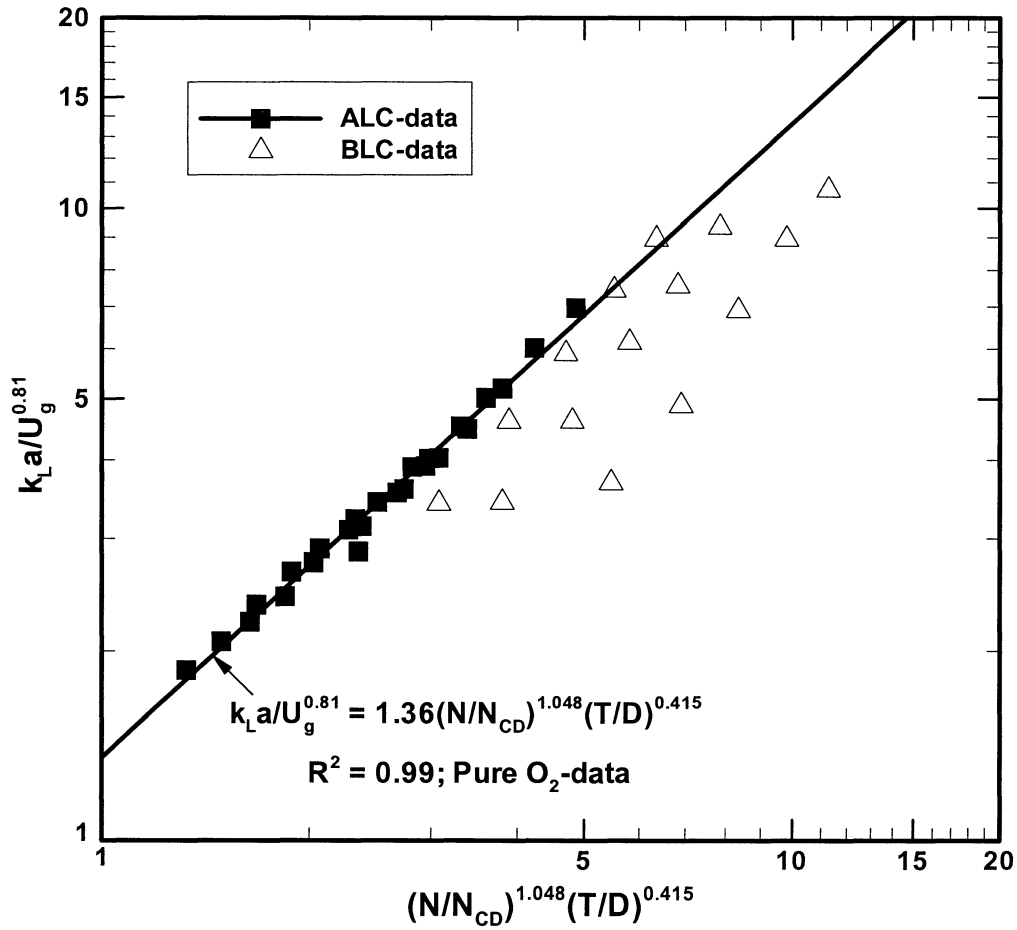


**Figure 4.18:** Flow regime dependence of ALC and BLC data in the scale-up correlation for volumetric gas-liquid mass transfer from dispersed oxygen in tap water at 25°C.

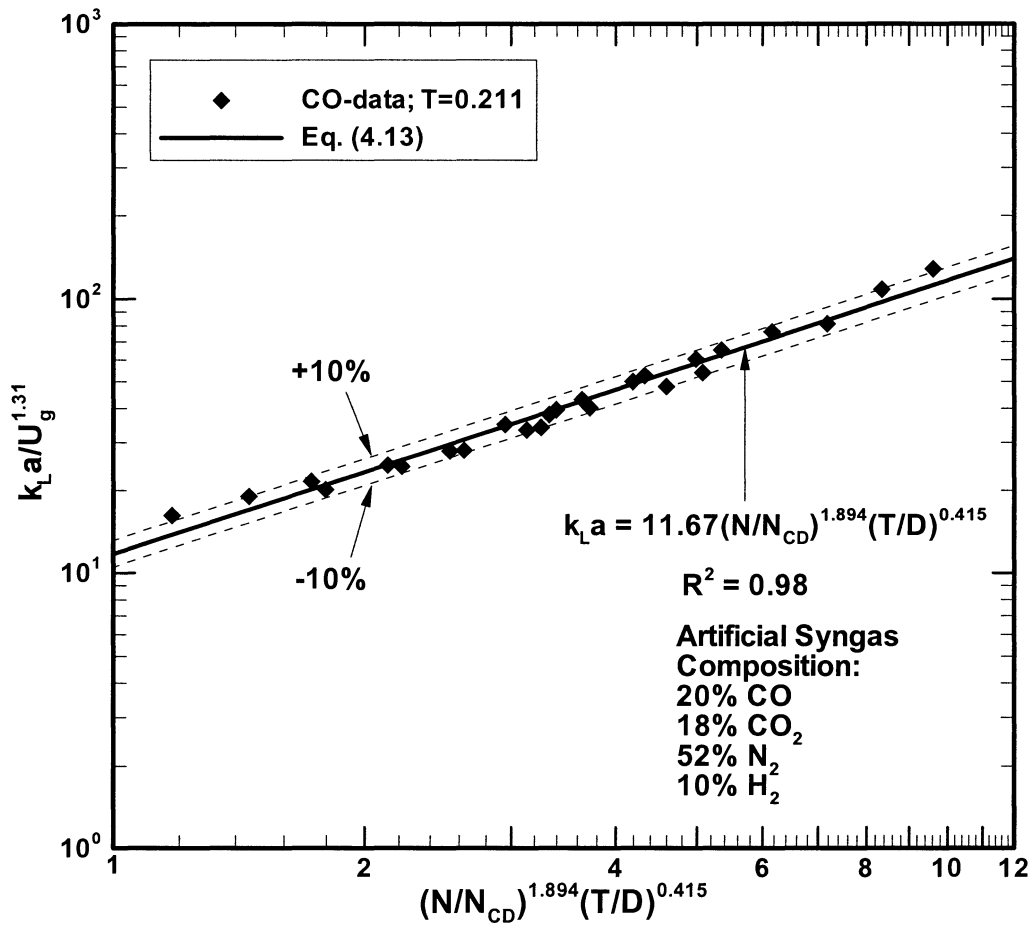


**Figure 4.19:** Carbon-monoxide mass transfer scale-up correlation in the ALC region using an artificial syngas blend of 20% CO, 18%CO<sub>2</sub>, 52%N<sub>2</sub>, and 10% H<sub>2</sub> in tap water at 30°C.

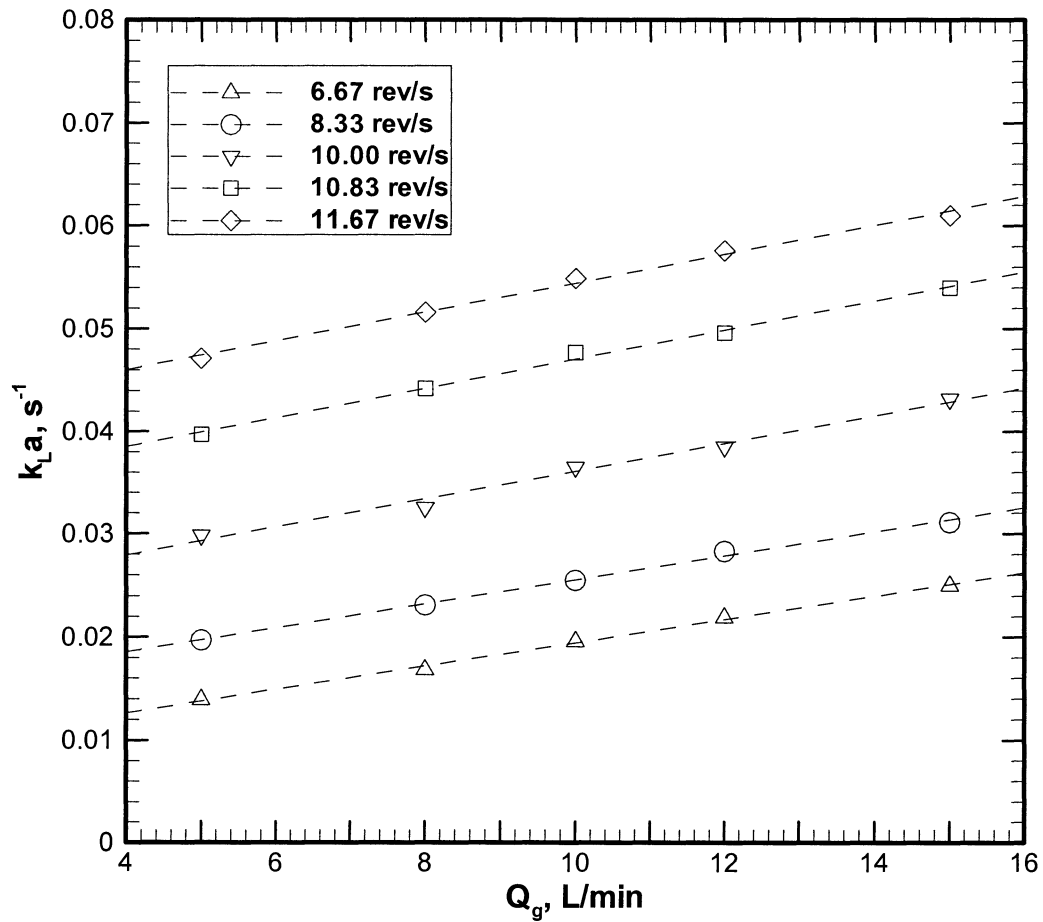


**Figure 4.20:** Volumetric mass transfer coefficient ( $k_L a$ ) as a function of gas flow rate ( $Q_g$ ) at constant impeller speed ( $N$ ) for dispersed artificial syngas in tap water with  $D = 0.0747$  m impeller in  $T = 0.211$  m vessel.

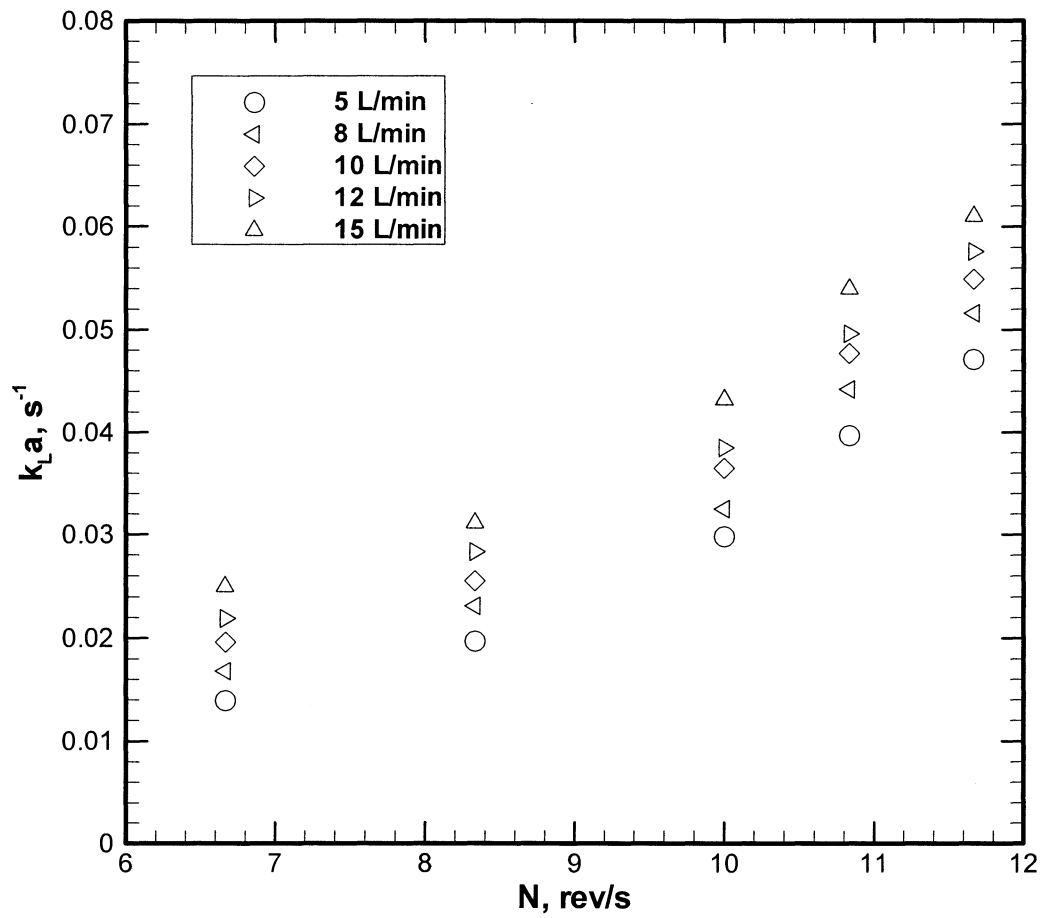


**Figure 4.21:** Volumetric mass transfer coefficient ( $k_L a$ ) as a function of impeller speed ( $N$ ) at constant gas flow rate ( $Q_g$ ) for dispersed artificial syngas in tap water with  $D = 0.0747$  m impeller in  $T = 0.211$  m vessel.

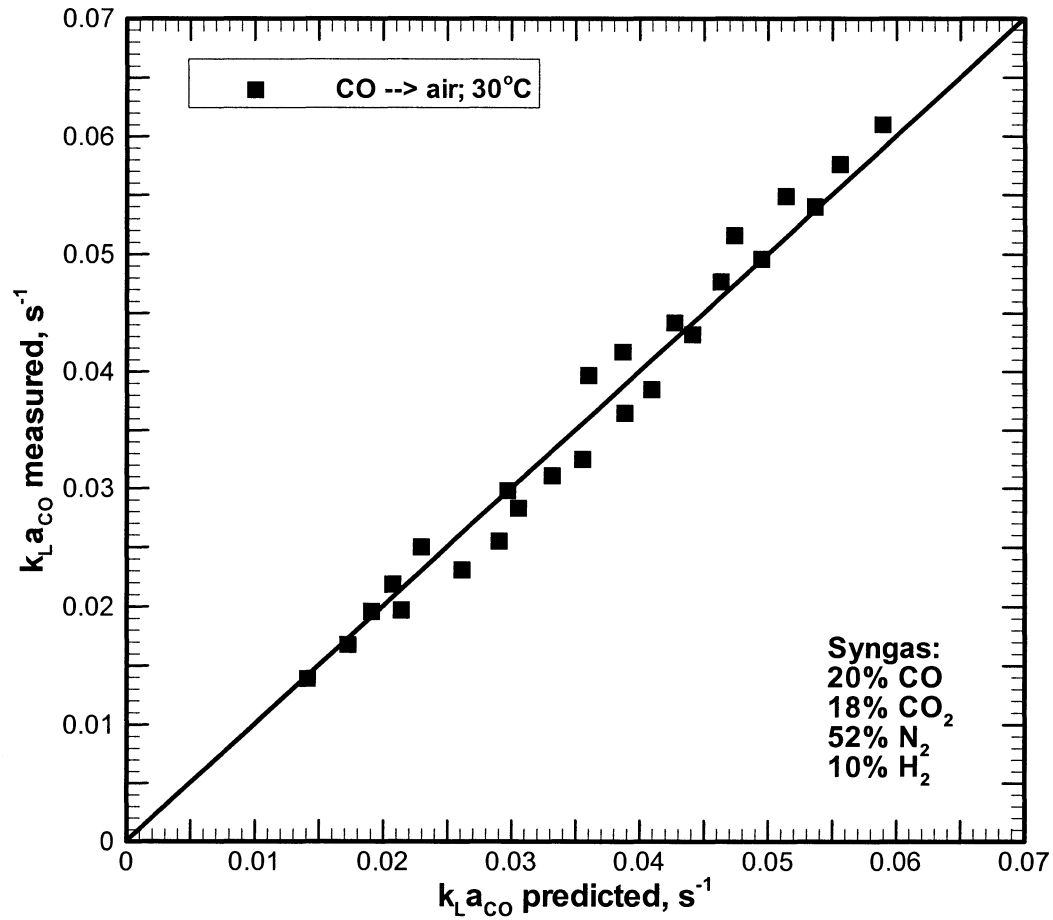


**Figure 4.22:** Predicted mass transfer rates for carbon-monoxide from air in tap water at 30°C sparging artificial syngas (20% CO, 18% CO<sub>2</sub>, 52% N<sub>2</sub>, 10% H<sub>2</sub>) using Eq. (4.14) in T = 0.211 m vessel and D/T = 0.35 in the ALC region.

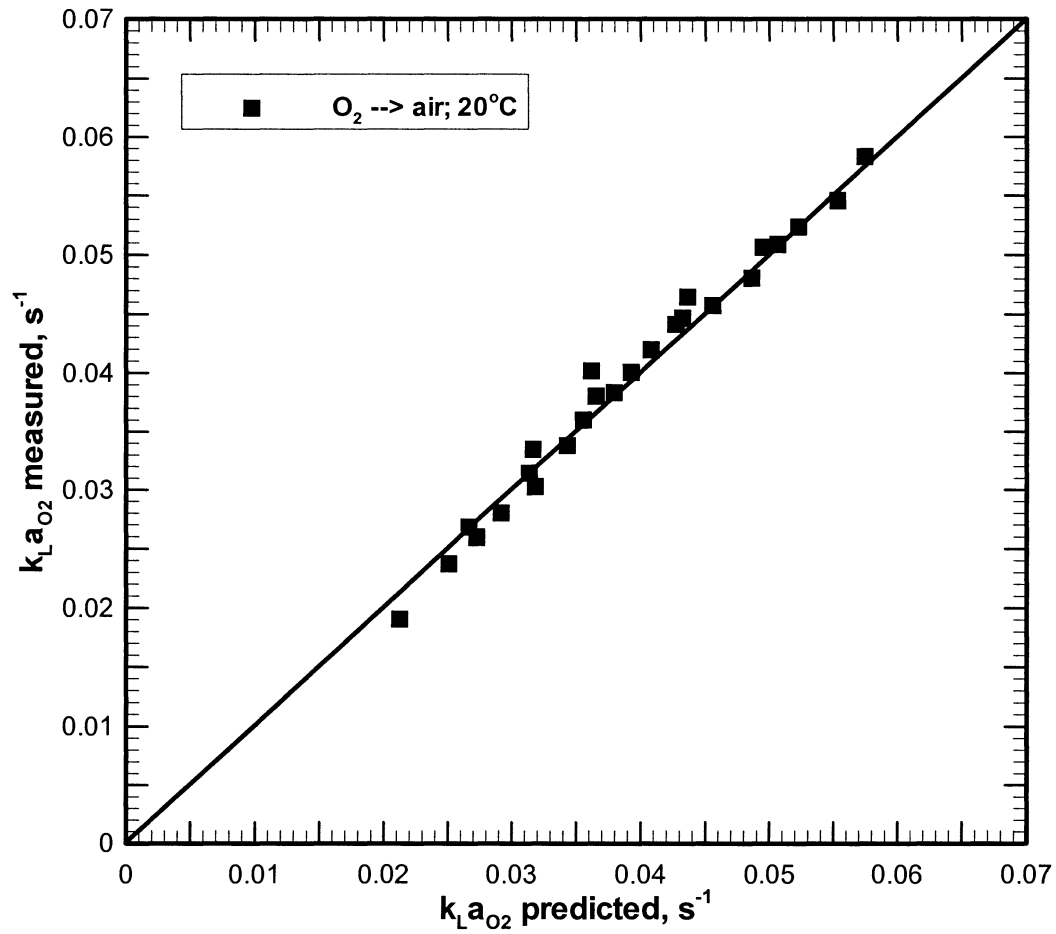


**Figure 4.23:** Dissolved  $O_2$  mass transfer rates predicted from air in tap water at  $20^\circ\text{C}$  from Eq. (4.15) in  $T = 0.211$  m vessel and  $D/T = 0.35$  in the ALC region.

## CHAPTER 5: CONCLUSIONS

### 5.1 Summary

Power requirements for a STR ( $T = 0.211$  m and  $D/T = 0.35$ ) dispersing air in tap water have been determined and empirically correlated using the suggested approach by Michael and Miller (1962). Gas-liquid mass transfer rates have been measured by sparging air, pure  $O_2$ , and an artificial syngas blend in a STR. The dynamic gassing out method for  $O_2$  mass transfer measurements agreed with the results from literature. The myoglobin protein method for measuring dissolved CO mass transfer rates from an artificial syngas mixture was utilized.

Volumetric mass transfer correlations for STRs as a function of specific power density ( $P_g/V$ ) and superficial gas velocity ( $U_g$ ), such as in Eq. (2.6), are restricted to a single vessel diameter and dependent on the gas-liquid hydrodynamics. It is most likely that the experimentally determined exponents used in Eq. (2.6) are functions of geometry and prevailing hydrodynamic conditions as suggested by many researchers.

Proper scale-up of volumetric mass transfer results should be based on three types of similarity: geometric, kinematic, and dynamic. Kinematic and dynamic similarities are combined into hydrodynamic similarity. For successful scale-up, hydrodynamic similarity must be satisfied in addition to geometric similarity. It has been shown that STR scale-up can be accomplished when similar hydrodynamic conditions are observed in vessels of different diameter. Extensive data, available in the literature, covering a wide range of vessel

diameters ( $0.211 \leq T \leq 2.7$  m), have been used to develop a mass transfer correlation appropriate for STR scale-up in the form of Eq. (4.3).

The power density model (Eq. (2.6)) is independent of operating conditions for a single vessel size. When the power density model is applied in a STR scale-up, there are large differences in power densities between bench-top and industrial scale reactors, which perhaps require additional terms to scale-up for the vessel size and for similar hydrodynamics.

The volumetric gas-liquid mass transfer scale-up model (Eq. (4.3)) is dependant on the STR hydrodynamics, which is a necessary condition for scale-up analysis. In the scale-up model, the  $N/N_{CD}$  dispersion parameter does not have large variations compared to power density ( $P_g/V$ ). Its range is approximately the same for different vessel size which implies geometric independence. When hydrodynamic conditions of different vessel sizes are matched,  $k_L a$  values fit the proposed correlation (i.e., Eq. (4.6)). A flow regime map, like the one shown in Fig. 4.7, is useful when completing STR scale-up to ensure that proper hydrodynamic conditions are satisfied.

The scale-up model (Eq. 4.3) is reliable in STR scale-up for other types of gases dispersed in water such as pure  $O_2$ , and CO from artificial syngas. The  $k_L a$  values for pure  $O_2$  are higher than those for air due to difference in the gas-liquid mass transfer driving potential. The  $k_L a$  values for CO from artificial syngas are higher than those from air, since CO is less soluble in water than air.

Gas-liquid mass transfer rates for CO from artificial syngas can be predicted from air measurements (Eq. 4.14), and can be applied over wide range of operating conditions (i.e.,  $T = 0.211$  to  $2.7$  m).

## 5.2 Recommendations

STR scale-up analysis for gas-liquid mass transfer rates presented in this thesis considered physically important parameters such as the dispersion parameter ( $N/N_{CD}$ ), superficial gas velocity ( $U_g$ ), and the tank to impeller diameter ratio ( $T/D$ ). Although the contribution of such parameters are different in the scale-up model (Eq. (4.3)), an overall combination is of great importance in STR scale-up. The assumption made in the scale-up model for any gas type (i.e., pure  $O_2$  or CO from artificial syngas) dispersed in a viscous liquid media is an equal dependence on the  $T/D$  ratio. This assumption seems reasonable, but it should be confirmed by investigating different STRs and impeller sizes applicable in the process industries.

Hydrodynamic flow regime maps were constructed to aid in the scale-up of STRs using Rushton disc impellers (6DT) from available literature data. Different studies in literature have shown that mass transfer rates increase greatly when other types of impellers, and vessel geometries are used, perhaps utilizing lower power consumption. An investigation should be conducted to determine the best combination of geometry and impeller type in the bench-scale STR to maximize gas-liquid mass transfer performance. Upon this completion, the scale-up model and the experimental work of this thesis may be used to aid in the construction of an accurate gas-liquid computerized fluid dynamic model (CFD) in STR scale-up.

A similar scale-up model for ALRs and BCRs is suggested. This model accounts for the hydrodynamic similarity between reactors of different size. In future work, it is recommended to provide experimental evidence for this model by investigating gas-liquid

mass transfer of ALRs and BCRs of different size.

**REFERENCES CITED**

- Aiba, S. (1959). Flow patterns of liquids in agitated vessels. *A.I.Ch.E. Journal*, 4, 485-489.
- Bakker, A., van den Akker, H.E.A., (1994). Gas-liquid contacting with axial flow impellers. *Institution of Chemical Engineers, Part A*, 72, 573-582.
- Bredwell, M.D., Srivastava, P., Worden, R.M., (1999). Reactor design issues for synthesis-gas fermentations. *Biotechnology Progress*, 15, 834-844.
- Bruijn, W., van't Riet, K., Smith, J.M., (1974). Power consumption with aerated Rushton turbines. *Transactions of Institution of Chemical Engineers*, 52, 88-104.
- Bujalski, W., Nienow, A.W., Chatwin, S., Cooke, M. (1987). The dependency on scale of power numbers of Rushton disc turbines. *Chemical Engineering Science*, 42, 317-326.
- Calderbank, P.H. (1958). Physical rate processes in industrial fermentation. Part I: The interfacial area in gas-liquid contacting with mechanical agitation. *Transactions of the Institution of Chemical Engineers*, 36, 443-463.
- Calderbank, P.H. (1959). Physical rate processes in industrial fermentation, Part II. Mass transfer coefficients in gas-liquid contacting with and without mechanical agitation. *Transactions of the Institution of Chemical Engineers*, 37, 173-185.
- Chandrasekharan, K., Calderbank, P.H., (1981). Further observations on the scale-up of aerated mixing vessels. *Chemical Engineering Science*, 36, 819-823.
- Chapman, C.M., Nienow, A.W., Cooke, M., Middleton, J.C., (1983). Particle-gas-liquid mixing in stirred vessels. Part II: Gas-liquid mixing. *Chemical Engineering Design*, 61, 82-95.

- Cowger, J.P., Klasson, K.T., Ackerson, M.D., Clausen, E.C., Gaddy, J.L., (1992). Mass-transfer and kinetic aspects in continuous bioreactors using *Rodospirillum rubrum*. *Applied Biochemistry and Biotechnology*, 34/35, 613-624.
- Dawson, M.K., (1992). The influence of agitator type on fluid dynamics and oxygen mass transfer in a pilot scale mixing vessel. Ph.D. Thesis, School of Chemical Engineering, University of Birmingham, Birmingham, England.
- Figueiredo, M.M., Calderbank, P.H., (1979). The scale-up of aerated mixing vessels for specified oxygen dissolution rates. *Chemical Engineering Science*, 34, 1333-1338.
- Fuchs, R., Ryu, D.D.Y., Humphrey, A.E., (1971). Effect of surface aeration on scale-up procedures for fermentation processes. *Industrial and Engineering Chemistry Process Design and Development*, 10, 190-196.
- Gogate, P.R., Pandit, A.B., (1999). Survey of measurement techniques for gas-liquid mass transfer coefficient in bioreactors. *Biochemical Engineering Journal*, 4, 7-15.
- Greaves, M., Barigou, M., (1988). Estimation of gas holdup and impeller power in a stirred vessel reactor. *Fluid Mixing III*, Institution of Chemical Engineers, 63, 235-255.
- Hickman, A.D. (1988). Gas-liquid oxygen transfer and scale-up. A novel experimental technique with results for mass transfer in aerated agitated vessels. *Proceedings of 6<sup>th</sup> European Conference on Mixing*, Pavia, Italy, 369-374.
- Holland, F.A., Chapman, S.S., (1966). *Liquid mixing and processing in stirred tanks*. Reinhold Publishing Corp., New York, NY.
- Incropera, F.P., DeWitt, D.P., (2002). *Diffusion mass transfer, Fundamentals of Heat and Mass Transfer*, John Wiley & Sons, Inc., New York, NY, 784-823.
- Kaster, J.A., Michelsen, D.L., Velander, W.H., (1990). Increased oxygen transfer in a yeast

fermentation using a microbubble dispersion. *Applied Biochemistry and Biotechnology*, 24/25, 469-484.

Klasson, K.T., Ackerson, M.D., Clausen, E.C., Gaddy, J.L., (1992). Bioconversion of synthesis gas into liquid or gaseous fuels. *Enzyme and Microbial Technology*, 14, 602-608.

Klasson, K.T., Lundback, K.M.O., Clausen, E.C., Gaddy, J.L., (1993a). Kinetics of light limited growth and biological hydrogen production from carbon monoxide and water by *Rhodospirillum rubrum*, *Journal of Biotechnology*, 29, 177-188.

Klasson, K.T., Gupta, A., Clausen, E.C., Gaddy, J.L., (1993b). Evaluation of mass-transfer and kinetic parameters for *Rhodospirillum rubrum* in a continuous stirred tank reactor, *Applied Biochemistry and Biotechnology*, 39/40, 549-557.

Konig, B., Lippert, J., Schugerl, K., (1979). A steady state method for the determination of  $k_{La}$  values in stirred tank reactors. Oxygen transfer rate in model fermentation media with high speed tube stirrer. *German Chemical Engineering*, 2, 371-377.

Linek, V., Banes, P., Sinkule, J., (1990). Dynamic pressure method for  $k_{La}$  measurement in large-scale bioreactors. *Biotechnology and Bioengineering*, 33, 1406-1412.

Linek, V., Banes, P., Sinkule, J., (1990). Critical assessment of the steady-state  $\text{Na}_2\text{SO}_3$  feeding method for  $k_{La}$  measurement in fermentors. *Biotechnology and Bioengineering*, 35, 766-770.

Linek, V., Vacek, V., Banes, P., (1987). A critical review and experimental verification of the correct use of the dynamic method for the determination of oxygen transfer in aerated agitated vessels to water, electrolyte solutions, and viscous liquids. *Chemical Engineering Journal*, 34, 11-34.

- Lines, P.C. (2000). Gas-liquid mass transfer using surface-aeration in stirred vessels with dual impellers. *Institution of Chemical Engineers, Part A*, 78, 342-347.
- Lynd, L. R. (1996). Overview and evaluation of fuel ethanol from cellulosic biomass: Technology, economics, the environment, and policy. *Annual Review of Energy and the Environment*, 21, 403-465.
- Martin, T., McFarlane, C.M., Nienow, A.W., (1994). The influence of liquid properties and impeller type on bubble coalescence behavior and mass transfer in sparged agitated reactors. *Proceedings of 8<sup>th</sup> European Conference on Mixing*, Cambridge, England, 57-64.
- Metzner, A.B., Taylor, J.S., (1960). Flow patterns in agitated vessels. *A.I.Ch.E. Journal*, 6, 109-114.
- Michael, B.J., Miller, S.A., (1962). Power requirements of gas-liquid agitated systems. *A.I.Ch.E. Journal*, 8, 262-266.
- Midoux, N., Charpentier, J.C., (1978). Les reacteurs gaz-liquide a cuve agitee mecaniquement, Partie 1: Hydrodynamique. *Entropie*, 88, 5-38.
- Mississippi State School of Chemical Engineering, Production of ethanol from synthesis gas using fermentation, 2005, School of Chemical Engineering, Accessed 15 March 2005, < [http://www.che.msstate.edu/academics/faculty\\_staff/Zappi/consortium/production\\_of\\_ethanol\\_from\\_synth.htm](http://www.che.msstate.edu/academics/faculty_staff/Zappi/consortium/production_of_ethanol_from_synth.htm) >.
- Nienow, A.W., Miles, D., (1969). A dynamometer for the accurate measurement of mixing torque. *Journal of Scientific Instruments*, 2, 994-995.
- Nienow, A.W., Wisdom, D.J., (1976). Power consumption in aerated turbine-agitated vessels. *Institution of Chemical Engineers 3<sup>rd</sup> Annual Research Meeting*, Salford,

England.

Nienow, A.W., Wisdom, D.J., (1978). The effect on scale on specific absorption rates in aerated vessels with a constant gas residence time. International Symposium on Mixing, London, England, C12, 1-12.

Nienow, A.W., Wisdom, D.J., Middleton, J.C., (1977). The effect of scale and geometry on flooding, recirculation, and power in gassed stirred vessels. Proceedings of 2<sup>nd</sup> European Conference on Mixing, Cambridge, England, F1, 1-16.

Nienow, A.W., Warmoeskerken, M.M.C.G., Smith, J.M., Konno, M., (1985). On the flooding/loading transition and the complete dispersal condition in aerated vessels agitated by a Rushton-turbine. Proceedings of the 5<sup>th</sup> European Conference on Mixing, Wurtsburg, West Germany, 143-154.

Pharamond, J.C., Roustan M., Roques, H., (1975). Determination de la puissance consommee dans une cuve aeree et agitee. Chemical Engineering Science, 30, 907-912.

Pollard, G.J. (1978). Flooding and aeration efficiency in standard stirred vessels. International Symposium on Mixing, Cranfield, Belford, England, C4, 1-16.

Riggs, S.S. (2004). Carbon monoxide and hydrogen mass transfer in a stirred tank reactor. M.S. Thesis, Iowa State University, Ames, IA.

Robinson, C.W., Wilke, C.R., (1973). Oxygen absorption in stirred tanks: A correlation for ionic strength effects. Biotechnology and Bioengineering, 15, 755-782.

Rushton, J.H., Bimbinet, J.J., (1968). Holdup and flooding in air liquid mixing. The Canadian Journal of Chemical Engineering, 46, 16-21.

Rushton, J.H., Oldshue, J.Y. (1953). Mixing: Present theory and practice. Chemical

Engineering Progress, 49, 161-181.

Sebba, F. (1987). Foams and bilyquid foams-aprons. Wiley, New York, NY.

Smith, J.M. (1972). Alternative flow regimes in agitated vessels. Chemical Engineering, 261, 182-185.

Smith, J.M. (1991). Simple performance correlations for agitated vessels. R. King, Ed., Oxford, London, Fluid Mechanics of Mixing, Modeling, Operations and Experimental Techniques, 55-63.

Smith, J.M., van't Riet, K., Middleton, J.C., (1977). Scale-up of agitated gas-liquid reactors for mass transfer. Proceedings of 2<sup>nd</sup> European Conference on Mixing, Cambridge, England, F4, 51-66.

Smith, J.M., Warmoeskerken, M.M.C.G., (1985). The dispersion of gases in liquids with turbines. Proceedings of the 5<sup>th</sup> European Conference on Mixing, Wurtsburg, West Germany, 115-126.

Stenberg, O., Andersson, B., (1988). Gas-liquid mass transfer in agitated vessels: Part II. Modeling of gas-liquid mass transfer. Chemical Engineering Science, 43, 725-730.

United States Department of Energy-Energy Efficiency and Renewable Energy, Oil dependence and energy security, 2005, United States Department of Energy, Accessed 15 March 2005, <<http://www.fueleconomy.gov/feg/oildep.shtml>>.

Valentin, F.H.H., Preen, B.V., (1962). Stoffubertragung Gas/Flussigkeit in einem Ruhrgefass. Einfluss von Ruhrerform, Drehzahl und Gasdurchsatz auf Blasenoberflache und Stoffubergang. Chemie Ingenieur Techink, 34, 194-199.

van de Sande, E. (1974). Air entrainment by plunging water jets. Ph.D. Thesis, Delft University of Technology, The Netherlands.

- van Dierendonck, L.L., Fortuin, J.M.H., Venderbos, D. (1968). The specific contact area in gas-liquid reactors. Proc. 4<sup>th</sup> Eur. Chem. Reaction Symp., Brussels, 205.
- van't Riet, K. (1975). Turbine agitator hydrodynamics and dispersion performance. PhD Thesis, Delft University of Technology, The Netherlands.
- van't Riet, K. (1979). Review of measuring methods and results in nonviscous gas-liquid mass transfer in stirred vessels. Industrial and Engineering Chemistry Process Design and Development, 18, 357-360.
- Vega, J.L., Prieto, B.B., Elmore, E.C., Clausen, E.C., Gaddy, J.L., (1989a). The biological production of ethanol from synthesis gas. Applied Biochemistry and Biotechnology, 20/21, 781-797.
- Vega, J.L., Clausen, E.C., Gaddy, J.L., (1989b). Study of gaseous substrate fermentations: Carbon monoxide conversion to acetate. 1. Batch culture. Biotechnology and Bioengineering, 34, 774-784.
- Westerterp, K., van Dierendonck, L., de Kraa., J. (1963). Interfacial areas in agitated gas-liquid contactors. Chemical Engineering Science, 18, 157-176.
- Warmoeskerken, M.M.C.G., Feijen, J., Smith, J.M., (1981). Hydrodynamics and power consumption in stirred gas-liquid dispersions. Fluid Mixing, Institute of Chemical Engineering Symposium, 64, J1-14.
- Warmoeskerken, M.M.C.G., Smith, J.M., (1982). Description of the power curves of turbine stirred gas-liquid dispersions. Proceedings of the 4<sup>th</sup> European Conference on Mixing, Noordwijkerhout, Netherlands, BHRA Fluid Eng., Cranfield, England, G1, 237.
- Warmoeskerken, M.M.C.G., Speur, J., Smith, J.M., (1984a). Gas-liquid dispersion with pitched blade turbines. Chemical Engineering Communications, 25, 11.

- Warmoeskerken, M.M.C.G., Smith, J.M., (1985). Flooding of disc turbines in gas-liquid dispersions: A new description of the phenomenon. *Chemical Engineering Science*, 40, 2063-2071.
- Warmoeskerken, M.M.C.G., van Houwelingen, M.C., Frijlink, J.J., Smith, J.M., (1984b). Role of cavity formation in stirred gas-liquid-solid reactors. *Chemical Engineering Research and Design*, 62, 197-200.
- Worden, R.M., (1997). *Fuels and chemicals from biomass*, B. Sasha, Ed., New York, ACS Symposium Series.
- Yawalkar, A.A., Heesink, A.B.M., Versteeg, G.F., Prangkar, V.G., (2002b). Gas-liquid mass transfer coefficient in stirred tank reactors. *The Canadian Journal of Chemical Engineering*, 80, 840-848.
- Yawalkar, A.A., Pangarkar, V.G., Beenackers, A.A.C.M., (2002a). Gas hold-up in stirred tank reactors. *The Canadian Journal of Chemical Engineering*, 80, 158-166.
- Zhu, Y., Bandopadhyay, P.C., Wu, J., (2001). Measurement of gas-liquid mass transfer in an agitated vessel. A comparison between different impellers. *Journal of Chemical Engineering of Japan*, 34, 579-584.
- Zlokarnik, M. (1978). Sorption characteristics for gas-liquid contacting in mixing vessels. *Advances in Biochemical Engineering*, 8, 133-151.
- Zlokarnik, M. (2001). Dimensional analysis and scale-up in theory and industrial application. *Journal of Liposome Research*, 11(4), 269-307.